First-principles study of electronic transport in organic molecular junctions

Carlo Motta

A thesis submitted for the degree of *Philosophiae Doctor*

Department of Materials Science

Università degli Studi Milano-Bicocca

December 2012

First-principles study of electronic transport
in organic molecular junctions
Ph.D. Thesis

Carlo Motta
Supervisor: Gian Paolo Brivio

Thesis presented for the degree of Doctor Europaeus and PCAM doctorate

Document typeset in LaTeX

Contents

Chapter 1

Introduction

1.1 Molecular electronics

Physics has been driven very often by the fascinating idea of pushing things to the limit. In some cases the word *limit* is intended in an extensive way. Just think about many fields in physics: astrophysics and cosmology deal with the limit in the large scale, trying to give an answer to questions which regard the whole universe as an "unicuum". On the opposite side, particle physics focuses on the first constituents of matter, looking for an insight into the reality when objects get smaller and smaller. In some cases, the *limit* can assume a more conceptual meaning which does not directly involve the idea of length scales, even if often it implicitly does. For instance, it is enough to mention some recurrent words like "classical limit", "thermodinamical limit", "inelastic limit" and so on. That is, another key issue in physics is to understand what happens when we cross different regimes, or when we stress a property to its limit. In this framework, it is impossible not to mention a word that has recently become of common use, that is *nanotechnology*. The term itself has acquired a broad meaning and encompasses a wide range of fields in many disciplines, but a common denominator of whatever falling within the scope of nanotechnology exists: it concerns the design, characterization and production of structures, devices and systems by controlling their shape and size at lowest possible scale, the nanometer scale. Here, the limit is both conceptual and technical. The idea is to reproduce structures that already exists on the large scale by shrinking their dimensions to the atomic one, that is by using a limited amount of the constituents of matter. This is not straightforward, since at those scales novel phenomena may arise due to the quantum laws that governs matter in this regime so that one has to face very challenging conceptual issues.

Molecular electronics (ME) is a perfect example of the quest to explore a macroscopic phenomenum, the electrical current, into its minimum terms, that is electrons propagating through a small amount of atoms. If we think at the common electronic devices, current flows through metallic stuctures (wires, contacts, etc.) which are made of at least 10^{20} atoms. Pushing the situation to its limit involves the question: how does the electrical current flow

through a single atom or molecule? Can a molecule mimic the behaviour of an ordinary microelectronics component or provide a new functionality? Namely, ME can be defined as the field of science that investigates the electronic and thermal transport properties of circuits in which individual molecules (or an assembly of them) are used as basic building blocks. Of course, being molecular circuits of the order of nanometers, ME is a subfield of nanotechnology. Dealing with systems that are composed by semi-infinite metallic leads, which belong to the realm of the systems investigated by physicists, and molecules, historically the object of study of chemists, ME is a field where different disciplines like physics, chemistry, materials science, biology, electrical engeneering merge down.
It seems unlikely that ME will replace silicon-based electronics, but there are good reasons to believe that it may complement it in terms of novel functionalities emerging at the nanoscale which can integrate the standard ones. It should also be stressed that, from the point of view of fundamental science, molecular junctions are ideal systems to investigate electronic conduction at a scale dominated by quantum effects, and shed new light into the fundamental electron transfer mechanisms that play a key role both in chemistry and biology. The science of molecular electronics has been driven by the need to find ways to exploit the beauty and complexity of the molecular world within solid-state settings. Moreover, one should be forget that the history of science proves that the exploration of new territories and the subsequent discovery of novel phenomena often leads to unexpected technological applications.
All these reasons make ME, which is now a well established discipline, an intriguing and worth-to-explore field of research.

1.2 Fabrication of nanoscale contacts

The experimental realization of metal-molecule-metal junctions has been provided by the development of both adequate chemical methods for preparation of molecule/electrode interfaces appropriate for forming metal-molecule contacts and nanoscale characterization techniques. Vital to experimental studies of metal-molecular junctions is the ability to form atomic-sized metallic contacts. A common way to create such contacts is by means of scanning tunneling microscope (STM) [1]. While in the standard application of an STM a fine metallic tip is held at distance from the counter electrode (in general a metallic surface) by making use of the exponential distance dependence of the tunneling current, the tip can also be indented into the surface and carefully withdrawn until an atomic size contact is formed. Thus, STM molecular contacts (Fig. 1.1) can be achieved in two ways, namely upon withdrawing and approaching the tip from/to the substrate. While in the former case the exact contact configuration is not accessible by experiments, in the latter it can be controlled more precisely. The main advantages of STM are its scanning speed, its versatility, and the possibility to use different metals for the two electrodes. On the other hand, the main drawbacks are its limited stability with respect to the change of external parameters such as the temperature or magnetic fields and the short lifetimes of the contacts in general, due to the sensitivity of

STM to vibrations.

Since the exact arrangement of atoms in the nanocontact cannot be controlled during the

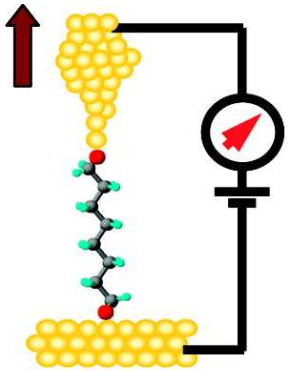

Figure 1.1: Schematic illustration of STM break junction measurement.

formation and breaking of a molecular junction, usually experiments suffer from a lack of reproducibility. Therefore several repetitions of the contact formation/breaking cycle are performed so that the conductance can be averaged over the atomic configurations of the nanocontact. The averaged conductance is more representative of the system under exam, rather than of a particular realization of the nanocontact. An experimental technique which allows for fast formation and breaking of the SMJ is the mechanically controllable break junction (MCBJ) technique [2, 3]. The working mechanism of MCBJ is illustrated in Fig. 1.2: a metallic wire is notched in the middle in order to reduce its cross section in the central region and it is then glued on the substrate. Alternatively, a metallic junction can be patterned over a substrate by means of litography. The bending beam can be curved by pushing upwards the extensible central support, causing an expansion of the upper surface of the beam and a thinning of the contact in proximity of the notch, where the strain is concentrated. After the rupture of the contact, the two cleanly exposed surfaces thus created can be brought together to form a new contact by retracting the extensible support. The two surfaces generated after contact breaking can be quite irregular, therefore the junction formed after coming back to contact is expected to be composed of a single atom.

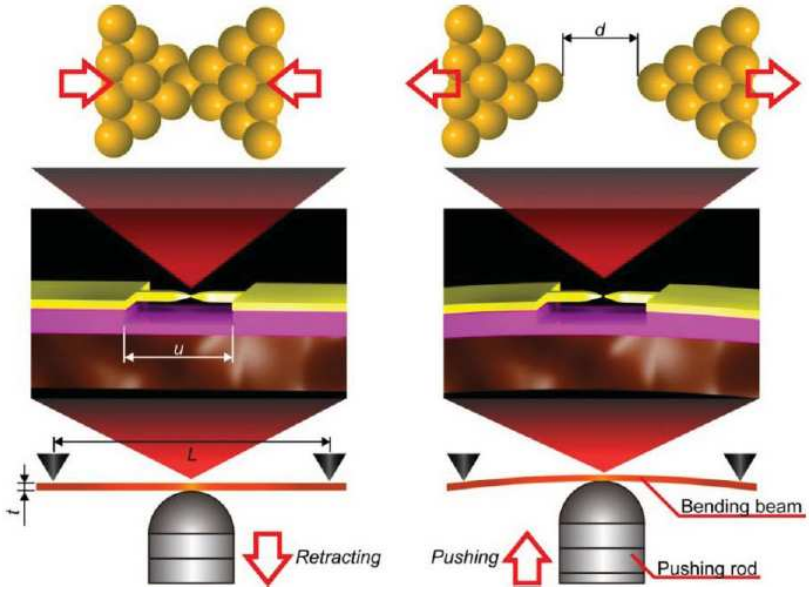

Figure 1.2: Schematic view of the MCBJ operation. The MCBJ set up (bottom) is comprised of a free-standing metal junction formed on bronze substrate by electron beam lithography and metal deposition processes (middle). The narrowest constriction at the center is usually sub-micrometer size. The substrate is deflected by the pushing rod in a three-point bending configuration, which induces the tensile force on the free-standing junction to break it. After breaking, an electrode gap of size d is formed (top). Thereafter, the electrode gap distance can be finely tuned by the vertical displacement of the pushing rod D by $d = rD$, where r is the attenuation factor roughly determined by the device configuration as $r = 3ut/L^2$ [4].

1.3 Metallic point contacts

The STM and MCBJ techniques allow for the rupture of a macroscopic metallic wire with only a few atoms remaining in the smallest cross section before the complete breakage. In this way, one can measure the conductance as the contact between two metals is broken and eventually a single atom (point contact) junction is formed at the last stretching stage. The typical evolution of the conductance during such a controlled elongation is shown in the left panel of Fig. 1.3. These so-called conductance traces present subsequent plateaus, which become pronounced before the contacts completely break. The plateaus are separated by sharp jumps, which have an intensity in the order of the conductance quantum ($2e^2/h$). This step-like structure can be explained by the subsequent rearrangement of the atomic configuration during the elongation. Upon stretching of the contact, the stress accumulates elastic energy in the atomic bonds over the length of a plateau, then at a certain stage the configuration becomes unstable and the contact jumps to an other atomic arrangement, to which correspond a lower number of conduction channel . The direct experimental evidence of this explanation was given by the simultaneous conductance and force measurements of Rubio et al. [6]. In general, the conductance trace changes from realization to realization, as it is

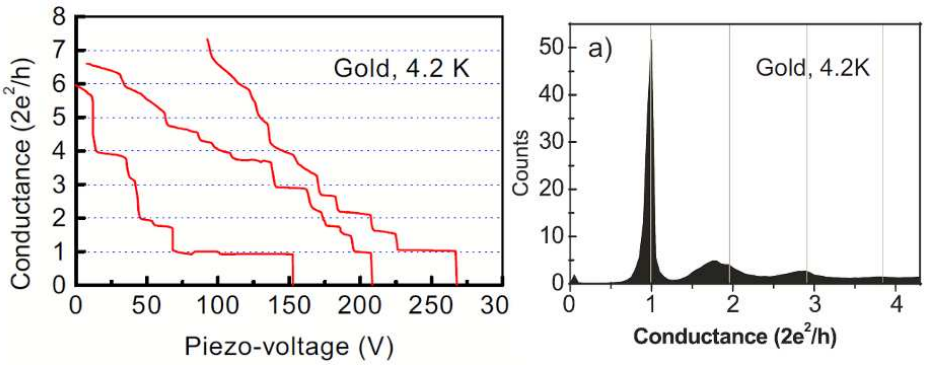

Figure 1.3: Left panel: typical recordings of conductance measured in atomic-size Au contacts, using the MCBJ technique. The conductance is measured as a function of the voltage applied to the piezo elements, which is proportional to the junction elongation. Right panel: typical conductance hystogram. [5]

very sensitive to the experimental procedure. However, certain features are reproducible, like the last plateau in gold contacts which corresponds to atomic-sized contact. These features can be captured by analyzing the statistical conductance histograms. Such conductance histograms are presented in right panel of Fig. 1.3. The peaks in the histogram indicate the conductance values where plateaus are frequently situated during the elongation. For some metals, like the noble ones, several preferred conductance values are found in the histogram but the conductance histogram of each metal shows one common feature: a peak appears right at the edge of the conductance region where the contact is broken and only tunnelling current flows. The position of this peak varies for different metals in the conductance range of $G \sim 0.8 - 3.0 \cdot 2e^2/h$, e.g. for the noble metals it is situated at one quantum unit. This peak is attributed to the conductance of a single metallic atom. During the elongation the last atomic configuration prior to the complete breakage generally contains only a single atom between the electrodes. The conductance is mainly determined by the smallest cross section, and the conductance value of a single atom contact is essentially independent of the atomic arrangement of the electrodes, thus the frequent occurrence of the same conductance value determines a peak in the histogram.
A simple scheme to account for the conductance in atomic-sized contacts is that the number of channels is determined by the number of valence orbitals of the contacting atom. This means in practice that the number of conduction channels for monovalent metals is limited to one, it is four for *sp*-like metals like Al or Pb, and it may be up to 6 for transition metals due to the contribution of the s and d bands.

1.4 Single molecular junctions

In the last decade substantial progress have been done towards the ultimate goal of building single molecular junctions (SMJ) [7, 8, 9, 10, 11]. For a comprehensive discussion on the

experimental aspects of SMJ, see Refs. [4, 12]. The electron transport in molecular junctions is characterized by charge injection barriers at the electrode-molecule interfaces, which is determined by energy alignment between the electrode Fermi level and a single discrete energy level of the molecule; either the highest occupied molecular orbital (HOMO) or the lowest unoccupied molecular orbital (LUMO) levels. Electronic coupling of the junction individual molecules with the macroscopic electrodes via the overlap of the molecular wavefunctions and those of the electrodes also affects the charge transmissivity by broadening the frontier orbital levels. In Fig. 1.4 the two main effects upon allowing the interaction between a molecule and metallic substrates are illustrated. First, the molecular electronic levels renormalize and the HOMO-LUMO gap reduces due to charge rearrangement between the molecule and the leads. Consequently, the electronic levels attain a finite lifetime, thus called molecular resonances. The alignment between the resonances and the Fermi level will determine the conductive properties of the junction.

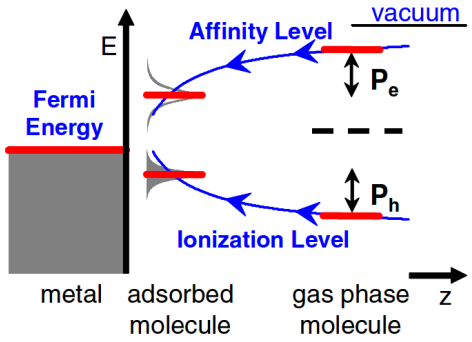

Figure 1.4: Diagram of the energy levels of a single molecule approaching a metallic lead, indicating the polarization shifts of the HOMO and LUMO orbitals [13].

The study of the transport properties of molecular junctions constitues a formidable challenge, both due to the intrinsic limitations of experiments (as seen before) and theory. Since the pioneering experiments of Reed et al. [14] on benzenedithiol, several types of molecules have been investigated with progressive complexity. However, each of the experiments has to face the problem of the reproducibility. The electronic transport depends crucially on the exact coupling between the molecule and the leads, i.e. on the precise atomic arrangement of the contacts. As a result the lead-molecule contact can differ from realization to realization and remarkable variations are observed. As explained before, a statistical analysis is needed to average out the individual experimental realization. Understanding the physics behind such structures is still a major challenge, since the microscopic atomistic details of the junction are inaccessible from the point of view of experiments. Thus theoretical models can give a fundamental support to interpret the electronic and transport properties of these structures, in particular under non-equilibrium conditions imposed by an external voltage.
From the theoretical side, in recent years several methods have been developed to describe the transport properties of materials. Due to the complexity of describing a junction with

semi-infinite leads, earlier approaches rely on phenemenological tight-binding models [15]. A pioneering approach by Lang [16] uses *ab initio* methods to describe the molecular part of the junction and the jellium model for the electrodes. However, the jellium model is known to give a poor description of the electron density on the surface region perturbed by the molecule, and the atomistic details of the molecule-lead contact are not taken into account. Presently, the most advanced method to describe electron transport is the combination of density functional theory (DFT) with the Landauer theory formulated in terms of Green's functions. The latter ones can be derived by the Keldysh non-equilibrium Green's function formalism [17]. This method has many advantages with respect to previous ones: namely, a reliable description of the electronic properties of the atoms in the junction and of those in the leads, the absence of adjustable parameters, and a self-consistent calculation of the charge redistribution due to the application of a bias voltage. Although this method is the most widely used one and it succeeded in many cases to correctly describe transport experiments, it often provides results that are only qualitatively correct. In particular, standard DFT functionals lack of derivative discontinuity and suffer from the self-interaction error, so they are often insufficient to treat molecules weakly coupled to the leads [18]. At present, there is no simple way to predict in which case this approach is reliable and accurate. Some approximations have been developed to overcome its limitations, like many body GW approach or time-dependent DFT [18], but they are only applied to the study of small systems due to their high computational demand.

1.5 Thesis outline

This thesis focuses on the theoretical description of coherent electronic transport in organic molecular junctions.

In **Chap. 2** the complex problem of describing interacting electrons and nuclei is introduced, showing how the Born Oppenheimer approximation provides a useful framework to solve it. The electronic structure problem will be addressed within DFT. So overview of the theory as well as some aspects related to its numerical implementation are given. The theoretical methods used to study ballistic electronic transport are illustrated in detail in **Chap. 3**. The Landauer theory is introduced with a discussion about its assumptions and regime of validity. Then, the formalism of non-equilibrium Green's function, at the basis of transport calculation, is developed. The original contribution of this thesis is developed from **Chap. 4**, which is devoted to an analysis of electronic transport by means of an extremely simplified model for the junction. The chapter starts with a theoretical discussion of the embedding approach, which is a practical method to study the interaction between a finite and an infinite system. Electrons will be considered as moving in a one-dimensional modulated potential introduced to simulate resonant tunneling junctions. Results will be shown by considering both jellium and metallic electrodes. **Chap. 5** shows applications of electronic transport in two dimensional systems. In the first part, we investigate a hybrid graphene

junction, where the linkers between graphene electrodes are graphene nanoribbons. We aim at performing a systematic investigation of how the nanoribbon aspect ratio affects the transport properties of these heterojunctions. Next the conductance properties of photoswitching molecular junctions with graphene electrodes are investigated, calculating the conductance for different diarylethene isomers also in presence of an applied bias. **Chap. 6** is devoted to the investigation of a highly conductive single molecule (pyrazine) junction with Pt leads showing bi-stable states. Our investigation addresses the complex problem of determining which is the physical origin of the different conducting regimes appearing in experiments. We fully characterize pyrazine/Pt junctions presenting a comprehensive study of the structural, conductive and vibrational properties as a function of the electrode stretching. Our findings shed light on the mechanism behind transitions between bi-stable states and contribute to proving the reversibility of the switching process. Apart from the transport properties of nanojunctions, the non-equilibrium Green's function formalism can be also applied to the study of the resonant charge transfer of adsorbates on semi-infinite substrates. In **Chap. 7** we develop a methodology to calculate the resonant lifetimes of the electronic states of molecules adsorbed on metallic or insulating surfaces. After showing how our method works for the test system Cs-p(2x2)-Cu(111), we present our preliminar results for triarylamine molecules on TiO_2 rutile (110), which are relevant for dye sensitized solar cell applications. Our study helps to clarify how the charge transfer is affected by the length of the spacer between the acceptor and donor ends of this class of dyes.

Chapter 2

Electronic Structure Methods

2.1 Born Oppenheimer approximation

The many-body Hamiltonian describing a system of interacting electrons and nuclei is

$$\begin{aligned}\hat{H} =& \hat{T}_e + \hat{T}_n + \hat{V}_{ee} + \hat{V}_{nn} + \hat{V}_{en} = \\ & -\sum_i \frac{\hbar^2}{2m_e}\nabla_i^2 - \sum_I \frac{\hbar^2}{2M_I}\nabla_I^2 \\ & + \frac{1}{2}\sum_{i\neq j}\frac{e^2}{|\mathbf{r}_i - \mathbf{r}_j|} + \frac{1}{2}\sum_{I\neq J}\frac{Z_I Z_J e^2}{|\mathbf{R}_I - \mathbf{R}_J|} - \sum_{i,I}\frac{Z_I e^2}{|\mathbf{r}_i - \mathbf{R}_I|} \quad ,\end{aligned} \tag{2.1}$$

which represents a sum of kinetic energy terms $\hat{T}$ as well as Coulomb interactions between electrons ($\hat{V}_{ee}$), nuclei ($\hat{V}_{nn}$), and electron and nuclei ($\hat{V}_{en}$). In the above expression $\mathbf{r}_i$ represents the coordinates of the ith electron (with mass m_e and charge $-e$), and $\mathbf{R}_I$ are the coordinates of the Ith nucleus (with mass M_I and charge $Z_I e$). The properties of the interacting system may in principle be determined from the time-independent Schrödinger equation

$$\hat{H}\Psi(\mathbf{r},\mathbf{R}) = E\Psi(\mathbf{r},\mathbf{R}) \quad , \tag{2.2}$$

where E is the total energy of the interacting electron-nuclei system described by the eigenfunction Ψ. Here, $\mathbf{r} = \{\mathbf{r}_i\}$ and $\mathbf{R} = \{\mathbf{R}_I\}$ are the full set of nuclear and electronic coordinates. The full time-independent Schrödinger equation is, by pratical means, impossible to solve exactly and approximations are required. One powerful way to solve Eq. (2.2) is to adopt the so-called Born-Oppenheimer approximation. It assumes that the nuclei are infinitely heavy as compared to the electrons so that the ionic and electronic motions can be decoupled from each other. The nuclear coordinates are described as external parameters which vary infinitely slowly. From a mathematical point of view, this consists in writing the full wavefunction in separable form:

$$\Psi(\mathbf{r},\mathbf{R}) = \Phi(\mathbf{R})\psi(\mathbf{r},\mathbf{R}) \quad , \tag{2.3}$$

where the electronic wavefunction $\psi(\mathbf{r},\mathbf{R})$ is a solution $\psi_i(\mathbf{r},\mathbf{R})$ of the following electronic equation:

$$[\hat{T}_e + \hat{V}_{ee} + \hat{V}_{en}]\psi_i(\mathbf{r},\mathbf{R}) = \varepsilon_i\psi_i(\mathbf{r},\mathbf{R}) \quad . \tag{2.4}$$

In the latter expression i represents the set of quantum numbers characterizing a given N-electrons eigenstate with energy ε_i. The electronic wavefunction $\psi_i(\mathbf{r},\mathbf{R})$ describes an electronic eigenstate corresponding to a given geometrical configuration $\mathbf{R}$ of the nuclei, and its $\mathbf{R}$-dependence is purely parametric (i.e. there is no $\nabla_{\mathbf{R}}$ operator in (2.4)). The assumption behind the factorization defined by Eqs. (2.3), (2.4), known as the adiabatic or Born-Oppenheimer scheme, is that, once an initial electronic state has been selected, the nuclei move slowly enough not to induce transitions to different electronic states. The Eq. (2.4) can be derived by substituting the wavefunction expression (2.3) in (2.1). First, one should consider that $\hat{T}_e$ (which contains the operator ∇_r^2) does not act on the $\mathbf{R}$ coordinates. Then, the non-adiabatic terms should be neglected, that is those terms which involves derivatives $\nabla_{\mathbf{R}}$ of the electronic wavefunction $\psi_i(\mathbf{r},\mathbf{R})$ [a]. The details of the formal derivation are described in Refs. [19, 20]. Once the electronic problem is solved, the adiabatic motion of the nuclei is governed by the following equation:

$$[\hat{T}_n + \hat{V}_{nn} + \varepsilon_i(\mathbf{R})]\Phi(\mathbf{R}) = E_i(\mathbf{R})\Phi(\mathbf{R}) \quad . \tag{2.5}$$

Note that $(\hat{V}_{nn} + \varepsilon_i)$ plays the role of the potential acting on the nuclear wavefunction, and that for each energy $\varepsilon_i(\mathbf{R})$ there is a full orthonormal basis set $\{\Phi_{i,\alpha}(\mathbf{R})\}$ of nuclear wavefunctions. To study the electronic properties of a system we solve (2.4) by introducing various methods: for the ground state, the Hartree-Fock approach or the Density Functional Theory (DFT), if we work within an *ab initio* method. In the next Section we shall outline the main properties of DFT, which is nowadays the most used first principles approach.

2.2 Density Functional Theory

Density Functional Theory (DFT) is a method which determines the ground state of a system of N electrons. In DFT the system charge density is the relevant physical quantity. DFT has proved to be succesful in accounting for structural and electronic properties of a vast class of materials, ranging from atoms and molecules to crystals and other complex extended systems.

In this Section we introduce the two basic theorems of DFT, the Kohn Sham equations, the Local Density Approximation and Gradient Corrected Approximation. Also, we mention how DFT is implemented by using a localized basis set.

2.2.1 The Hohenberg-Kohn Theorem

Let us consider a system of N interacting electrons in an external potential $V_{ext}(\mathbf{r})$. If the system has a nondegenerate ground state, it is obvious that there is only one ground-state

[a] The adiabatic approximation consists precisely in neglecting these terms.

charge density $n(\mathbf{r})$ that corresponds to a given $V_{ext}(\mathbf{r})$. In 1964, Hohenberg and Kohn (HK) [21] demonstrated the inverse, far less obvious result: there is only one external potential $V(\mathbf{r})$ that yields a given ground-state charge density $n(\mathbf{r})$. The demonstration is very simple and uses a reductio ad absurdum argument.

First HK theorem. Given the external potential $V_{ext}(\mathbf{r})$, the total energy of a N-electron system is a unique functional[b] of the ground state (GS) electron density $\rho(\mathbf{r})$.

The total energy can be written as:

$$E[\rho(\mathbf{r})] = V_{ext}[\rho(\mathbf{r})] + T[\rho(\mathbf{r})] + U_{ee}[\rho(\mathbf{r})] := \int \rho(\mathbf{r}) V_{ext}(\mathbf{r}) dr + F_{\mathrm{HK}}[\rho(\mathbf{r})]. \tag{2.9}$$

The term $F_{\mathrm{HK}}[\rho]$ is the so called Hohenberg-Kohn functional, which depends only on the density and whose form is universal. The second Hohenberg and Kohn theorem provides the variational principle to determine the energy of the system:

Second HK theorem. The GS energy can be obtained variationally: the density that minimizes the total energy is the exact GS density.

That is, given a trial density $\rho'(r)$ so that $\rho'(r) \geq 0$ and $\int \rho'(r) dr = N$, it follows that $E_{\mathrm{GS}}[\rho_0] \leq E[\rho']$. The GS energy is given by the functional of the exact GS charge density ρ_0. In this way, DFT exactly reduces the N-body problem to the determination of a 3 - dimensional function $\rho(\mathbf{r})$ which minimizes the functional $E[\rho(\mathbf{r})]$ in (2.9). Unfortunately this functional is unknown, since we do not know the exact form of $F_{\mathrm{HK}}[\rho]$.

2.2.2 The non-interacting system

One year later, Kohn and Sham (KS) reformulated the problem and opened the way to practical applications of DFT [22]. They proved that *the system of interacting electrons can be mapped on to an auxiliary system of non-interacting electrons having the same ground*

[b] A functional is the generalization of the concept of a function: a function associates a value with another value, while a functional associates a value with a given function. The functional dependence is indicated by square brackets so, if $f(r)$ is a simple function, it can be written in a generical way like this:

$$F[f] = \int g\left(f(r)\right) dr \tag{2.6}$$

The differential of a functional is the term coming from $F[f + df] - F[f]$ which depends linearly by df:

$$\delta F = \int \frac{\delta F[f]}{\delta f(x)} \delta f(x) dx \quad , \tag{2.7}$$

where the quantity $\frac{\delta F[f]}{\delta f(x)}$ is the functional derivative of F with respect to f at the point x. Functional derivatives obeys some simple rules similar to those of normal derivatives: the chain rule and the rule for the derivations of a product still hold when dealing with functionals. Here we only recall that, if $f(x)$ is a function,

$$\frac{\delta f(x)}{\delta f(y)} = \delta(x - y) \quad . \tag{2.8}$$

state charge density $\rho(\mathbf{r})$. This can be done thanks to the first HK Theorem: we consider a system whose density is the same of the interacting system, but without interaction between particles. In this way we can compute exactly the kinetic energy functional. For a system of non-interacting electrons the ground-state charge density can be represented as a sum over one-electron orbitals (the KS *orbitals*) $\psi_i(\mathbf{r})$

$$\rho(\mathbf{r}) = \sum_{j}^{occ.} |\psi_j(\mathbf{r})|^2 \quad . \tag{2.10}$$

In general j runs fron 1 to $N/2$ if we assume double occupancy of all states, and the KS orbitals are the solution of the Schrödinger-like equation

$$\left(-\frac{\hbar^2}{2m}\nabla^2 + V_{\mathrm{KS}}(\mathbf{r})\right)\psi_j(\mathbf{r}) = \epsilon_j\psi_j(\mathbf{r}) \tag{2.11}$$

with the orthonormality constraint:

$$\int \psi_i^*(\mathbf{r})\psi_j(\mathbf{r})d\mathbf{r} = \delta_{ij} \quad . \tag{2.12}$$

2.2.3 The Kohn-Sham equations

The problem is now to determine $V_{\mathrm{KS}}(\mathbf{r})$ for a given $\rho(\mathbf{r})$. The problem is solved by considering the variational property of the energy, as specified in the second HK theorem. The condition to be verified is that the functional derivative with respect to the ψ_i of the constrained functional

$$E' = E - \sum_{ij}\lambda_{ij}\left(\int \psi_i^*(\mathbf{r})\psi_j(\mathbf{r})d\mathbf{r} - \delta_{ij}\right) \tag{2.13}$$

where λ_{ij} are Lagrange multipliers, must vanish:

$$\frac{\delta E'}{\delta\psi_j^*(\mathbf{r})} = \frac{\delta E'}{\delta\psi_j(\mathbf{r})} = 0 \tag{2.14}$$

The energy functional can be written as follows:

$$E = T_s[\rho(\mathbf{r})] + E_{\mathrm{H}}[\rho(\mathbf{r})] + E_{xc}[\rho(\mathbf{r})] + \int \rho(\mathbf{r})V_{ext}(\mathbf{r})d\mathbf{r} \tag{2.15}$$

The first term is the kinetic energy of *non-interacting* electrons:

$$T_s[\rho(\mathbf{r})] = -\frac{\hbar^2}{2m}2\sum_j \int \psi_j^*(\mathbf{r})\nabla^2\psi_j(\mathbf{r})d\mathbf{r} \quad . \tag{2.16}$$

The second term (called the Hartree energy) contains the electrostatic interactions between clouds of charge:

$$E_{\mathrm{H}}[\rho(\mathbf{r})] = \frac{e^2}{2}\int \frac{\rho(\mathbf{r})\rho(\mathbf{r}')}{|\mathbf{r}-\mathbf{r}'|}d\mathbf{r}d\mathbf{r}' \quad . \tag{2.17}$$

The third term, called the exchange-correlation energy, contains all the remaining terms, and its exact form is unknown[c]. It is defined as:

$$E_{xc}[\rho] = T[\rho] - T_s[\rho] + U_{ee}[\rho] - E_{\mathrm{H}}[\rho] \tag{2.18}$$

Taking into account that

$$\frac{\delta\rho(\mathbf{r})}{\delta\psi_i^*(\mathbf{r}')} = \psi_i(\mathbf{r})\delta(\mathbf{r}-\mathbf{r}') \tag{2.19}$$

one can easily compute the functional derivatives of each term appearing in the energy functional and solve out explicitly the equation (2.14) [22]. In this way, one then finds:

$$\hat{H}_{\mathrm{KS}}\psi_i = \sum_j \lambda_{ij}\psi_j \tag{2.20}$$

where the operator $\hat{H}_{\mathrm{KS}}$, called KS Hamiltonian, is defined as

$$\hat{H}_{\mathrm{KS}} = -\frac{\hbar^2}{2m}\nabla^2 + V_{\mathrm{H}}(\mathbf{r}) + V_{xc}(\mathbf{r}) + V_{ext}(\mathbf{r}) = -\frac{\hbar^2}{2m}\nabla^2 + V_{\mathrm{KS}}(\mathbf{r}) \quad . \tag{2.21}$$

Here we have introduced the Hartree potential

$$V_{\mathrm{H}}(\mathbf{r}) = e^2 \int \frac{\rho(\mathbf{r}')}{|\mathbf{r}-\mathbf{r}'|} d\mathbf{r}' \tag{2.22}$$

and an exchange-correlation potential

$$V_{xc}(\rho(\mathbf{r})) = \frac{\delta E_{xc}}{\delta\rho(\mathbf{r})} \quad . \tag{2.23}$$

The Lagrange multipliers λ_{ij} are obtained by multiplying both sides of (2.20) by $\psi_k^*(\mathbf{r})$ and integrating:

$$\lambda_{ik} = \int \psi_k^*(\mathbf{r}) \left(-\frac{\hbar^2}{2m}\nabla^2 + V_{\mathrm{H}}(\mathbf{r}) + V_{xc}(\mathbf{r}) + V_{ext}(\mathbf{r}) \right) \psi_k(\mathbf{r}) d\mathbf{r} \tag{2.24}$$

By doing a subspace rotation in the $\{\psi\}$ space leaving the charge density invariant, one obtains the so-called Kohn-Sham equations:

$$\left(H_{\mathrm{KS}} - \epsilon_i\right)\psi_i(\mathbf{r}) = 0 \quad , \tag{2.25}$$

where $\lambda_{ij} = \delta_{ij}\epsilon_j$.

2.2.4 Approximation functionals for the exchange-correlation energy

The KS equations are similar to the Hartree-Fock (HF) equations. Both are derived from a variational principle and have to be solved out self consistently, which correspond to minimize the energy functional (KS) of the energy for a single Slater determinant (HF). It is important

[c]The logic behind such procedure is to subtract out easily computable terms which account for a large fraction of the total energy.

to point out that, while the HF equations are derived starting from an approximation, that is taking the GS total electron wavefunction as a Slater determinant, while the derivation of KS equations is exact. In the HF equations the non-local exchange term appears in the place of the local exchange-correlation potential of the KS equations:

$$\left(-\frac{\hbar^2}{2m}\nabla^2 + V_{\rm H}(\mathbf{r}) + V_{ext}(\mathbf{r})\right)\psi_j(\mathbf{r}) + e^2\sum_{j,||}\int \frac{\psi_j^*(\mathbf{r}')\psi_j(\mathbf{r})}{|\mathbf{r}-\mathbf{r}'|}\psi_i(\mathbf{r}')d\mathbf{r}' = \epsilon_j\psi_j(\mathbf{r}) \quad , \tag{2.26}$$

where the sum over j extends only to states with parallel spins. The exchange-correlation energy contains three contributions: the exchange energy (that is present also in HF), the correlation energy, and a contribution coming from the difference between the true many-body kinetic energy $\langle\Psi|T|\Psi\rangle$ and the kinetic energy $T_s[\rho]$ of the non-interacting electrons. The exchange term in the HF equations is a nonlocal operator, acting on a function ψ as $(V_x\psi)(\mathbf{r}) = \int V_x(\mathbf{r},\mathbf{r}')\psi(\mathbf{r}')d\mathbf{r}'$. In earlier calculations, an approximated form was often used. In the homogeneous electron gas, the exchange energy ϵ_x and exchange potential v_x for an electron are

$$\langle\epsilon_x\rangle = -\frac{3}{4}\frac{e^2k_{\rm F}}{\pi} \tag{2.27}$$

$$\langle v_x\rangle = -\frac{3}{2}\frac{e^2k_{\rm F}}{\pi} \tag{2.28}$$

where $k_{\rm F}$ is the Fermi wavevector: $k_{\rm F} = (3\pi^2\rho)^{1/3}$. In 1951 Slater proposed to replace the nonlocal exchange potential with the above form valid for the homogeneous electron gas, but with $k_{\rm F}$ evaluated at the local density $\rho(\mathbf{r})$. This procedure yields a *local* (multiplicative) exchange potential

$$V_x(\mathbf{r}) = -\frac{3}{2}\frac{e^2}{\pi}\left[3\pi^2\rho(\mathbf{r})\right]^{1/3} \quad . \tag{2.29}$$

Eq. (2.29) was the first attempt to find an explicit (approximated) form for the exchange potential V_x.

Local density approximation

On the basis of this idea, one of the most used approximations for the exchange-correlation potential has been introduced by Kohn and Sham in 1965, the so called Local Density Approximation (LDA). They approximated the exchange-correlation energyfunctional $E_{xc}[\rho(\mathbf{r})]$ introducing the exchange-correlation energy of the homogeneous electron gas locally depending on $\rho(\mathbf{r})$:

$$E_{xc}[\rho(\mathbf{r})] = \int \epsilon_{xc}(\rho(\mathbf{r}))\rho(\mathbf{r})d\mathbf{r} \quad , \tag{2.30}$$

with

$$\frac{\delta E_{xc}}{\delta\rho(\mathbf{r})} = \mu_{xc}(\rho(\mathbf{r})) = \left(\epsilon_{xc}(\rho) + \frac{d\epsilon_{xc}}{d\rho}\right)_{\rho=\rho(\mathbf{r})} \quad . \tag{2.31}$$

In the LDA approximation the exchange potential (appearing in the KS equations) is equal to

$$V_x^{KS}(\mathbf{r}) = -\frac{e^2}{\pi}\left[3\pi^2\rho(\mathbf{r})\right]^{1/3} \quad , \tag{2.32}$$

that is exactly 2/3 of the Slater local exchange, Eq. (2.29) [23].

Local Spin Density Approximation

So far the KS equations have been considered independent of spin. DFT can be also extended to calculate ground-state properties of spin-polarized systems; in this case the electronic density is split into two parts polarized in opposite way, $\rho = \rho_\uparrow + \rho_\downarrow$, and the energy is a functional of both these components, $E = E[\rho_\uparrow, \rho_\downarrow]$. In fact, we limit ourselves to study collinear systems and perturbations with magnetic fields only oriented along the z-axis, we can consider only the diagonal terms of the spin-density matrix $\rho_{\alpha,\beta}$. So in the Local Spin Density Approximation (LSDA)the exchange and correlation potential can be written as

$$V_{xc}^{LSD} = \int \rho(\mathbf{r}) \epsilon_{xc} \left(\rho_\uparrow(\mathbf{r}), \rho_\downarrow(\mathbf{r})\right) d\mathbf{r} \quad , \tag{2.33}$$

where ϵ_{xc} is the exchange and correlation energy per particle of the homogeneus electron gas at densities $(\rho_\uparrow, \rho_\downarrow)$. An important quantity is the relative polarization

$$\varsigma = \frac{\rho_\uparrow - \rho_\downarrow}{\rho} \quad .$$

If it is equal to one, all the spins are oriented along the same direction or, equivalently, the system is completely polarized. The LSDA is constructed using the following parametrization for the exchange and correlation energy:

$$\epsilon_{xc}(\rho, \varsigma) = \epsilon_{xc}(\rho, \varsigma = 0) + \left[\epsilon_{xc}(\rho, \varsigma = 1) - \epsilon_{xc}(\rho, \varsigma = 0)\right] g(\varsigma) \quad , \tag{2.34}$$

whre $g(\varsigma)$ is an interpolation function [24]:

$$g(\varsigma) = \frac{(1+\varsigma)^{4/3} + (1-\varsigma)^{4/3} - 2}{2(2^{1/3} - 1)} \quad . \tag{2.35}$$

Generalized Gradient Approximation

In order to improve the LDA, the so-called Generalized Gradient Approximation (GGA), where the gradient of the density is also considered, has been introduced [25]. In comparison with LDA, GGA tends to improve total energies, atomization energies, energy barriers and structural energy differences [26]. In GGA, the exchange-correlation energy depends both on the homogeneous electron gas density and on its gradient:

$$E_{xc}^{GGA}[\rho(\mathbf{r})] = \int f(\rho(\mathbf{r}), \nabla\rho(\mathbf{r})) d\mathbf{r} \quad , \tag{2.36}$$

where f is a parametrized analytic function. To obtain reasonable results the function f must be chosen with care, because the expression (2.36) does not derive from a physical system. The xc-functional used for most of the calculations presented in this thesis is the Perdew-Burke-Ernzerhof (PBE) functional [26]. The PBE functional is based on earlier PW91, but avoiding cumbersome features. It contains a unified real space cutoff for exchange and correlation

holes [27] to avoid spurious long range parts in the second order gradient expansion of density. PBE does not have any fitting parameters, retains correct features of LSDA, combines them with the most energetically important features of gradient-corrected nonlocality.

2.3 SIESTA method

In order to use DFT for numerical calculations one needs to consider many technical details and further approximations related to the implementation. Besides the inevitable approximation for the *xc*-functional discussed above, some of the main aspects in the SIESTA (Spanish Initiative for Electronic Simulations with Thousands of Atoms) code, used in this work, are briefly described below. For a complete description the reader is referred to Refs. [28, 29, 30]. In order to solve differential equations such as the Kohn-Sham equations one needs to specify appropriate boundary conditions (BCs). In SIESTA, as in many other DFT codes, one uses periodic BCs corresponding to a supercell with periodicity in all three dimensions. This is convenient for treating infinite systems such as crystals, but can also handle finite systems by making the supercell sufficiently large separating the objects. The framework in the supercell approach is Bloch's theorem, which states that for a periodic system the electronic wavefunction can be written as a product of a wavelike part and a cell-periodic part, i.e.,

$$\psi_{j,\mathbf{k}}(\mathbf{r}) = e^{i\mathbf{k}\mathbf{r}} u_{j,\mathbf{k}(\mathbf{r})} \tag{2.37}$$

where j is a discrete band index and $\mathbf{k}$ a reciprocal lattice vector belonging to the first Brillouin zone (BZ) corresponding to the supercell. The theorem allows for mapping the KS eigenvalue problem into the reciprocal space, where one can separately obtain for each k-point a discrete set of eigenstates of the Hamiltonian. The expectation value of some one-body operator $\hat{O}$ is then calculated as

$$\langle \hat{O} \rangle = \frac{1}{\Omega_{BZ}} \int_{BZ} d\mathbf{k} O(\mathbf{k}) \approx \sum_{\mathbf{k} \in BZ} w_{\mathbf{k}} O(\mathbf{k}) \tag{2.38}$$

where the integral over the first Brillouin zone (BZ), with volume Ω_{BZ}, for practical purposes is approximated by a sum over $\mathbf{k}$-points with weight factors $w_{\mathbf{k}}$ (adding up to one). In SIESTA this discrete BZ sampling is based on the so-called Monkhorst-Pack [31]. Note at this point that the larger the supercell the smaller the corresponding BZ. For sufficiently large supercells this BZ sampling becomes less critical and using only the Γ-point might be a reasonable approximation. In most DFT implementations one uses pseudopotentials to get rid of the core electrons. The idea is to replace the true atomic potential and the chemically inert core electrons with an effective potential (the pseudopotential) that provides the same description for the valence electrons. As a result the computations simplify since one just has to solve for the valence electronic structure. In SIESTA one generally uses norm-conserving pseudopotentials according to the Troullier-Martins parameterization [32]. For a numerical solution of the Kohn-Sham equations one typically chooses a finite basis by which to represent the wave functions. In SIESTA one uses atomic-like localized orbitals that guarantee the

Hamiltonian and overlap matrix to be sparse. For each atom I positioned at $\mathbf{R}_I$ one defines a set of atom-centered orbitals

$$\phi_{I,lmn}(\mathbf{r}) = \phi_{I,ln}(r_I) Y_{lmn}(\hat{\mathbf{r}}_I) \tag{2.39}$$

where $\phi_{I,ln}(r_I)$ and $Y_{lmn}(\mathbf{r}_I)$ are radial and angular components, respectively. Distances are conveniently written in terms of $\mathbf{r}_I = \mathbf{r} - \mathbf{R}_I$ and the angular momentum is labeled by l, m. With a multiple-ζ basis there will be several orbitals (labeled n) corresponding to the same angular momentum but with different radial dependence. The basis orbitals are strictly confined in the sense that they are zero beyond a certain radius (which may be different for each of the radial functions). This cutoff radius is usually specified indirectly in terms of a confinement energy. The SIESTA basis implies that the calculation of the overlap matrix and most matrix elements of the Hamiltonian are two-center integrals, which are effectively calculated within Fourier space where the convolution becomes a simple product. However, the density and some Hamiltonian matrix elements are calculated on a real-space grid. The fineness of this grid is conveniently described by an energy "grid cutoff"[d].

[d]The grid cutoff to represent the density is not directly comparable to the energy cutoff in the context of plane-wave codes, which usually refers to the wavefunctions.

Chapter 3

Electronic Transport

3.1 Transport regimes

The electrical conduction in macroscopic metallic wires is described by Ohm's law $i = GV$, which establishes that the current is proportional to the applied voltage. The constant of proportionality is the conductance, G, which for a sample with cross-section S and length L reads $G = \sigma S/L$, where σ is the conductivity of the material. However, concepts like Ohm's law are not applicable at the atomic scale. Atomic-size conductors are a limiting case of systems in which quantum coherence plays a central role in the transport properties.

We can define different transport regimes according to the relative size of the various length scales [5]. A fundamental length scale is the phase coherence length, L_ϕ, which measures the distance over which the phase of the electron wave function is preserved. Phase coherence can be destroyed by inelastic scattering mechanisms like electron-electron or electron-phonon interactions. A typical value of L_ϕ for Au at T =1K is around 1μm, while at room temperature it lowers to few tens of nm. The *mesoscopic* regime is determined by the condition $L < L_\phi$, where L is the sample length.

Another important length scale is the elastic mean free path L_m which measures the distance between static collision with static scatterers. This quantity can be also referred to as the momentum relaxation length. The regime $L_m \ll L$ is called *diffusive*. In a semiclassical picture the electron motion in this regime is a random walk of steps L_m among the impurities. On the other hand, when $L_m \gg L$ we reach the *ballistic* regime in which the electron momentum can be assumed to be constant and only limited by the scattering with the geometric boundaries of the sample. The two regimes are schematically illustrated in Fig. 3.1.

So far, we have assumed that the typical dimensions of the sample are larger than the electron Fermi wavelength λ_F. However, in the case of atomic-scale junctions we have that the cross section W of the junction is so small that $\lambda_F \sim W$. We thus enter the full quantum limit, where semiclassical arguments fail, and we need a full quantum picture of transport at those scales.

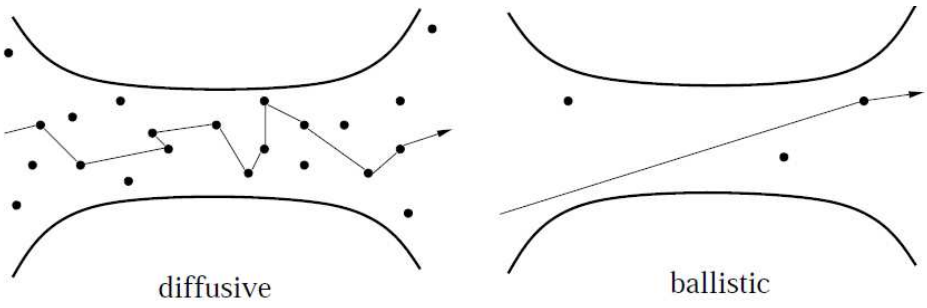

Figure 3.1: Schematic illustration of a diffusive (left) and ballistic (right) conductor [3].

3.2 Assumptions

Calculating the electronic current flowing in a system due to the application of a bias voltage is one of the most challenging problems in solid state physics. Actually, electrical transport is a non-equilibrium statistical problem. We are interested in systems whose dimensions are in the range of the *nanoscale*, for example nanotubes, atomic wires, small molecules sandwiched between metal electrodes. On the macroscopic scale one can define different quantities describing the system like current and charge density or the applied electric field. However, it is very difficult to trace these quantities down to the microscopic scale due to the complicated thermodynamical averaging taking place. On the other hand, even the very microscopic view of transport contains many important physical processes which are hard to describe. A very simple system to generate a current is the discharge of a capacitor. In this case, if we wait enough no current (in a time-averaged sense) will flow in the system, which will reach an equilibrium state. However, we can make the decay time longer by increasing the capacitance of the system (for example by increasing the size of the electrodes), while keeping the resistance fixed. If we extend this idea to the limit, we reach the concept of *reservoir*: a reservoir is an ideal systems that can supply and receive an arbitraty amount of carriers and energy without changing its internal state[a].
We will describe a very powerful method to calculate the conductance of small systems, the so-called *Landauer approach*. This approach rests on specific physical assumptions that may or not may satisfied in experimental realizations of transport in nanoscale systems.

1. *Open quantum system.* The main principle of this approach is the assumption that the system under study is coupled to large reservoirs where all inelastic processes take place. Since the reservoirs may represent a battery, the energy required to extract an electron from one reservoir and bring it into the system can be different from the energy required to bring it into the second reservoir. We thus assume that the electrochemical potentials associated to the two reservoirs differ by the bias:

$$V = \frac{\mu_L - \mu_R}{e} \quad . \tag{3.1}$$

[a]If the external system exchanges only energy and not particles, it is called a "bath"

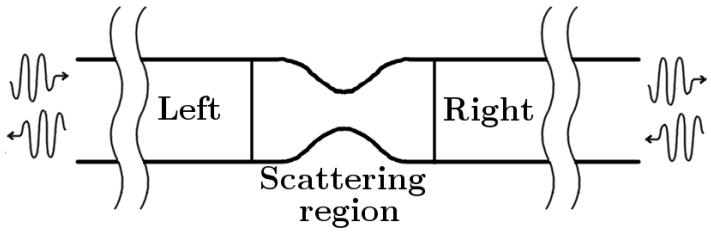

Figure 3.2: Scattering setup: we work with a close but infinite quantum system composed of the device region sandwiched between two leads.

As a consequence, the transport through the systems can be formulated as a quantum mechanical scattering problem. Hence one can reduce the non-equilibrium transport problem to a quantum mechanical one.

2. *Ideal steady state.* It is possible to wait long enough so that the system reach a steady state, that is its density operator does not depend on time.

3. *Openess vs. boundary conditions.* Since we are in a steady state, the role of the reservoirs is just to continuously supply electrons to be injected into the junction. Thus the open system can be mapped to a finite one with suitable boundary conditions. Electrons are prepared in the distant past and far away from the junction into wave-packets. These wave-packets move towards the junction from the leads, scatter on the junction potential, and move away propagating in the opposite lead.

4. *Mean-field approximation.* Let us assume that the Hamiltonian of the scattering region $\hat{H}_S$ can be separed into at least two components:

$$\hat{H}_S = \hat{H}^{mf} + \hat{V} \quad ,$$

where $\hat{H}^{mf}$ is the Hamiltonian describing independent electrons in the presence of the ions that do not belong to the junction, and $\hat{V}$ is the interaction energy between electrons -beyond mean field- in the nanojunction, and the interaction energy of these electrons with the ions of the junction. To practical purpose, we adopt mean-field approximation and we will consider DFT Hamiltonian $\hat{H}_S$ as in Eq. (2.21) to describe the full lead-nanojunction-lead system.

5. *Independent channels.* After the previous assumptions, we are left with a static and deterministic single-particle problem, that is easier to solve than the true non-equilibrium statistical one. We assume that the initial electronic state can be expanded into different channels, that are a set of quantum numbers that describes a scattering solution. The initial state reads:

$$|\Psi(t)\rangle = \sum_{E_i,\alpha} c_{E_i,\alpha} |\Psi_{E_i,\alpha}\rangle e^{-\frac{i}{\hbar}E_i t} \quad , \tag{3.2}$$

where $\hat{H}_S|\Psi_{E_i,\alpha}\rangle = E_i|\Psi_{E_i,\alpha}\rangle$ and α is any set of quantum nunbers necessary to describe the system. We will also assume that electrons are injected from the left (right) reservoir (right (left) moving electrons) with a local distribution function appropriate to the corresponding chemical potential:

$$f_{L(R)}(E) = \frac{1}{e^{(E-\mu_{L(R)})/k_B\Theta} + 1} \quad , \tag{3.3}$$

where Θ is the temperature. With these hypoteses, the basic idea of the scattering approach is to relate the transport properties (conductances) with the transmission and reflection probabilities for carriers incident on the sample. In this one-electron approach phase-coherence is assumed to be preserved on the entire sample and inelastic scattering is restricted to the electron reservoirs only. Instead of dealing with complex processes taking place inside the reservoirs they enter into the description as a set of boundary conditions. Why is the Landauer approach different from other ones like the Drude Model, the Kubo formalism, and the Maxwell equations [17]? The conceptual difference is the following: even if we have a bias represented by the chemical potential difference, we do not use that bias as a perturbation to some Hamiltonian. Instead, the bias here is a boundary condition on the system, where wave-packets with given momenta carry the current across the nanojunction. Due to the scattering of those wavepackets with the potential $\hat{V}$ of the junction, each electron has a finite probability to be transmitted in any given direction, and consequently a probability to be reflected.

3.3 Landauer Theory

Here we illustrate the Landauer theory, which will be derived more rigorously in the next Section. We outline the derivation proposed in Ref. [17]. To simplify, we will consider two identical left and right leads to define the scattering states and the subsequent definition of channels. We suppose that the system is subject to a given confinement potential along the $(x, y = \mathbf{r}_\perp)$ plane and the transport occurs along the z direction. The eigenstates of the L,R asymptotic Hamiltonians can be easily found:

$$H_{L,R}\psi_{\alpha,k}(\mathbf{r}) \equiv \left[\frac{-\hbar^2}{2m}\nabla^2 + V_{L,R}(\mathbf{r}_\perp)\right]\psi_{\alpha,k}(\mathbf{r}) = E_\alpha(k)\psi_{\alpha,k}(\mathbf{r}) \quad , \tag{3.4}$$

which can be separated into longitudinal and transverse equations giving solutions like

$$\psi_{\alpha,k}(\mathbf{r}) \sim u_\alpha(\mathbf{r}_\perp)e^{ikz} \tag{3.5}$$

with energies (subbands)

$$E_\alpha(k) = \epsilon_\alpha + \frac{\hbar^2 k^2}{2m} \tag{3.6}$$

Given an energy E, the number of channels (transverse modes) at that energy is $N_c(E) = \sum_\alpha \Theta(E - E_\alpha)$. We have determined the solutions at the boundaries. We now need to determine the general solution for $\hat{H}_S$, which corresponds to the full lead-nanojunction system.

That is, we need a solution of

$$\hat{H}_S\Psi_{\alpha,k}(\mathbf{r}) \equiv \left[\frac{-\hbar^2}{2m}\nabla^2 + V(\mathbf{r})\right]\Psi_{\alpha,k}(\mathbf{r}) = E\Psi_{\alpha,k}(\mathbf{r}) \quad . \tag{3.7}$$

The solutions $\Psi_{\alpha,k}(\mathbf{r})$ have to asymptotically merge with the eigenstates of H_L and H_R. Consider an electron with energy E_i that for $z \to -\infty$ was in an initial eigenstate $\psi_{i,k_i}(\mathbf{r})$ of the asymptotic Hamiltonian at the *same* energy. Hence this electron has a positive momentum $\hbar k_i$ such that

$$E_i(k_i) = \epsilon_i + \frac{\hbar^2 k_i^2}{2m} \quad . \tag{3.8}$$

At the nanojunction, this state solution of (3.7) may be very complicated. Anyway, we expect that deep into the right lead it is a linear combination of eigenstates of the asymptotic H_R:

$$\Psi^+_{ik_i}(\mathbf{r}) \to \sum_{f=1}^{N_c^R} \mathcal{T}_{if}\psi_{fk_f}(\mathbf{r}), \quad x \to +\infty \quad , \tag{3.9}$$

where $\mathcal{T}_{if}$ are complex numbers.
Deep into the left lead the eigenfunction will be the sum of the incoming wave and contributions due to reflection at the interface:

$$\Psi^+_{ik_i}(\mathbf{r}) \to \psi_{ik_i}(\mathbf{r}) + \sum_{f=1}^{N_c^L} \mathcal{R}_{if}\psi_{fk_f}(\mathbf{r}), \quad x \to -\infty \quad , \tag{3.10}$$

where k_f are negative momenta which correspond to the same energy E_i of the incoming wave, and again $\mathcal{R}_{if}$ are complex numbers. We now calculate the current across a given surface S (perpendicular to z) carried by the wave $\Psi^+_{ik_i}(\mathbf{r})$. The current operator is defined as

$$\hat{I} = e\int_S d\mathbf{S}\cdot\hat{\mathbf{j}}(\mathbf{r},t) \quad . \tag{3.11}$$

We make the usual change $\mathbf{p} \to -i\hbar\partial/\partial\mathbf{r}$ and evaluate first the expectation value of the current density operator:

$$\begin{aligned}
\hat{\mathbf{j}}(\mathbf{r},t) =& \frac{1}{2m}\sum_i \{\delta(\mathbf{r}-\hat{\mathbf{r}}_\mathbf{i}), \hat{\mathbf{p}}_\mathbf{i}\} = \\
& \langle\Psi^+_{ik_i}|\hat{\mathbf{j}}(\mathbf{r})|\Psi^+_{ik_i}\rangle = \\
& \frac{\hbar}{2im}\left[[\Psi^+_{ik_i}(\mathbf{r})]^*\frac{\partial\Psi^+_{ik_i}(\mathbf{r})}{\partial z} - \Psi^+_{ik_i}(\mathbf{r})\frac{\partial[\Psi^+_{ik_i}(\mathbf{r})]^*}{\partial z}\right] = \\
& \frac{\hbar}{m}\left\{[\Psi^+_{ik_i}(\mathbf{r})]^*\frac{\partial\Psi^+_{ik_i}(\mathbf{r})}{\partial z}\right\} \quad .
\end{aligned} \tag{3.12}$$

If we integrate this expression over a plane perpendicular to the z direction and multiply by e we get the average current $I(E_i)$ carried by the state at energy E_i. Since we are considering

the system in an ideal steady state, the current $I(E_i)$ cannot depend on the position of the surface at which we evaluate it. We can evaluate it deep into the left (right) lead:

$$\begin{aligned} I_L(E_i) =& I_i(E_i) + \sum_{f=1}^{N_c^L} |\mathcal{R}_{if}|^2 I_f(E_i) = I_i(E_i) - \sum_{f=1}^{N_c^L} |\mathcal{R}_{if}|^2 |I_f(E_i)| = \\ & I_i(E_i) \left(1 - \sum_{f=1}^{N_c^L} R_{if}(E_i) \right) \quad , \end{aligned} \tag{3.13}$$

where we have defined

$$\begin{aligned} I_i(E_i) =& \frac{e\hbar}{2im} \int dx \int dy \left[\psi^*_{ik_i}(\mathbf{r}) \frac{\partial \psi_{ik_i}(\mathbf{r})}{\partial z} - \psi^*_{ik_i}(\mathbf{r}) \frac{\partial \psi^*_{ik_i}(\mathbf{r})}{\partial z} \right] \propto \\ & \hbar k_i / m \propto v_i(k_i) \quad . \end{aligned} \tag{3.14}$$

In a similar way, I_f, the currents reflected back into the left lead, are

$$I_f(E_i) \propto \hbar k_f / m \propto v_f(k_f) \quad , \tag{3.15}$$

which have opposite sign with respect to $I_i(E_i)$ as the vector k_f points toward the negative z versus. The quantity

$$R_{if}(E_i) \equiv |\mathcal{R}_{if}|^2 \frac{|I_f(E_i)|}{|I_i(E_i)|} \tag{3.16}$$

is known as the reflection probability for a wave incident with momentum $\hbar k_i$ to be scattered back into the left lead in a state with momentum $\hbar k_f$, while the energy is conserved.
In the same way one obtains that the transmission probability for the wave function with momentum $\hbar k_i$ to be transmitted in the right lead with final momentum $\hbar k_f$ reads:

$$T_{if}(E_i) \equiv |\mathcal{T}_{if}|^2 \frac{|I_f(E_i)|}{|I_i(E_i)|} \quad . \tag{3.17}$$

3.3.1 Total current

The total current across the junction can be calculated as the sum of all currents carried by all states at all energies. This can be done by multiplying by the density of states for each momentum direction, and summing over all incident channels. If one defines the *transmission coefficients* at a given energy:

$$T_{RL}(E) = \sum_{i=1}^{N_c^R} \sum_{f=1}^{N_c^L} T_{if}(E) \qquad \text{from R to L} \quad , \tag{3.18}$$

$$T_{LR}(E) = \sum_{i=1}^{N_c^L} \sum_{f=1}^{N_c^R} T_{if}(E) \qquad \text{from L to R} \quad , \tag{3.19}$$

it is possible to obtain an expression of the total current:

$$I = \frac{e}{\pi\hbar} \int dE \left\{ T_{LR}(E) - T_{RL}(E) \right\} \quad . \tag{3.20}$$

If the left and right channels are equally populated, the total current is zero, as the same amount of carriers flow in the two directions. In fact, since the particle flux must be conserved, we it must be

$$T_{LR}(E) = T_{RL}(E) \equiv= T(E) \quad . \tag{3.21}$$

Anyway, if the left and right leads are populated with two different local distribution functions (and thus have two different electrochemical potentials), the total currents differs from zero and Eq. (3.20) becomes:

$$I = \frac{\mathrm{G}_0}{e} \int_{-\infty}^{+\infty} dE \left[f_L(E) - f_R(E) \right] T(E) \quad , \tag{3.22}$$

where we define the quantity $\mathrm{G}_0 = 2e^2/h$ as the *quantum of conductance*. The latter equation is usually called the Landauer equation. Considering that the voltage drop is defined as $V = \frac{\mu_L - \mu_R}{e}$, it is possible to calculate the conductance G from Eq. (3.22) assuming for semplicity that the temperature is zero:

$$\mathrm{G}(E) = \frac{dI}{dV} = \frac{d}{dV} \left[\frac{\mathrm{G}_0}{e} \int_{\mu_L}^{\mu_R} dE \; T(E) \right] = \frac{\mathrm{G}_0}{e} eT(E) = \mathrm{G}_0 T(E) \quad . \tag{3.23}$$

3.3.2 Zero bias limit

In the zero bias limit, namely if $(\mu_L - \mu_R) \to 0$, Eq. (3.22) can be simplified. If we Taylor-expand the local distribution function:

$$f_L(E) = f_R(E) - \frac{\partial f_R(E)}{\partial E}|_{\mu_R} (\mu_L - \mu_R) + \mathcal{O}[(\mu_L - \mu_R)^2] \tag{3.24}$$

we can insert the latter expression in Eq. (3.22):

$$I = \frac{2e}{h} (\mu_L - \mu_R) \int dE \left(-\frac{\partial f_R(E)}{\partial E}|_{\mu_R} \right) T(E), \qquad (\mu_L - \mu_R) \to 0 \quad . \tag{3.25}$$

If we set the electronic temperature to zero, the Fermi dirac distribution f_R becomes a step function, and its energy derivative is a δ-function centered at μ_R. Thus

$$I = \frac{2e}{h} (\mu_L - \mu_R) T(E = \mu_R) = \frac{2e^2}{h} T(E_F) \Delta V; \qquad \mu_L - \mu_R \to 0, \quad \Theta \to 0 \quad , \tag{3.26}$$

where $\Delta V = \mu_L - \mu_R$ is the applied bias. For this reason, very often we focus on the zero-bias transmission function near the Fermi level, that is the region where the real transport takes place at low biases.

3.4 Non Equilibrium Green's functions

What we have discussed so far is a standard derivation of the Landauer formula. In solid state physics, non equilibrium Green's function methods are used to calculate current and charge densities in nanoscale (both molecular and semiconductor) conductors under bias. In

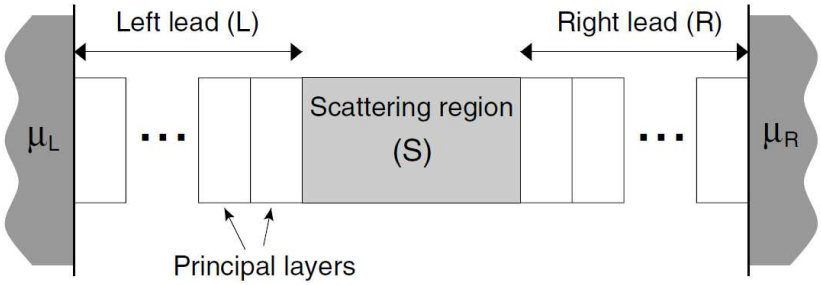

Figure 3.3: Schematic setup used to study phase coherent transport. The system is divided in three regions: a central scattering region (S) between two left (L) and right (R) leads connected to thermal reservoir with chemical potentials μ_L and μ_R. The leads are perfectly periodic and can be represented as a sequence of periodically repeated principal layers [34].

this Section we will summarize such methods [33], showing how the Landauer approach can be recast in terms of Green's functions, which is a practical way to calculate the transmission properties in many realistic cases. Let us suppose to be able to divide the space into three regions: two semi infinite left and right (L, R) leads connected to a central scattering region (S), as depicted in Fig. 3.3. The leads are assumed to be perfect conductors and thus the electron move ballistically in these regions and can scatter only on the potential inside S. We separate the Hamiltonian and the wavefunction of the system into contact $(H_{L,R}, |\psi_{L,R}\rangle)$ and scattering region$(H_S, |\psi_S\rangle)$ subspaces:

$$\begin{pmatrix} H_L & \tau_L & 0 \\ \tau_L^\dagger & H_S & \tau_R^\dagger \\ 0 & \tau_R & H_R \end{pmatrix} \begin{pmatrix} |\psi_L\rangle \\ |\psi_S\rangle \\ |\psi_R\rangle \end{pmatrix} = E \begin{pmatrix} |\psi_L\rangle \\ |\psi_S\rangle \\ |\psi_R\rangle \end{pmatrix} \tag{3.27}$$

where $\tau_{L,R}$ are the hopping terms describing the interaction between device and contacts. Here we will assume that the contacts are independent, i.e., there are no cross terms τ between the different L and R contacts. We can define the Green's function of the system as the resolvent of H [35]:

$$(E - H)G(E) = I \quad . \tag{3.28}$$

The Green's function gives the response of a system to a constant perturbation $|\nu\rangle$ in the Schrödinger equation

$$H|\psi\rangle = E|\psi\rangle + |\nu\rangle \quad . \tag{3.29}$$

The response to this perturbation is

$$\begin{aligned} (E - H)|\psi\rangle &= -|\nu\rangle \quad , \\ |\psi\rangle &= -G(E)|\nu\rangle \quad . \end{aligned} \tag{3.30}$$

For example, from third row of Eq. 3.27:

$$\begin{aligned} H_R|\psi_R\rangle + \tau_R|\psi_S\rangle &= E|\psi_R\rangle \\ (E - H_R)|\psi_R\rangle &= \tau_R|\psi_S\rangle \\ \Rightarrow |\psi_R\rangle &= g_R(E)\tau_R|\psi_S\rangle \quad , \end{aligned} \tag{3.31}$$

where g_R is the Green's function of the isolated R electrode: $(E-H_R)g_R = I$. It is important to note that since we have an infinite system, we obtain two types of solutions for the Green's functions, the retarded and the advanced solutions corresponding to outgoing and incoming waves in the contacts. These two solutions are usually obtained by respectively adding an infinitesimal positive or negative imaginary part to the energy. We will denote the retarded Green's function with G and the advanced one with $G^\dagger$. Here, capital G denotes the full Green's function and its sub-matrices G_R, G_{RS} etc. Lowercase is used for the Green's functions of the isolated subsystems, e.g., $(E - H_L)g_L = I$. By using the retarded Green's function of the isolated contact (g_R) in Eq. (3.31) we obtain the solution corresponding to an outgoing wave in the contact. Using the advanced Green's function ($g_R^\dagger$) would produce the solution corresponding to an incoming wave.

3.4.1 Self-energy

Calculating the Green's function is easier than solving the full Schrödinger equation. Also, the Green's function of the scattering region can be calculated separately without calculating the Green's function of the full region.
From the definition of the Green's function one obtains:

$$\begin{pmatrix} E-H_L & -\tau_L & 0 \\ -\tau_L^\dagger & E-H_S & -\tau_R^\dagger \\ 0 & -\tau_R & E-H_R \end{pmatrix} \begin{pmatrix} G_L & G_{LS} & G_{LR} \\ G_{SL} & G_S & G_{SR} \\ G_{RL} & G_{RS} & G_R \end{pmatrix} = \begin{pmatrix} I & 0 & 0 \\ 0 & I & 0 \\ 0 & 0 & I \end{pmatrix} \quad . \tag{3.32}$$

From the set of three equations in the second column:

$$\begin{aligned} (E-H_L)G_{LS} - \tau_L G_S &= 0 \\ -\tau_L^\dagger G_{LS} + (E-H_S)G_S - \tau_R^\dagger G_{RS} &= I \\ (E-H_R)G_{RS} - \tau_R G_S &= 0 \quad . \end{aligned} \tag{3.33}$$

From the first and third row of Eq 3.33 we obtain:

$$\begin{aligned} G_{LS} &= g_L \tau_L G_S \\ G_{RS} &= g_R \tau_R G_S \quad . \end{aligned} \tag{3.34}$$

Now, if we substitute these expression into the central equation of Eq (3.33):

$$-\tau_L^\dagger g_L \tau_L G_S + (E-H_S)G_S - \tau_R^\dagger g_R \tau_R G_S = I \quad , \tag{3.35}$$

from which we can find G_S:

$$G_S = ((E+i\eta) - H_S - \Sigma_L - \Sigma_R)^{-1} \quad , \tag{3.36}$$

where we have explicitely written the imaginary part η of the energy. The terms $\Sigma_L = \tau_L^\dagger g_L \tau_L$ and $\Sigma_R = \tau_R^\dagger g_R \tau_R$ are the self-energies of the left and right leads. So the effect of the semi-infinite contacts to the central region is replaced by adding the two self-energies to

the Hamiltonian. Now the matrices in Eq. (3.36) have all a finite size. It may seem that we have not gained much, since to obtain the self energies one needs to calculate $g_{L,R}$ and thus to invert infinite matrices. However, assuming the leads to be periodic, in all practical calculations this can be easily overcome by using recursive methods [36].

3.4.2 The spectral function

The spectral function is defined as:

$$A = i(G - G^\dagger) \quad . \tag{3.37}$$

This is one of the most important quantities we will use, since it contains information about the density of states (DOS) and all solutions to the Schrödinger equation. In fact, we note that for any perturbation $|\nu\rangle$ we get two solutions $|\psi^r\rangle$ and $|\psi^a\rangle$ to the Schrödinger equation:

$$(E - H)|\psi\rangle = -|\nu\rangle \tag{3.38}$$

from the advanced and retarded Green's functions:

$$\begin{aligned} |\psi^r\rangle &= -G|\nu\rangle \\ |\psi^a\rangle &= -G^\dagger|\nu\rangle \end{aligned} \tag{3.39}$$

The difference of these solutions is a solution to the Schrödinger equation:

$$(E - H)(|\psi^r\rangle - |\psi^a\rangle) = (E - H)(G - G^\dagger)|\nu\rangle = (I - I)|\nu\rangle = 0 \quad , \tag{3.40}$$

which means that $|\psi\rangle = A|\nu\rangle$ is a solution to the Schrödinger equation for any vector $|\nu\rangle$. To show that the spectral function actually gives all solutions to the Schrödinger equation we expand the Green's function in the basis set of the eigenvectors $\{|k\rangle\}$:

$$G = \frac{1}{E + i\eta - H} = \sum_k \frac{|k\rangle\langle k|}{E + i\delta - \epsilon_k} \quad , \tag{3.41}$$

where we have added a small imaginary part η to the energy as discussed above, and $|k\rangle$ are all the eigenvectors of H with eigenenergies ϵ_k. Expanding the spectral function in the eigenbasis gives:

$$\begin{aligned} A &= i\left(\frac{1}{E + i\eta - H} - \frac{1}{E - i\eta - H}\right) \\ &= i\sum_k |k\rangle\langle k| \left(\frac{1}{E + i\eta - \epsilon_k} - \frac{1}{E - i\eta - \epsilon_k}\right) \\ &= \sum_k |k\rangle\langle k| \frac{2\eta}{(E - \epsilon_k)^2 + \eta^2} \quad . \end{aligned} \tag{3.42}$$

In the limit $\eta \to 0$ we get

$$A = 2\pi \sum_k \delta(E - E_k)|k\rangle\langle k| \quad , \tag{3.43}$$

which is the spectral density of states. Integrating over k one obtains the total density of states.

3.4.3 Response to an incoming wave

In the non-equilibrium case, reservoirs with different chemical potentials will inject electrons which will occupy the states corresponding to incoming waves in the contacts. Therefore, we want to find the solutions corresponding to these incoming waves. Consider contact L isolated from the other contacts and the device. At a given energy we have solutions corresponding to an incoming wave that is *totally reflected* at the end of the contact. We will denote these solutions with $|\psi_{L,n}\rangle$ where L is the contact label and n is a quantum number. We can find all these solutions from the spectral function a_L of the isolated contact, which can be calculated by Eq. (3.42). Connecting the contacts to the device we can calculate the wavefunction on the whole system caused by the incoming wave in contact L. To do this we note that a wavefunction should be of the form

$$|\psi_{L,n}\rangle + |\psi^r\rangle$$

where $|\psi_{L,n}\rangle$ is the totally reflected wave and $|\psi^r\rangle$ is the retarded response of the whole system. In particular, $|\psi^r\rangle$ has also contributions in region L, otherwise the solution in that region would remain $|\psi_{L,n}\rangle$. We will adopt the ansatz of considering the scattering state $|\psi_{L,n}\rangle + |\psi^r\rangle$ as a solution of the Hamiltonian. If we substitute that state into the Schrödinger equation we get:

$$\begin{aligned}
\begin{pmatrix} H_L & \tau_L & 0 \\ \tau_L^\dagger & H_S & \tau_R^\dagger \\ 0 & \tau_R & H_R \end{pmatrix} (|\psi_{L,n}\rangle + |\psi^r\rangle) &= E(|\psi_{L,n}\rangle + |\psi^r\rangle) \\
\begin{pmatrix} E|\psi_{L,n}\rangle \\ \tau_L^\dagger|\psi_{L,n}\rangle \\ 0 \end{pmatrix} + \begin{pmatrix} H_L & \tau_L & 0 \\ \tau_L^\dagger & H_S & \tau_R^\dagger \\ 0 & \tau_R & H_R \end{pmatrix} |\psi^r\rangle &= E(|\psi_{L,n}\rangle + |\psi^r\rangle) \\
H|\psi^r\rangle &= E|\psi^r\rangle) - \tau_L^\dagger|\psi_{L,n}\rangle
\end{aligned} \tag{3.44}$$

We see that $|\psi^r\rangle$ is the response of the whole system to a perturbation of $-\tau_L^\dagger|\psi_{L,n}\rangle$ (by a comparison of last row of Eq (3.31)):

$$|\psi^r\rangle = (E - H)^{-1}\tau_L^\dagger|\psi_{L,n}\rangle = G\tau_L^\dagger|\psi_{L,n}\rangle \quad , \tag{3.45}$$

with G being the Green's function of the infinite $(L + S + R)$ system. The scattering states generated from Eq. (3.45), using all possible incoming waves from each contact, form a complete orthonormal set of solutions of the full Schrödinger equation. Note that we have chosen the retarded response which means that the incoming wave (part of $|\psi_{L,n}\rangle$) is traveling towards the device. We will make full use of this fact below. The full wavefunction can thus be expressed as:

$$|\psi\rangle = |\psi_{L,n}\rangle + G\tau_L^\dagger|\psi_{L,n}\rangle \quad . \tag{3.46}$$

We would like to calculate the expressions for the wavefunction in the scattering region $|\psi_S\rangle$ and in the contact region $|\psi_{L,R}\rangle$. The scattering region part is simply derived from Eq. (3.46) by noting that $|\psi_{L,n}\rangle$ has not contribution in that region:

$$|\psi_S\rangle = G_S\tau_L^\dagger|\psi_{L,n}\rangle \quad , \tag{3.47}$$

and from Eq. (3.31) and Eq. (3.34)

$$|\psi_R\rangle = g_R\tau_R|\psi_S\rangle = g_R\tau_R G_S\tau_L^\dagger|\psi_{L,n}\rangle \quad . \tag{3.48}$$

Note that to calculate the wavefunction in the contact containing the incoming wave (contact L) we need to add the incoming wave, giving the following expression:

$$|\psi_L\rangle = (1 + g_L\tau_L G_S\tau_L^\dagger)|\psi_{L,n}\rangle \quad . \tag{3.49}$$

Knowing the wavefunctions corresponding to incoming waves in different contacts enables us to fill up the different solutions according to the electron reservoirs filling the contacts.

3.4.4 Charge density matrix

We now calculate the charge density when the system is in a non-equilibrium state (otherwise, it can be easily derived from the spectral function a_S). The charge density matrix is defined as:

$$\rho = \sum_k f(k,\mu)|\psi_k\rangle\langle\psi_k| \quad , \tag{3.50}$$

where the sum runs over all states with the occupation number $f(E_k,\mu)$. The occupation number is determined by the reservoirs filling the incoming waves in the contacts such that:

$$f(E_k,\mu_L) = \frac{1}{1 + e^{(E_k-\mu_L)/k_B\Theta}} \tag{3.51}$$

is the Fermi-Dirac function with the chemical potential μ_L and the temperature Θ of the reservoir responsible for injecting the electrons into the contacts. From Eq. (3.47), the wavefunction in the scattering region given by an incoming wave in contact L is:

$$|\psi_{S,k}\rangle = G_S\tau_L^\dagger|\psi_{L,k}\rangle \quad . \tag{3.52}$$

Adding up all states from contact L and using Eq. (3.43) gives:

$$\begin{aligned}
\rho_S(\text{contact } L) &= \int dE \sum_k f(E,\mu_L)\delta(E-E_k)|\psi_{S,k}\rangle\langle\psi_{S,k}| \\
&= \int dE \sum_k f(E,\mu_L)\delta(E-E_k)G_S\tau_L^\dagger|\psi_{L,k}\rangle\langle\psi_{L,k}|\tau_L G_S^\dagger \\
&= \int dE f(E,\mu_L)G_S\tau_L^\dagger\left(\sum_k \delta(E-E_k)|\psi_{L,k}\rangle\langle\psi_{L,k}|\right)\tau_L G_S^\dagger \\
&= [\text{vd. } \quad 3.43] = \int dE f(E,\mu_L)G_S\tau_L^\dagger\frac{a_L}{2\pi}\tau_L G_S^\dagger \quad ,
\end{aligned} \tag{3.53}$$

which, after defining the quantity $\Gamma_L = \tau_L^\dagger a_L \tau_L = i\left(\Sigma_L - \Sigma_L^\dagger\right)$ can be rewritten as:

$$\rho_S(\text{contact } L) = \frac{1}{2\pi}\int dE f(E,\mu_L) G_S \Gamma_L G_S^\dagger \quad . \tag{3.54}$$

Note that this is the density operator on the scattering region which has contributions only from the states incident from the left side. The total charge density thus becomes a sum over all contacts:

$$\rho_S(\text{contact } L) = \frac{2 \quad (\text{spin})}{2\pi}\int dE \sum_i f(E,\mu_i) G_S \Gamma_i G_S^\dagger \tag{3.55}$$

3.4.5 Probability current

In presence of a bias the chemical potential difference between L, R leads gives rise to a finite current. In the next section we will calculate this current in a similar way as the charge density. In order to do this we need an expression for the current from the wavefunction. In the continuum case we can calculate the current from the velocity operator. However, for a discrete Hamiltonian it is not straightforward how to define a velocity operator. Therefore, we derive an expression for the current from the continuity equation (using two contacts). In steady-state, the probability to find an electron on the scattering region S ($\sum_{i\in S}|\langle i|\psi\rangle|^2 = \sum_{i\in S}|\psi|^2$, where the sum runs over the device subspace) is conserved:

$$\begin{aligned}
0 &= \frac{\partial \sum_i |\psi|^2}{\partial t} = \sum_i \frac{\partial \langle\psi|i\rangle\langle i|\psi\rangle}{\partial t} = \sum_i \left(\frac{\partial\langle\psi|i\rangle}{\partial t}\langle i|\psi\rangle + \langle\psi|i\rangle\frac{\partial\langle i|\psi\rangle}{\partial t}\right) \\
&= \frac{i}{h}\sum_i \left(\langle\psi|H|i\rangle\langle i|\psi\rangle - \langle\psi|i\rangle\langle i|H|\psi\rangle\right) = \frac{i}{h}\left(\langle\psi|H|\psi_S\rangle - \langle\psi_S|H|\psi\rangle\right) \\
&= \frac{i}{h}\left(\langle\psi|H_S + \tau_L + \tau_R\psi_S\rangle - \langle\psi_S|H_S + \tau_L^\dagger + \tau_R^\dagger\psi\rangle\right) \\
&= \frac{i}{h}\left(\left[\langle\psi_L|\tau_L|\psi_S\rangle - \langle\psi_S|\tau_L^\dagger|\psi_L\rangle\right] + \left[\langle\psi_R|\tau_R|\psi_S\rangle - \langle\psi_S|\tau_R^\dagger|\psi_R\rangle\right]\right)
\end{aligned} \tag{3.56}$$

We interpret the term in the first (square) bracket as the incoming probability current into the device from contact L and the second bracket from contact R. Generalizing to an arbitrary contact j gives us the electric current (at one energy) as the charge $(-e)$ times the probability current:

$$i_j = -\frac{ie}{\hbar}\left(\langle\psi_j|\tau_j|\psi_S\rangle - \langle\psi_S|\tau_j^\dagger|\psi_j\rangle\right) \quad , \tag{3.57}$$

where i_j is defined as positive for a current from the contacts into the device. We can now put in the expressions for the wavefunctions in the same way as for the density matrix.

3.4.6 Electrical current

To calculate the total current through the device we only need to put in the wavefunction of the device and the contacts ($\psi_S, \quad \psi_L, \quad \psi_R$) from Eqs. (3.47), (3.49) and (3.31) and adding

all the contributions together. Thus the current into the device from a incoming wave of one energy (E) in contact L ($|\psi_{L,n}\rangle$) through the coupling defined by τ_R is:

$$\begin{aligned} i_{(2 \quad \text{from} \quad 1)} &= -\frac{ie}{\hbar}\left[\langle\psi_R|\tau_R|\psi_S\rangle - \langle\psi_S|\tau_R^\dagger|\psi_R\rangle\right] \\ &= -\frac{ie}{\hbar}\left[\langle\psi_{L,n}|\tau_L G_S^\dagger \tau_R^\dagger g_R^\dagger \tau_R G_S \tau_L^\dagger|\psi_{L,n}\rangle - \langle\psi_{L,n}|\tau_L G_S^\dagger \tau_R^\dagger g_R \tau_R G_S \tau_L^\dagger|\psi_{L,n}\rangle\right] \\ &= -\frac{ie}{\hbar}\langle\psi_{L,n}|\tau_L G_S^\dagger \tau_R^\dagger \left(g_R^\dagger - g_R\right)\tau_R G_S \tau_L^\dagger|\psi_{L,n}\rangle \\ &= -\frac{e}{\hbar}\langle\psi_{L,n}|\tau_L G_S^\dagger \Gamma_R G_S \tau_L^\dagger|\psi_{L,n}\rangle \end{aligned} \tag{3.58}$$

Adding over the states n and noting that the levels are filled from the reservoir connected to contact L gives (2 for spin):

$$\begin{aligned} I_{(2 \quad \text{from} \quad 1)} &= 2\frac{e}{\hbar}\int_{E=-\infty}^{+\infty} dE f(E,\mu_L)\sum_n \delta(E-E_n)\langle\psi_{L,n}|\tau_L G_S^\dagger \Gamma_R G_S \tau_L^\dagger|\psi_{L,n}\rangle \\ &= 2\frac{e}{\hbar}\int_{E=-\infty}^{+\infty} dE f(E,\mu_L)\sum_{m,n} \delta(E-E_n)\langle\psi_{L,n}|\tau_L|m\rangle\langle m|G_S^\dagger \Gamma_R G_S \tau_L^\dagger|\psi_{L,n}\rangle \\ &= 2\frac{e}{\hbar}\int_{E=-\infty}^{+\infty} dE f(E,\mu_L)\sum_m \langle m|G_S^\dagger \Gamma_R G_S \tau_L^\dagger \left(\sum_n \delta(E-E_n)|\psi_{L,n}\rangle\langle\psi_{L,n}|\right)\tau_L|m\rangle \\ &= 2\frac{e}{\hbar}\int_{E=-\infty}^{+\infty} dE f(E,\mu_L)\sum_m \langle m|G_S^\dagger \Gamma_R G_S \tau_L^\dagger \frac{a_L}{2\pi}\tau_L|m\rangle \\ &= \frac{e}{\pi\hbar}\int_{E=-\infty}^{+\infty} dE f(E,\mu_L)\mathrm{Tr}\left(G_S^\dagger \Gamma_R G_S \Gamma_L\right) \end{aligned} \tag{3.59}$$

To get the total current through the device the current from contact R have to be subtracted away:

$$I = \frac{e}{\pi\hbar}\int_{E=-\infty}^{+\infty} dE\left(f(E,\mu_L) - f(E,\mu_R)\right)\mathrm{Tr}\left[G_S^\dagger \Gamma_R G_S \Gamma_L\right] \tag{3.60}$$

The quantity

$$T(E) = \mathrm{Tr}\left[G_S^\dagger \Gamma_R G_S \Gamma_L\right] \tag{3.61}$$

is the transmission function of the system.

3.4.7 Practical Calculations

The formalism presented so far can be used in combination with DFT calculations. The general scheme is the following. By using a localized basis set, it is possible to do a partition of the system in a left, scattering, and right region as in Fig. 3.3. The self-energies $\Sigma_{L,R}$ are provided by a self consistent calculation of the electrode principal layer, with periodic boundary conditions along all the three direction. Then, it is possible to compute the scattering Green's function (3.36) with the Hamiltonian evaluated at a given charge density ρ_0 [b].

[b] For example, the starting ρ_0 can be the one obtained by a preliminar self-consistent calculation of the scattering region with periodic boundary conditions along z.

With the expression in Eq (3.55) we can compute the non-equilibrium charge in the device region of a junction. In practice, this integral is performed by splitting it into two parts: an equilibrium part which can be integrated along a contour in the complex plane and a nonequilibrium part which has to be integrated along the real energy axis [37]. This is due to the fact that the L, R spectral densities $\rho_{L,R} = \frac{1}{\pi} G_S \Gamma_{L,R} G_S^*$ (which appear as the arguments of the energy integral) are not analytical. Afterwards, from the Green's function G a new charge density ρ_1 can be calculated, which is then used to construct the new Hamiltonian $H_S(\rho_1)$. This procedure is iterated until reaching self-consistency, that is when $\rho_{n+1} = \rho_n$. A fundamental requirement is that the final self-consistent density matrix matches exactly that of the leads at the boundaries. Therefore one tipically enlarges the scattering region to contain a few principal layers of the leads (those where the electronic structure is different from that of the bulk)[c] as depicted in Fig. 3.3. Finally, the converged Green's function can be used to calculate (i) the transmission function T(E) and (ii) the current I through the device as shown in Eq. (3.60).
All the transport calculations presented in this thesis work are performed with the TranSIESTA code [38].

[c] The exact number of such planes depends on the screening length of the material considered.

Chapter 4

Transport on a 1D system: a simplified model

Before applying the NEGF technique to study conductance of realistic systems, we study the Landauer theory for a simplified model. Here, our interest is not to perform a conductance calculation for a realistic system, but rather to grasp the main features of electronic transport across interfaces by using a very simple model and a formally exact approach for the calculation of the Green's function. At a basic level, the simplest example of a nanoscale junction is an atom/molecule embedded between two leads. Of course, this is a 3-dimensional system, but the underlying physics can be understood by considering a one dimensional potential, which properly simulates the effects of the two semi-infinite leads and the presence of the atom/molecule discrete energy levels. We will consider one dimensional potentials which can be of any shape inside a well defined scattering region, while they remain constant outside that region in order to reproduce jellium electrodes. Inside the scattering region, we will consider single barrier as well as double barrier potentials which yield electronic resonances. The Green's function of the infinite system will be numerically calculated by means of the embedding theory, which will be summarized before showing the results. Except when differently specified, along this chapter we will make use of the atomic units ($e = m_e = \hbar = 1$).

4.1 Embedding approach

Embedding is a theory that allows one to calculate the Green's function in a limited region of space (region I), taking into account the effect of the rest of the space (region II) to region I [39]. This is done by adding to the Hamiltonian an embedding potential defined over the interface between regions I and II, which includes the effect of the infinite substrate. This potential ensures that the wave functions have the correct boundary conditions on the surface between I and II, allowing them to match with the wavefunctions of the substrate.
This method is perfectly suitable to reproduce an interface potential between two infinite leads. In fact, we may solve the Schrödinger equation only in a region containing the junc-

tion between the leads and, to a first approximation, we may consider two jellium leads with constant potential, initially set to zero. In this case, the embedding potential is calculated on the two surfaces (left and right), which in one dimension reduce to two points, z_l and z_r (Fig. 4.1).

If we call S the surface separating regions I and II, and if n_S is a normal vector pointing out-

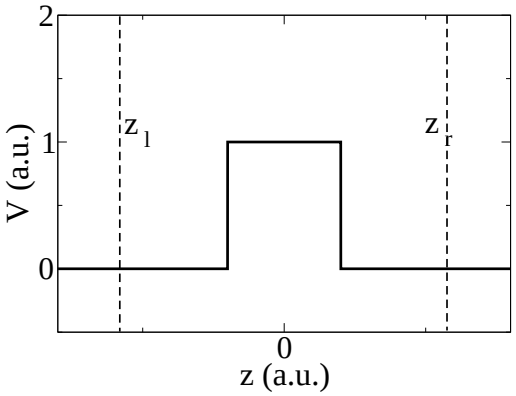

Figure 4.1: Example of embedding surfaces in one dimension, situated at $z = z_l$ and $z = z_r$.

ward S, we denote the embedding potentials for the left and right half spaces by $\Sigma(\mathbf{r}_S, \mathbf{r'}_S; E)$. Σ is a complex matrix defined on the surface S giving a generalized logarithmic derivative on S of solutions ψ of the Schrödinger equation in region II satisfying the outgoing boundary condition at $z = \pm\infty$ [39]: the embedding potential

$$\frac{\partial\psi(\mathbf{r}_S)}{\partial n_S} = -2\int_S d\mathbf{r}_S \Sigma(\mathbf{r}_S, \mathbf{r'}_S; E)\psi(\mathbf{r}_S) \quad , \tag{4.1}$$

where the normal n points outwards region I. The equation for the Green's function G in the embedding formalism is:

$$\begin{aligned} &-\frac{1}{2}\nabla^2_{\mathbf{r}} G(\mathbf{r}, \mathbf{r'}; E) + \frac{1}{2}\delta(n - n_S)\frac{\partial G(\mathbf{r}, \mathbf{r'}; E)}{\partial n_S} + V(\mathbf{r})G(\mathbf{r}, \mathbf{r'}; E) \\ &+ \delta(n - n_S)\int_S d\mathbf{r''}_S \Sigma(\mathbf{r}_S, \mathbf{r''}_S; E)G(\mathbf{r''}, \mathbf{r'}; E) - EG(\mathbf{r}, \mathbf{r'}; E) \\ &= \delta(\mathbf{r} - \mathbf{r'}) \qquad \mathbf{r}, \mathbf{r'} \ \text{ in } \ \text{I}. \end{aligned} \tag{4.2}$$

The reader may notice that, unlike the formalism described in Chap. 3, now we are expanding all the equations in real space. We will work in real space only in this chapter.

4.1.1 Numerical solution

In order to solve Eq. (4.2), we cast it in a matrix form.
First, we expand the Green's function G on a basis set χ_i:

$$G(z, z'; E) = \sum_{i,j} \chi_i(z)\chi_j(z')G_{ij}(E). \tag{4.3}$$

Then, Eq. (4.2) reduces to a matrix equation (see Appendix A):

$$\sum_j \left(H_{ij} + \Sigma_{ij}(E) - ES_{ij}\right) G_{jk} = \delta_{ik}, \tag{4.4}$$

where the Hamiltonian matrix is given by [40]:

$$H_{ij} = \frac{1}{2}\int_{z_l}^{z_r} dz \frac{d\chi_i(z)}{dz}\frac{d\chi_j(z)}{dz} + \int_{z_l}^{z_r} dz \chi_i(z) V(z) \chi_j(z), \tag{4.5}$$

the embedding matrix by:

$$\Sigma_{ij}(E) = \Sigma_l(E)\chi_i(z_l)\chi_j(z_l) + \Sigma_r(E)\chi_i(z_r)\chi_j(z_r), \tag{4.6}$$

and the overlap matrix S by:

$$S_{ij} = \int_{z_l}^{z_r} dz \chi_i(z)\chi_j(z) \quad . \tag{4.7}$$

We use a trigonometric basis functions,

$$\chi_n(z) = \begin{cases} \cos(\frac{m\pi\zeta}{2D}) & n \quad \text{even} \\ \sin(\frac{m\pi\zeta}{2D}) & n \quad \text{odd} \end{cases} \tag{4.8}$$

where ζ is measured from the mid point of region I,

$$\zeta = z - \frac{z_r + z_l}{2} \tag{4.9}$$

and where $D > (z_r - z_l)/2$. With this approach, one obtains the 1D Green's function $G(z, z', E)$. In the case of translational invariance in the (x, y) plane, one can extend this result and obtain the full Green's function $G(\mathbf{r}, \mathbf{r'}, E)$ (see Appendix B) and then compute the relevant physical quantities such as the density of states or the charge density.

4.1.2 Ballistic transport

The conductance G (see Eq. (3.23)) can be expressed in an efficient way by using the embedding approach [41, 42]. With a derivation similar to what shown in the previous chapter, it can be shown that the conductance may be written in terms of the embedding potentials as [42]:

$$\mathrm{G} = 2\mathrm{G}_0 \mathrm{Tr}\left[G_{12}\mathrm{Im}\Sigma_2 G_{21}^* \mathrm{Im}\Sigma_1\right], \tag{4.10}$$

where G is the outgoing (retarded) Green's function of the system, the indices $(1, 2)$ refer to two boundary surfaces $S_{1,2}$, $G_{12} = G(\mathbf{r}_1, \mathbf{r}_2)$ is evaluated with one argument on the first surface and the other on the second one (the integral on the repeated variables is implicit), and Σ is the embedding potential defined in Eq. (4.1). Eq. (4.10) is the same as Eq. (3.61): here, the embedding potential plays the role of the self-energy derived quantity Γ. Having an expression for the conductance, it is then possible to calculate the current. If we assume near-zero temperatures, we can approximate the Fermi functions f with step functions and

the current is approximated by the integral between the two leads chemical potentials (see Eqs. (3.22), (3.23)):

$$I(V) = \frac{1}{e}\int_{\mu_1}^{\mu_2} \mathrm{G}(E,V)dE \quad . \tag{4.11}$$

We have explicitly shown the dependence of the conductance on the voltage V. In fact, the Green's function is computed at any given voltage V, and thus G is updated to calculate $I(V)$.

4.2 Resonant Tunneling

A strategy to investigate the effects to the conductance due to the presence of an atom or a molecule between two leads is to study a simple system which reproduces the presence of discrete levels. Our choice is to study the conductance of a double barrier potential: the two barriers represent the vacuum regions between the molecule/atom and the two electrodes, while in the mid-region a set of quasi-localized levels is present. The fact that a potential well yields discrete electronic levels is an elementary quantum physics exercise. The same happens for a double barrier potential, where the height of the barriers is infinite. If we immagine to reduce the barriers height from infinite to a finite value, localized electron states in the interface hybridize with the continuum of electron states at the left and right sides of the resulting well, forming electronic *resonances*. By using the embedding formalism, the resonance width due to the coupling with semiinfinite substrates is correctly calculated.

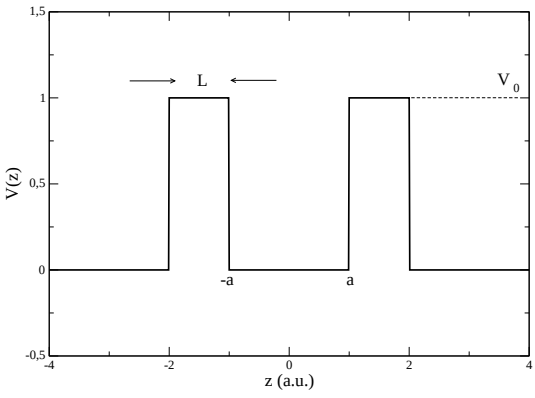

Figure 4.2: Double rectangular barrier potential.

In the following, we will consider a double rectangular barrier (Fig. 4.2). But note that with our approach we can simulate whatever potential profile we prefer. Let us call a the semiamplitude of the resulting well, V_0 the intensity of the two barriers, and L their width. In Fig. 4.3 the local density of states (LDOS) is shown for a potential profile with $V_0 = 1Ha$ and $a = 1a_0$. We see that for $z \simeq 0$ the LDOS has a sharp peak for $E \cong 0.4Ha$ due to the bound state of the well. The peak is not perfectly localized in energy, but it has a

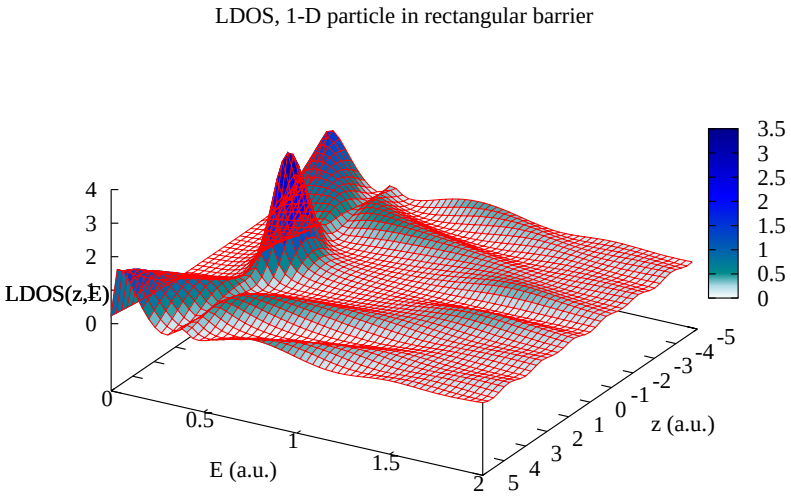

Figure 4.3: LDOS for an electron in a double potential barrier ($V_0 = 1$ Ha, $a = 1\ a_0$), calculated versus several points z.

broadening that is due to the hybridization with the continuum of states of the substrate, as described before. For values of z which are far from the barriers, the energy dependence of the LDOS approaches that of the free particle ($\propto 1/\sqrt{E}$) with an oscillatory behaviour. If we increase the distance between the two barriers, i.e. if we increase the well's width, we

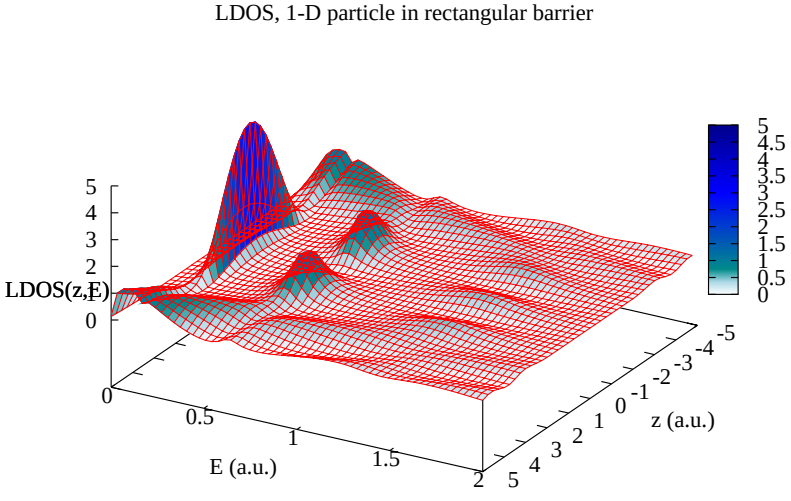

Figure 4.4: LDOS for an electron in a double potential barrier ($V_0 = 1$ Ha, $a = 2\ a_0$), calculated versus several points z .

find more bound states. For example, Fig. 4.4 shows the LDOS in the case of two barriers with $a = 2a_0$: here two resonances are clearly visible, the second having zero probability

at $z = 0$ since its wavefunction has an odd-symmetry. The first peak has a lower energy in this case, as expected for a wider well potential, and it is less broadened if compared to the case of $a = 1a_0$ (Fig. 4.3): the first bound state is less hybridized with the substrate because the barriers are wider and so its wavefunction may decay closer to zero inside them. In both cases we also notice the presence of continuum resonances corresponding to energies $E > V_0$, whose wavefunctions display opposite parity with respect to the higher bound state.

In Fig. 4.5 we show the LDOS at the position $z = 0$ and the $k_{\parallel} = 0$ conductance for several configurations of double square potentials, changing the geometrical parameters that characterize it (L, V_0, and a). In panel a) we see that if we increase the distance between the two barriers, the resonances shift to lower energies and their width is narrowed. As expected, by increasing V_0 the peak moves to higher energies (panel c). Finally, if the barrier width L is increased, the resonance energy remains unchanged, but it gets sharper because the electron has a lower probability to escape from the well (panel e). The behaviour of the conductance in a one dimensional double square potential follows that of the LDOS (panels b-d-f). In corrispondence of the resonance energies, the conductance G yields high peaks. Such features are broadened as well as the resonances in the potential well. For energies approaching V_0, G starts to oscillate in the same way as the case of a single potential barrier, the oscillations getting narrower the higher the energy (see Fig. 4.6). In conclusion, the main difference between the conductance for a single and a double barrier potential is shown in Fig. 4.6. The presence of discrete levels in the scattering region causes sharp peaks to appear in the conductance before the usual edge situated at $E \simeq V_0$. This is an example of *resonant tunneling* [43]: only electrons with specific energies (corresponding to resonances) are allowed to transfer through the double barrier without being reflected.

We calculated the current, as a function of the applied bias, for the one dimensional double potential barrier. We arbitrarly set an equilibrium Fermi level equal to $\mu = 0.23$a.u., which is lower than the resonance energy[a], $E_r = 0.32$ a.u. The bias voltage is applied symmetrically across the device. The calculation is done by evaluating the integral of Eq. (4.11), where the integration is computed for each value of the applied bias. With zero bias, we assign the same value to the Fermi levels on the left and right leads (μ_L, μ_R). The procedure is thus the following: we set a bias value V and compute the Green's functions for the resulting potential, calculate the conductance (Eq. (4.10)) which is thus integrated from μ_R to $\mu_L = \mu_R + V$. Thus, we obtain the current for a given bias V. In Figs. 4.8 we show the potentials resulting under the application of different bias, the respective DOS and the conductance, while in Fig. 4.7 we show the current versus bias, for a double barrier potential with one resonant state. It is clear that when the resonance remains outside the bias window ($\mu_R \leq E \leq \mu_L$) there are no states in the interface which support charge transport (panel a) of Fig. 4.8), thus the current is zero. The current remains nearly equal to zero until a bias of about $0.19Ha$ is applied. As shown in panel b), μ_L aligns with the resonant state and a large resonant current takes place. Here the current reaches its maximum value, since the electronic states

[a]Note that the resonance energy grows as the bias increases.

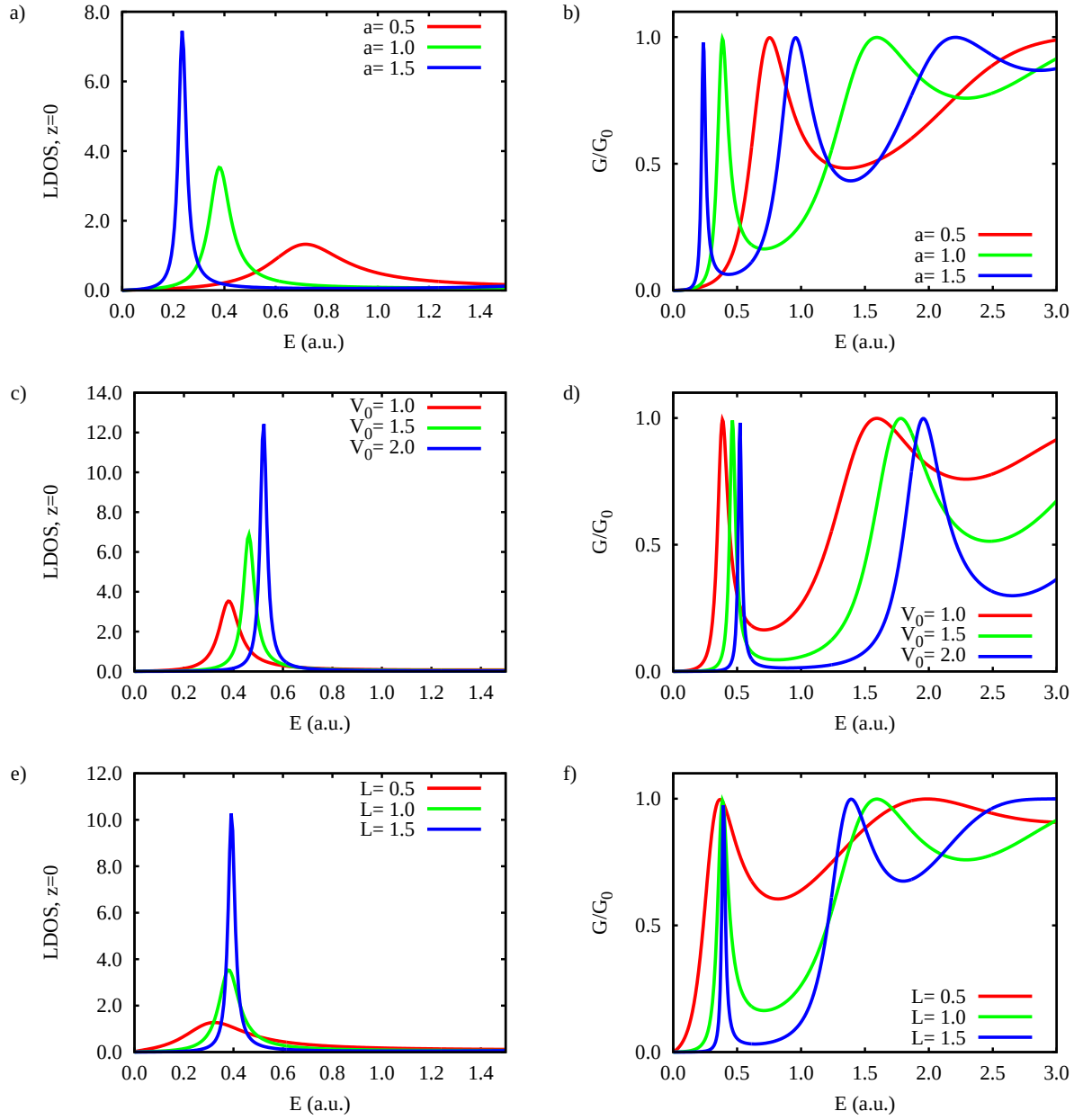

Figure 4.5: LDOS in $z = 0$ and conductance for several configurations of double square potential (default values: $L = 1$, $V_0 = 1Ha$, $a = 1a_0$, $\eta = 10^{-4}$). The parameters in the captions are intended in a.u.

that transport current from the left lead lie at about the resonant state inside the juction and therefore they have a larger probability to overcome the barriers. When the bias increases (panel c) the current reduces because the states that transmit are progressively far from resonance. The current persists until the resonant state is pushed below the occupied states in the left lead. Then, for a bias larger than 1.2 a.u. (panel d), the left band edge overcomes

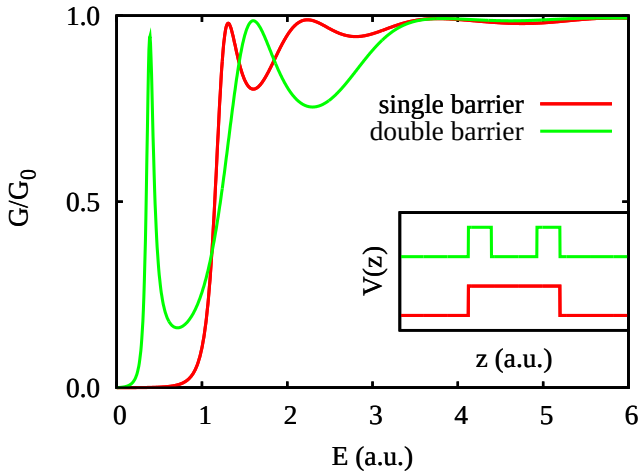

Figure 4.6: Conductance for single and double potential barriers.

the energy of the right barrier, and the current slowly increases again.
It is interesting to note that the energy integral of the resonant state is fairly independent of V, while this state is broader when it better hybridize with the right electrode.

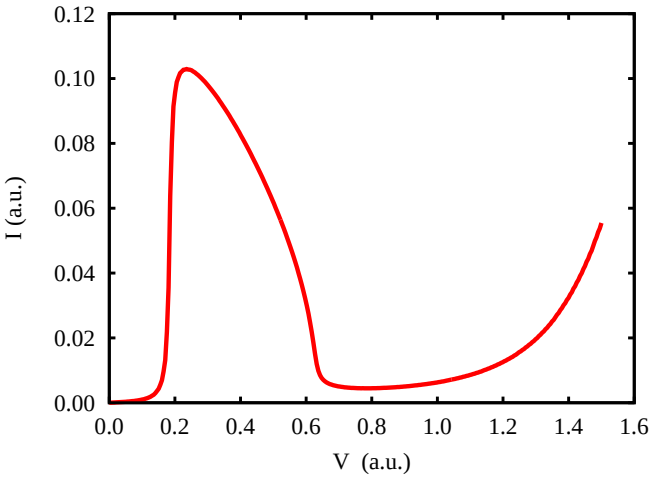

Figure 4.7: Current versus applied bias for a double barrier potential.

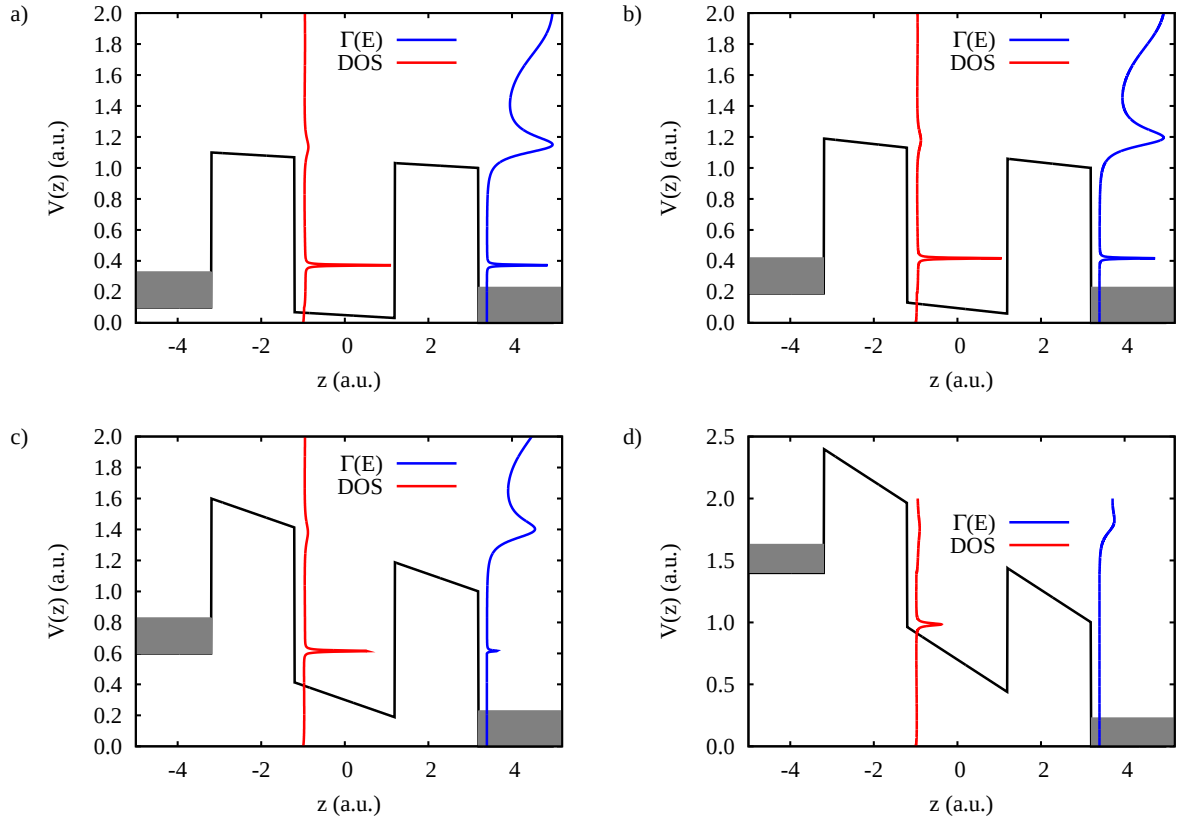

Figure 4.8: Potential (black), DOS (red) and conductance (bue) for different applied biases: $\Delta V = 0.1$, 0.19, 0.6, and 1.4 Ha. The filled areas at the left and right represent the electron filling of the left and right electrodes up to the chemical potentials.

4.3 Modulated potential

We apply the approach described above for the case of junction formed by Cu electrodes. We study the properties of these systems as we change the Cu surface exposed in the junction: we consider jellium Cu, Cu(111) and Cu(100). In order to reproduce the metal properties, we use a modulated potential in the direction normal to the surfaces, as developed by E.V. Chulkov and coworkers [44], which is able to reproduce the surface potential of a variety of metals. We add a gaussian well contribution in between two of these potentials, in order to obtain tunable ad hoc resonant states in the interface section (see Fig. 4.9). In the following, results are shown for three fixed values of the gaussian depth V_0, which give shallow, medium, and deep resonances. Namely, those values are 2.7 eV, 10.8 eV and 21.7 eV. In Fig. 4.11 we show the DOS of the clean surface (panels a-b), the DOS in the interface region (panels c-d), the conductance (panels e-f) and the I/V characteristic (panels g-h) for Cu(111) and Cu(100) on the left and right, respectively. These quantities are shown only considering $k_{\|} = 0$. In the case of Cu(111) and Cu(100) the modulation of the potential creates a band structure

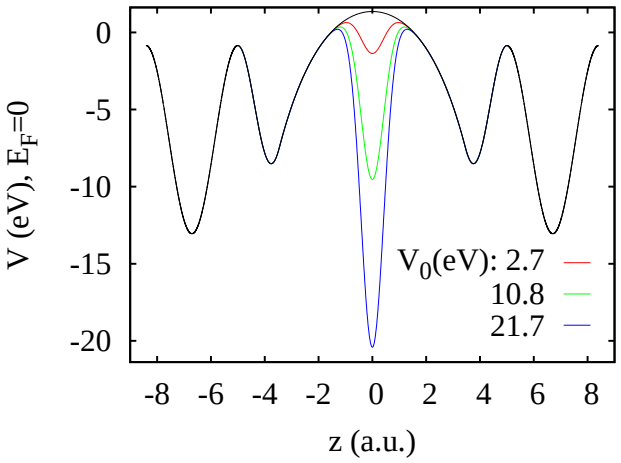

Figure 4.9: Example of potential at the interface of two Cu(111) surfaces with the addition of potential wells of three different depths.

and eventually surface states: for the former, the surface state lies inside the band gap (Fig. 4.11,a), while for the latter it lies on the edge of the lower ($k_{\|} = 0$) band (Fig. 4.11,b). We report the DOS for the interfaces (Fig. 4.11,c-d). Note that, when an interface is formed between two surfaces, the surface state splits into two states with opposite parity. The even state hybridizes with the ad-hoc resonant one in the gaussian well, determining two states which are the symmetric and antisymmetric combinations of the resonant and surface states. One of these states is pushed inside the lower band when the resonant state energy is deep in the well. The other state does not change its position as the well depth is changed, because of its odd parity. We calculate the Landauer conductance for normal incident (*i.e.* for $k_{\|} = 0$) electrons (Fig. 4.11,e-f). In the energy gap the conductance is zero, because no propagating states are available at those energies in the leads. We have instead large contributions at the resonance positions that are split into the electronic valence bands. Of course we can directly relate the feature of the conductance to those of the DOS. In order to calculate the current, we need to compute the conductance at different increasing biases. In Fig. 4.10 we show the DOS and the conductance G in the case of Cu(100) at different applied voltages ΔV. If we look at the DOS, we notice that its contribution due to the left electrode shifts in energy according to ΔV. The resonant state localized in the gaussian well is also shifted. The conductance behaves in the same way: its contribution in the bias window decreases as a consequence of the progressively lower overlap between the portions of the left/right electrode bands within the bias window. Eventually it will increase at sufficiently higher biases as a consequence of the overlap between the left electrode's valence band with the right one higher band. The resonant state doesn't contribute to the conductance since it is localized within a gap energy region. We compare the currents for the two interfaces (Fig. 4.11,g-h). The Cu(111) interface is an insulator at $k_{\|} = 0$. Therefore the current is zero until the bias is large enough to permit the left lower band overlap with the right higher one. The I/V shape

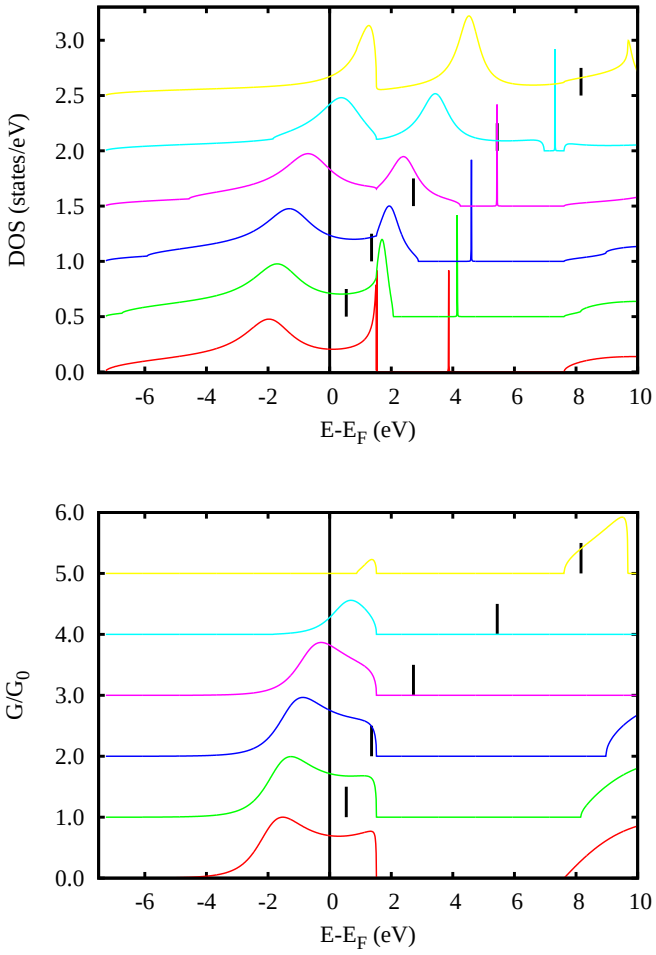

Figure 4.10: DOS (upper panel) and conductance (lower panel) for Cu(100) interface calculated at different voltages (V_0 = 10.8 eV). The black vertical lines represent the voltage applied to the junction.

differs significantly when the junction resonant level is shifted in energy. For these structures, the current at low biases can be enhanced by selecting the value of V_0 for which the resonance is aligned with the Fermi level. If we consider Cu(100), we can see that the highest current is found for $V_0 = 2.7$ eV, since the resonance is localized near E_F.
In conclusion, this simplified model is a tool to play with the relevant quantities which are basic in the transport properties of nanostructured interfaces.

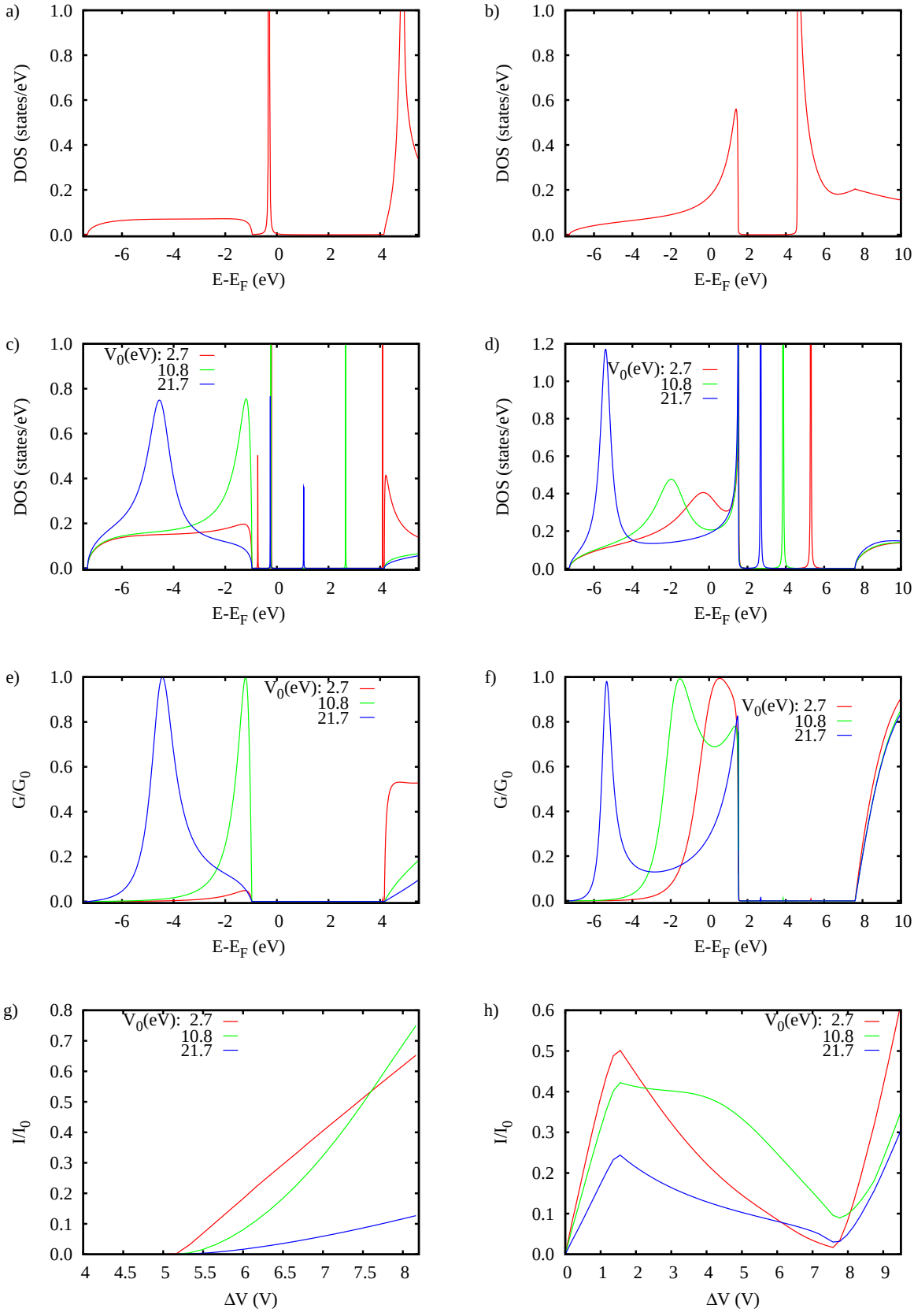

Figure 4.11: From top panel to lower panel: surface, DOS of the interface region, conductance and I/V charachteristic for Cu(111) (left) and Cu(100) (right). Note that the energy scales are referred to the Fermi level.

Chapter 5

Transport on 2D systems

Organic electronics has rapidly grown into a fundamental field whose potential is still to be fully developed and exploited. Research focuses on novel functional organic materials and existing applications already comprise, among others, nanoscale electronic devices such as thin film transistors and diodes, solar cells, integrated circuits on flexible substrates, carbon nanotube field effect transistors and molecular switches.

Graphene, a perfect carbon monolayer sp^2-hybridized, has attracted a huge interest since its discovery in 2004 [45, 46]. Besides a pure theoretical interest, its possible applications in carbon-based electronics represent a very exciting perspective. Graphene displays a very peculiar electronic structure, determined by the confinement of electrons in two dimensions and its geometrical symmetries. Being a zero gap semiconductor, its specific linear electronic band dispersion near the Brillouin zone corners (Dirac points) makes the electrons and holes to propagate as massless fermions [47, 48, 49, 50]. Therefore, graphene is a very good candidate to build transparent conducting electrodes to be incorporated in potential electronic and optoelectronic devices. Several studies have proven the potential of graphene to replace traditional electrode materials (such as tin-indium oxide) in electrical devices [51]. Being the incorporation of graphene in electronic circuits a feasible solution, the next logical step is to pattern graphene in order to obtain miniaturized circuits which mimic the behaviour of standard electronic components (gates, switches, diodes, sensors, etc.). For instance, one can think of a way to link different graphene electrodes. A possible and straightforward solution is to use carbon derived systems like graphene nanoribbon which preserve the nature of electrodes. Another way is to use components which are activated by an external stimulus, which can be mechanical, electrical or optical.

In this chapter, we first devote a Section to show the main properties of graphene and graphene nanoribbons based on DFT calculations. In the following two sections we will discuss two different graphene-based molecular junction which address the issues discussed so far. We first investigate a hybrid graphene junction, where the linkers between graphene electrodes are small stripes of carbon atoms. Our interest is to do a systematic investigation of how the basic geometrical features affect the transport properties of these heterojunctions.

Next, the second system under study is a photocromic molecular junction, composed of a particular class of molecules, named diarylethenes, which are embedded between graphene electrodes. The latter two sections will be opened by a discussion of the experimental and theoretical state-of-the art in the field, and the main motivations that drove us carry on these investigations.

5.1 Pristine graphene and GNR

5.1.1 Graphene

Graphene is the ideal 2D allotropic form of carbon where the atoms are periodically arranged in an infinite honeycomb network. Such an atomic structure is characterized by two kinds of bonds and exhibits the so-called planar sp^2 hybridization. Indeed, among the four valence orbitals of the carbon atom ($2s$, $2p_x$, $2p_y$ and $2p_z$ orbitals, where $\hat{z}$ is perpendicular to the graphene sheet), the (s, p_x, p_y) orbitals combine to form the inplane σ (bonding or occupied) and σ^* (anti-bonding or unoccupied) orbitals. Such orbitals are strong covalent bonds responsible for most of the binding energy. The remaining p_z orbital, pointing out of the graphene sheet, is odd with respect to the planar symmetry and cannot couple with the σ states, which are instead even. The lateral interaction among neighboring p_z orbitals creates the delocalized π (bonding) and π^* (anti-bonding) orbitals. If different layers of graphene are coherently stacked, the π orbitals are responsible of a weak inter-planar interaction and graphite is formed.

The graphene plane is an hexagonal lattice with two atoms per unit cell (A and B) and a

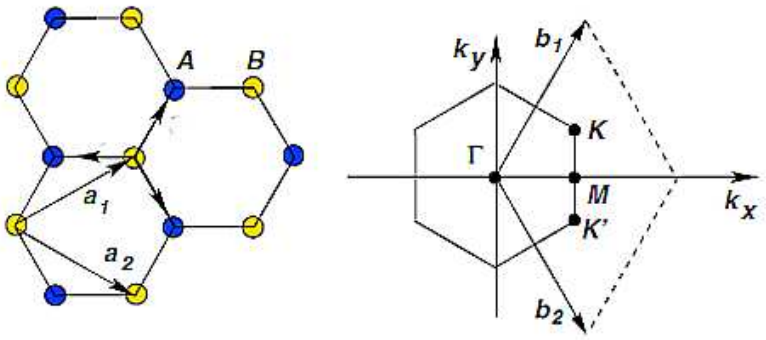

Figure 5.1: Graphene: basis vectors and Brillouin zone.

basis defined by the vectors ($\vec{a}_1$ and $\vec{a}_2$):

$$\begin{aligned} |\vec{a}_1| = |\vec{a}_2| &= \sqrt{3}a_{\mathrm{CC}} \\ \vec{a}_1 &= \sqrt{3}a_{\mathrm{CC}}\left(\frac{\sqrt{3}}{2}, \frac{1}{2}\right) \\ \vec{a}_2 &= \sqrt{3}a_{\mathrm{CC}}\left(\frac{\sqrt{3}}{2}, -\frac{1}{2}\right) \quad , \end{aligned} \tag{5.1}$$

where a_{CC} is the distance between two neighboring carbon atoms.
We performed DFT electronic structure calculations of pristine graphene using the SIESTA code [29, 30]. The exchange-correlation energy and electron−ion interaction are described by the Perdew-Burke-Ernzerhof (PBE) [52] generalized gradient approximation (GGA) and norm-conserving pseudopotentials [32] in the fully nonlocal form, respectively. A double-ζ polarized (DZP) basis set of numerical atomic orbitals is used and the energy cutoff for real-space mesh is set to 300 Ry [29] after convergence tests. We verified that a 40×40 **k**-mesh (821 points) is enough to obtain convergent results. The basis set for C includes DZP $2s$ and $2p$ orbitals, and we fix the radii of the orbitals by imposing an energy shift of 0.02 Ry. The resulting cutoff radii of the different species are then $r_{2s} = 4.08$ Bohr and $r_{2p} = 4.87$ Bohr. The unit cell is composed by two atoms, while periodic boundary conditions are used and the periodic replica of the graphene planes are separated by 11 Å in order to avoid direct coupling. In Fig. 5.2 we show how the energy changes with the lattice parameter: we obtained a converged value of a_{CC}=2.48 Å in good agreement with the experimental one a_{CC}^{exp}=2.46 Å. The calculated electronic bands are reported on Fig. 5.3 (left panel) along high symmetry points $M - \Gamma - K - M$. The typical feature of graphene is the crossing of the π and π^* bands at the K points, i.e. at all the vertices of the hexagonal Brillouin zone. In the neighbourhood of these special points the energy-momentum dispersion is quasi-linear (giving rise to the so-called Dirac cones), and electrons actually can be described as massless Dirac fermions. Consequently, graphene exhibits electronic properties that are distinctive for a 2D gas of particles described by the relativistic Dirac equation rather than the non-relativistic Schrödinger equation (only valid for non-relativistic electrons with a finite mass). Indeed, in graphene, charge carriers mimic relativistic particles with zero mass and an effective speed of light $c \simeq 10^6$m/s.
In the inset, we show the transmission function of pristine graphene in a shorter range near the Fermi level E_{F}, calculated along the armchair direction. We obtain the same result along the zigzag direction. As expected for perfect systems, the transmission function reflects the DOS and tends linearly to zero approaching E_{F}.

5.1.2 Graphene Nanoribbons

Graphene nanoribbons (GNR) are strips of graphene with a finite width that can be obtained by patterning graphene along preferential directions. Due to the honeycomb structure

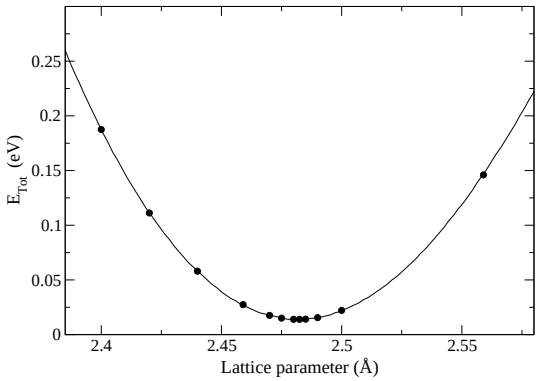

Figure 5.2: Graphene: total energy versus lattice parameter.

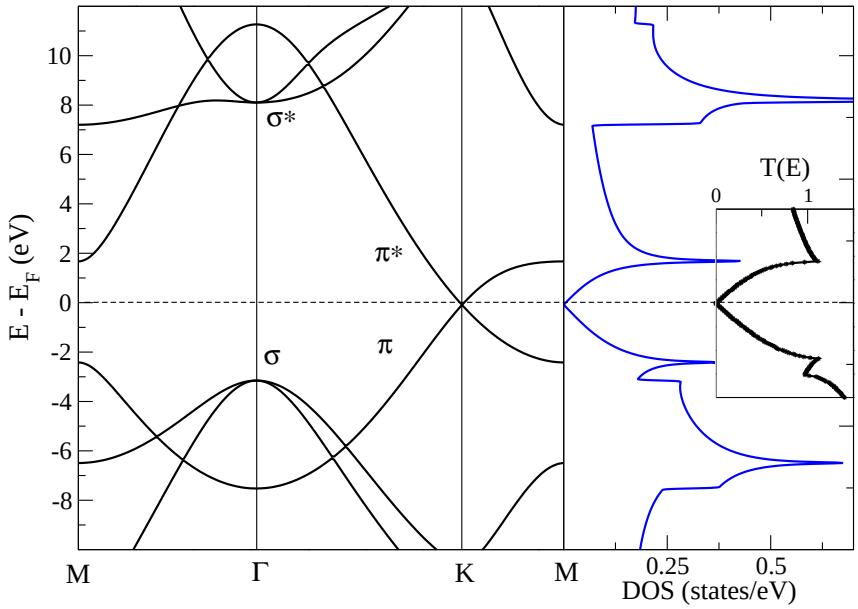

Figure 5.3: Graphene: electronic bands (left panel) and DOS (right panel). The bonding and antibonding π and σ bands are indicated. In the inset the transmission function of pristine graphene is shown.

of graphene, only two preferential directions can be considered: the resulting GNR have armchair or zigzag edges. In Fig. 5.4 such structures are illustrated, along with the usual convention for their nomenclature. N-aGNR (N-zGNR) are defined as the ribbon having N zigzag dimers (lines) along the transverse direction. If not otherwise stated, the dangling bonds on the edge sites of GNR will be assumed to be terminated by hydrogen atoms. The presence of edges in GNR entails the quantum mechanical constriction of electronic wave-

functions in the direction perpendicular to the axis of the ribbon and, as a consequence, a confinement-induced gap can open. This lateral confinement causes a discretization of the electronic quantum levels and breaks the spectrum into subbands. The Brillouin zone foldes to a rectangular zone, inscribed in the original Brillouin zone of graphene.
In Fig. 5.5 we show the electronic band structure and transmission function of 10-aGNR [a], taken as a reference system. In these two cases, an energy gap opens at E_F. It has been demonstrated that the aGNR electronic properties sensibly vary by changing the width of the ribbon [53, 54, 55, 56]. In particular, the width and the electron energy gap Δ_N are inversely proportional. Moreover, the electronic gap Δ_N (and thus the transport properties) of N-aGNR strongly depend on the value of N defining three different categories of aGNR: $\Delta_{3p+1} > \Delta_{3p} > \Delta_{3p-1}$, with p integer [56] . If we restrict to each of these classes, the energy gap decreases as p increases. The origin of the gap can be understood by considering the confinement imposed by the boundary conditions at ribbon edges, plus the perturbation induced by the presence of passivated edges (which can not be taken into account with simple tight-binding models). Also, this is a good test system to interpret the Landauer theory. Looking at the transmission function, we can notice that it increases by integer steps in corrispondence to each subband, i.e. to each channel that is open at a given energy.
The case of zGNR is a little more complicated. In fact, their ground state is predicted to be magnetic, with magnetic moments on the two edges. We calculated the electronic properties for the cases of ferromagnetic (FM) and anti-ferromagnetic (AF) structures of a reference zGNR, namely the 4-zGNR (Fig. 5.6). The energy difference between these two electronic configurations is $\sim$0.3 eV: the AF is more stable, because of the interaction between spins on opposite edges in the FM. The energy difference between AF and FM decreases as N increases due to progressive lower coupling between the edges. From the spin-resolved band structure, we see that the AF configuration conserve the semiconducting behaviour of aGNR with a 0.5 eV gap around E_F. On the contrary, the FM system is metallic as both the $\uparrow$ and $\downarrow$ bands cross the Fermi level.

[a] Details of the computations presented in Sect. 5.1.2

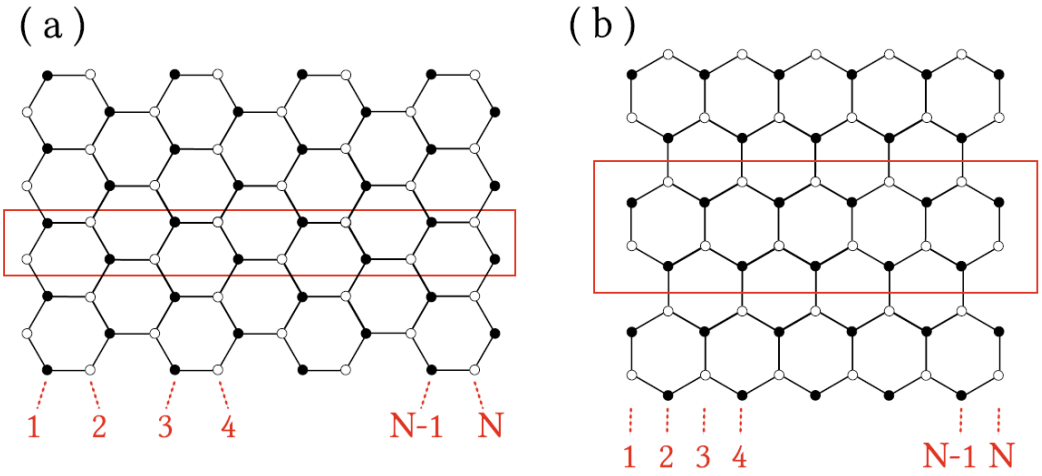

Figure 5.4: Carbon N-zGNR (a) and N-aGNR (b) composed of N armchair and zigzag lines, respectively. Black and white dots identify carbon atoms belonging to the two different graphene sublattices (A and B). The red rectangle represents the 1D unit cell of the corresponding GNR [48]

.

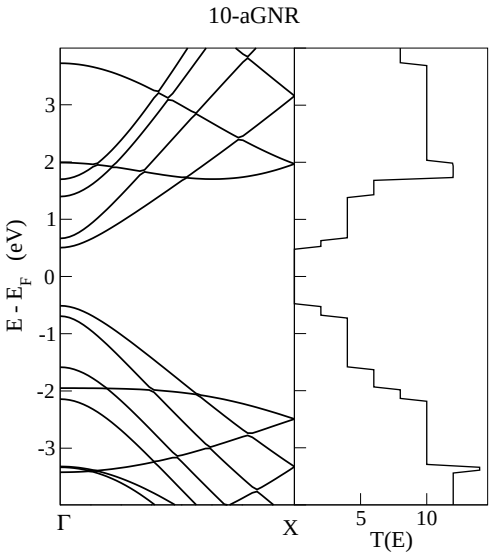

Figure 5.5: Electronic band structure and transmission function of 10-aGNR.

5.2 Graphene-GNR heterojunctions

5.2.1 Experiments and motivation

As discussed above, GNR are one dimensional graphene strips that are considered as promising candidate building blocks for future electronic applications [57, 58, 59]. Several methods

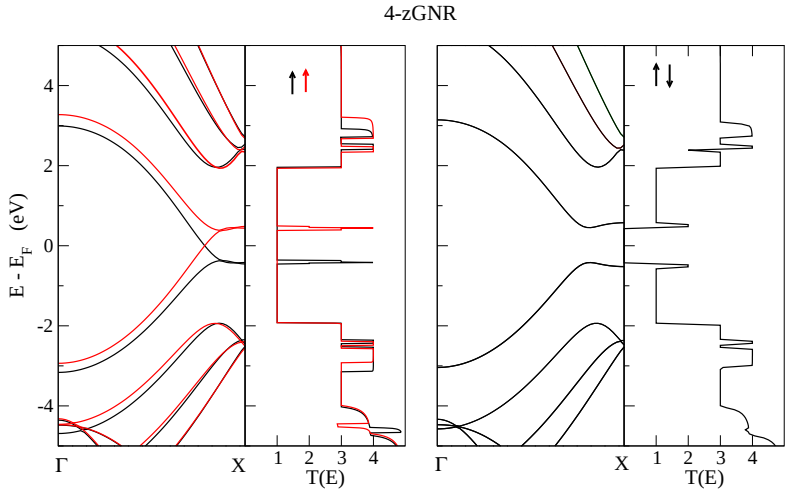

Figure 5.6: Electronic band structure and DOS for 4-zGNR in ferromagnetic (left) and antiferromagnetic (right) electronic configurations.

allow the production of GNR, including mechanical cutting of exfoliated graphene [46], patterning of epitaxially grown graphene [60], bottom-up chemical methods [61], and carbon nanotubes unzipping [62]. The finite size of the GNR gives rise to a large variety of electronic behaviors that can be relevant in transport. Transport properties of pristine GNR have been studied both for the ideal [63, 64, 65] and defective [66, 67, 68] case. Electronic transport has also been studied, by a tight-binding approach, for junctions connecting zGNR of different widths [69, 70, 71] revealing the crucial role played by corner edge structures [72]. A challenging technological issue would be to exploit the high mobility properties of graphene and the finite-size characteristics of GNR, by creating heterostructures which make use of both these properties. These systems may be used as interconnections to transmit signals in future pure-C-based electronic devices. In fact, the effects of quantum confinement in graphene nanoconstrictions have been studied showing their analogy with optics phenomena [73] as well as their exploitation for valley filter applications [74]. Recently a quantized ballistic conductance has been measured in such structures [75]. Although a chemical precise production of small nanoribbons and graphene nanojunctions is a significant challenge, a lot of progress has been made in recent years by means of different techniques. While a bottom-up approach has been proposed to build atomically precise GNR [61], graphene nanojunctions stable at room temperature can be produced by forming nanogaps in graphene by controlled electroburning [76]. Furthermore, the chirality of GNR edges can be selectively controlled by optical annealing enabling the realization of GNR and heterostructures with purified edges [77]. Even more complex junctions have been experimentally built, with carbon nanotubes as interconnections between graphene bilayers [78]. However, due to their flat structure, GNR seem easier to pattern than carbon nanotubes. Owing to the large zoology of hybrid graphene interconnections it is of great importance to perform a systematic investiga-

tion of their transport properties at the simplest level of configurational complexity, in order to clarify how the basic geometrical parameters affect the conductance. Most of the previous works investigating GNR junctions and graphene nanoconstrictions rely on standard tight-binding calculations. It has been shown by Louie and co-workers [56] that the predictions of simple tight-binding models on GNR may lead to incorrect band structures and energy gaps since the bonding characteristics between atoms substantially change at the edges. An *ab initio* study of GNR junctions avoids such these difficulties, providing an accurate description of their transport properties [79], which are directly related to the underlying electronic band structure.

In this Section, we present a first-principles study, by means of the non-equilibrium Green's functions (NEGF) technique described in previous chapters, of the electronic and transport properties of systems consisting of two semi-infinite graphene layers interconnected by an hydrogen-passivated armchair graphene nanoribbon. The transport properties of such junctions are predicted to strongly depend on the GNR geometry, while are quite robust to changes of the graphene's edges geometry. These structures combine the high mobility of graphene electrodes [80, 81, 82] with the intrinsic semiconducting behavior of GNR. We show that these semiconducting hybrid graphene-GNR junctions have a significant gap in the transmission spectrum, which may be exploited to build logic devices which require a large on-off ratio in the current [78].

In the following, we show the properties of aGNR junctions considering one representative for each class according to their width: we will take into account 3-aGNR, 5-aGNR, and 7-aGNR. In the case of 3-aGNR, we will consider ribbons of three different lengths, namely those consisting of four (4L), six (6L), and eight (8L) zigzag lines along their axis. The 8L 3-aGNR will be considered as an illustrative model to study the effects of the application of a bias. We will discuss the effect of the rotation of a phenyl ring, and show how different edge configurations affect the transport properties.

5.2.2 Model and methods

The system setup for a 4L 7-aGNR junction is shown in Fig. 5.7 as a representative case. This open system is constituted by three parts: the left (L) and right (R) semi-infinite graphene leads, and an extended-molecule (EM) region. The junction is constructed so that the periodic replicas of the aGNR along the direction parallel to the electrode edge are separated by 7.43 Å. This corresponds to three unit cells of graphene and we verified that the interactions among the replica are negligible. The width of the leads part included inside the EM region is chosen after converging the transmission function: six carbon zigzag lines per side are sufficient to reach stable results.

The electronic structure calculations are carried out using the first-principles self-consistent method implemented in SIESTA package [29, 30]. The exchange-correlation energy and electron−ion interaction are described by the Perdew-Burke-Ernzerhof (PBE) [52] generalized gradient approximation (GGA) and norm-conserving pseudopotentials[83] in the fully

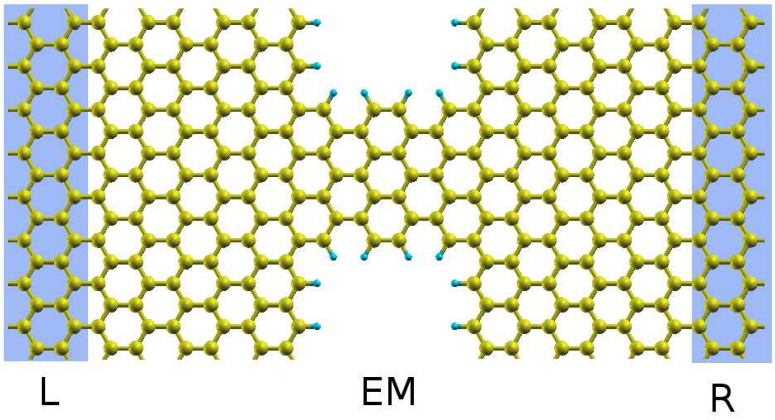

Figure 5.7: System setup for 4L 7-aGNR. The left and right electrodes and the extended-molecule region are highlighted.

nonlocal form, respectively. A double-ζ polarized basis set of numerical atomic orbitals is used and the energy cutoff for real-space mesh is set to 200 Ry [29]. Preliminary tests indicated that the relaxation of the carbon atoms in the leads did not affect the transport properties of the systems under study, so in most cases we considered non-relaxed geometries. The edges of semi-infinite leads are saturated with one relaxed hydrogen per carbon atom. We also verified that the relaxation of the aGNR does not affect significantly the electronic and transport properties of the system. For the calculation of the transmission coefficients, 60 k-points along the transverse direction in the 2D first Brillouin zone are used. Periodic images of the graphene layer are separated by 15 Å along the normal direction. The electronic transport is studied with the TranSIESTA code.

5.2.3 Results

We first investigate in detail the electronic properties and the transmission function of the 4L 3-aGNR junction [84]. For the other systems, similar considerations can be done. In Fig. 5.8 we show the density of states (DOS) in the EM region and the projected density of states (PDOS) on the ribbon region, in comparison with the transmission function. Around the Fermi energy (E_{F}), the DOS resembles that of graphene, in fact it goes to zero almost linearly with a deviation due to the presence of vacuum portions in the molecular bridge region. The signature of the molecular energy levels is clear both in the DOS and PDOS, and the transmission function has higher intensity in correspondence to those peaks. We also consider the isolated molecule obtained by cutting the bonds between the 4L 3-aGNR and the graphene leads, and saturating them with hydrogen atoms. The red triangles represent the eigenvalues of the isolated molecule, which correlate well with the position of the resonances in the DOS, PDOS, and transmission. The (P)DOS for the other studied systems have a similar behavior, and are not reported here.

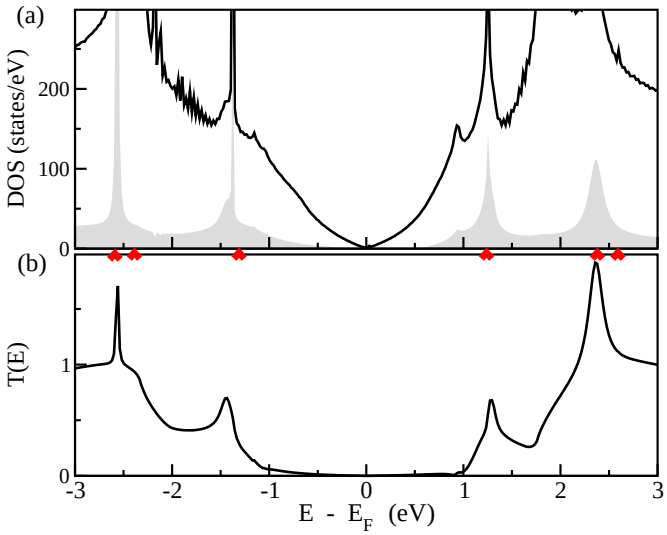

Figure 5.8: Electronic and transport properties of 4L 3-aGNR. Upper panel (a): DOS (solid line) of the junction and PDOS (shaded grey area) on the ribbon region. Red triangles represent the eigenstates of the isolated (unconnected and hydrogenated) 4L 3-aGNR linker. Lower panel (b): transmission function.

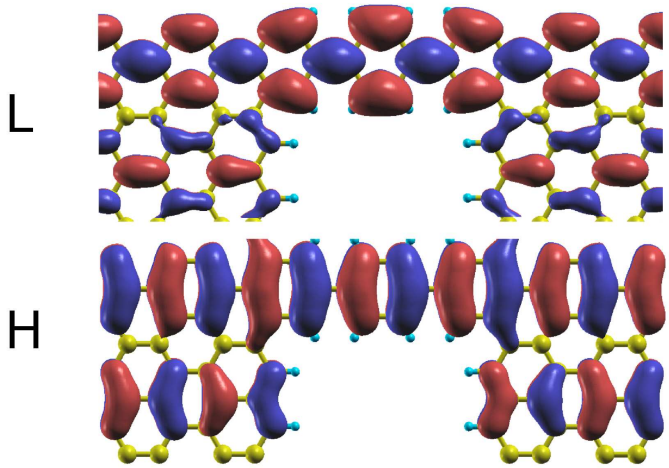

Figure 5.9: 4L 3-aGNR junction: isosurface plot of the wavefunctions at energies corresponding to the LUMO and HOMO resonant transmission peaks, calculated at $k_{\|} = 0$.

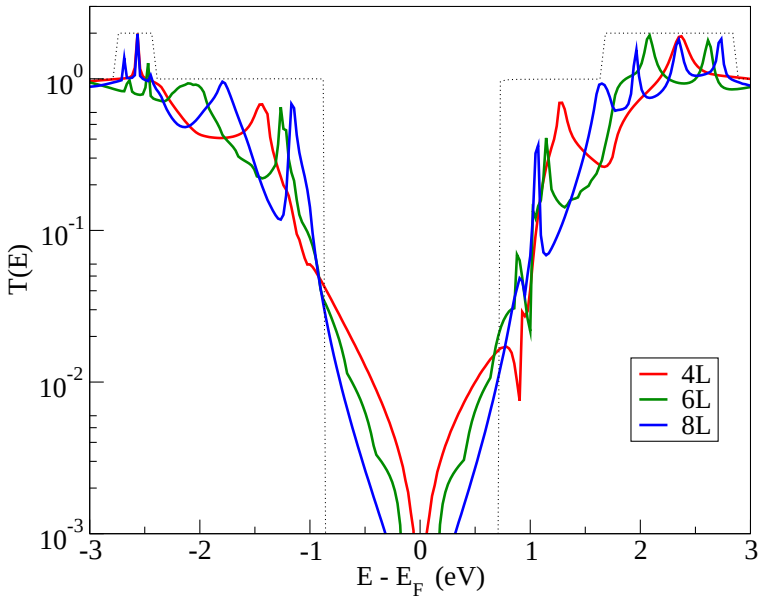

Figure 5.10: Transmission function of 3-aGNR junctions for three different lengths: 4L (red), 6L (green), and 8L (blue). The dotted line is the transmission function of the pristine infinite 3-aGNR.

Moving away from E_F, the transmission function increses up to significant values in correspondence to the two peaks at -1.4 and 1.3 eV; these peaks are generated by the hybridization of the molecule's highest occupied molecular orbital (HOMO) and the lowest unoccupied molecular orbital (LUMO) states with the leads, playing the role of channels between the two graphene electrodes. The corresponding wavefunctions of the interacting system (shown in Fig. 5.9) calculated at $k_{\|} = 0$, have the same shape and symmetry of that of the isolated molecule (see Fig. 5.14). These wavefunctions represent good conducting states, as they are delocalized along the molecule and propagate inside the electrodes with the same symmetry. Some other states farther from E_F contribute to the transmission. All these states are generated from the π orbitals of the C atoms and they are delocalized along the junction.

Length dependence

We now discuss the dependence on the length of the ribbon forming the junction. The transmission functions for the 4L, 6L, and 8L 3-aGNR junctions, reported in Fig. 5.10, show some general trends. The peaks become denser when the length of the junction increases, because they are related to the discrete structure of the electronic states of the nanostructured ribbon. Thus, the effective gap of the junction decreases as the length increases. As expected, the transmission function of the pristine infinite 3-aGNR acts like an envelope curve for the

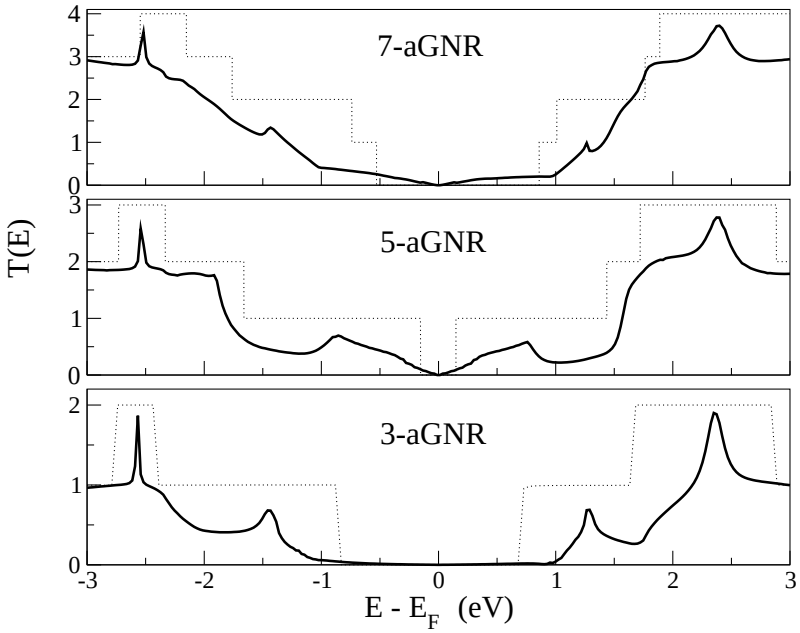

Figure 5.11: Transmission function of 4L N-aGNR junctions for $N = 3$, 5, and 7. Dotted line: transmission function of the infinite pristine N-aGNR.

other curves; it has an energy gap of $\simeq$1.5 eV [56]. This aspect confirms that the contacts between the graphene sheets and the nanoribbon do not represent significant barriers to the transport of electrons, as one can naively expect due to the chemical identity of the different subsystems. Within the energy gap of the nanoribbon, the transmission function is very low and decreases rapidly as the length of the ribbon increases. This behavior is clearly due to the tunneling mechanism dominating the transmission at those energies. The states of the graphene lead decay exponentially along the ribbon because there are no states in the junction supporting the conductance. This metal-semiconductor-metal device presents an effective gap for transport, since the conductance inside the gap is several orders of magnitude lower than that outside it [76].

Width dependence

In order to analyze the effects of the aGNR width, we consider a representative aGNR for each of the three classes, i.e. junctions made of 4L 3-aGNR, 4L 5-aGNR, and 4L 7-aGNR. As illustrated in Fig. 5.11, the aGNR junctions have different gaps in the transmission spectrum consistently with the previously reported results [56]. In miniaturized graphene-based electronic devices these structures may act both as linkers and as active components, and it would be useful to finely tune their width in order to have different conductive behaviors. Within each class, we expect the energy gap to decrease as the width of the junction increases. We notice that the intensity of the transmission function is higher for wider ribbons,

as more electronic channels are open. Moreover, as the width of the ribbon increases the spike features of the transmission function become less marked, since the system approaches the limit of graphene. In this case, the transmission functions of the pristine aGNR is a good reference only for those junctions where the aspect ratio between the length and the width is reasonably high. This because the contribution to the conductance of the infinite aGNR comes from $k_{\parallel} = 0$ only. For finite nanoribbons this restriction is relaxed and the passage of electrons with a finite $k_{\parallel}$ is allowed, with $k_{\parallel}$ within an interval that increases as the width to length ratio increases. This is clearly reflected in the transmission function, which departs from an exponential decay within the energy gap for short and wide ribbons. This is more evident for the 4L 7-aGNR in Fig. 5.11. For this ribbon the conductance is linear in the gap region, reflecting the underlying electronic structure of the graphene electrodes, and departing from a strictly tunneling behavior dominated by the energy dependence of the effective tunneling barrier.

Effects of applied bias

We now discuss the effects of the application of a bias to the junction. We consider the junction with the 8L 3-aGNR as a representative case; this is the longest junction considered here, thus being that in which the edges of the two graphene leads are less interacting. In Fig. 5.12 the transmission functions for different biases up to 1.0 V are shown. For any given bias voltage, the chemical potentials of the two leads are well recognizable, as they correspond to the left and right Dirac points where the DOS tends to zero. Within the bias window, the intensity of the transmission function increases with the bias. This is expected since it is determined by the number of electron tunneling through the leads, and the DOS of graphene shows a linear energy dependence in that region. Thus, the shape of the transmission function within the gap region can be interpreted in terms of the product of the DOS of the left an right graphene leads and a modulation function determined by the size of the gap of the nanoribbons. We notice two small peaks near the Dirac points of the two electrodes, which we assign to the edge states appearing at the two zigzag electrodes [85]. In fact, in presence of zigzag edges there is a band near E_{F} which corresponds to a state localized at the edge. At small applied bias, the probability for an electron lying in an edge state to be transferred to the opposite lead is very small since the DOS at that energy is negligible. However, at finite bias, the situation is different and we can find distinct features in the transmission curves related to the presence of edge states. We can also see that the resonances originated by the HOMO and LUMO of the aGNR slightly shift as the bias is applied. As a result, the energy gap reduces by approximatively 10% when a bias of 1.0 V is applied. In the lowest panel of Fig. 5.12 we report the current as a function of the applied bias, computed with Eq. (3.60). The data of the current are calculated in two ways. We present fully self-consistent results obtained using different transmission curves for different voltages (the corresponding transmission curves are also shown in Fig. 5.12). We also present the current obtained using the transmission curve calculated at zero bias. Both calculations show very

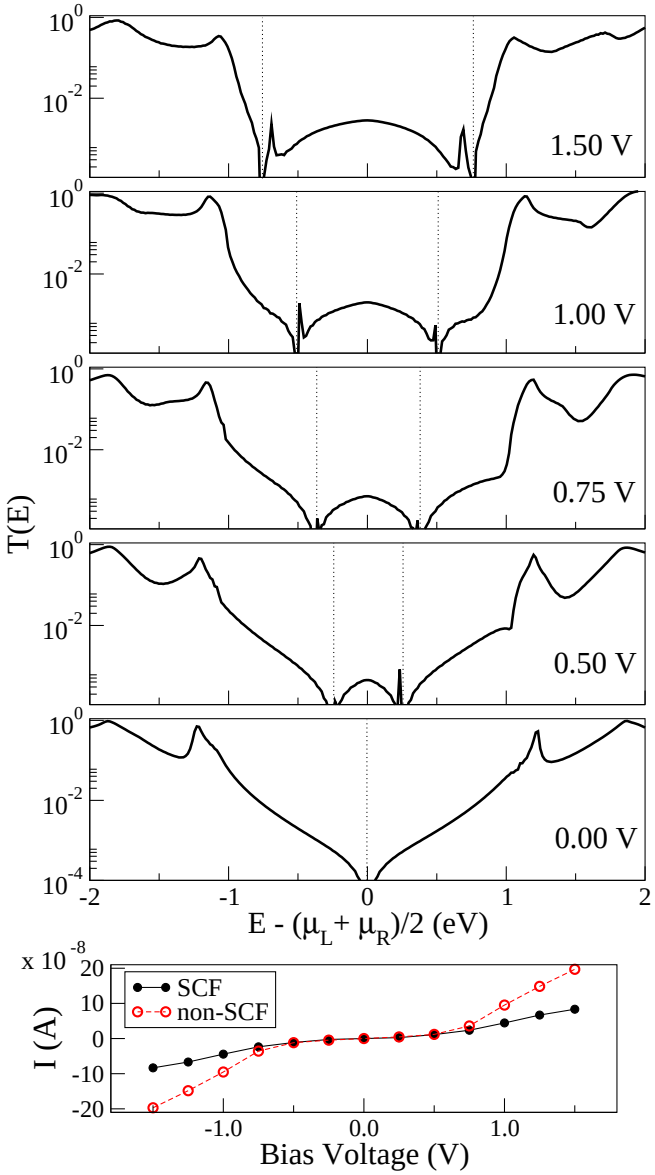

Figure 5.12: Upper panels: transmission function of 8L 3-aGNR junction for five selected values of the bias voltage, as indicated in labels. The bias window is delimited by two vertical lines. Lower panel: SCF (black) and non-SCF (red) current-voltage characteristics of 8L 3-aGNR junction.

similar behavior and reasonably agree in the order of magnitude of the calculated current. However, the non-self-consistent current clearly overestimates the value of the current as compared to the selfconsistent result. The current remains low (less that 0.1 μ), although it shows non-linear behavior with the onset of a sharp increase as we approach the position of the resonances of the junction. Unfortunately, for voltages above 1.5 V, the self-consistent process becomes very unstable and it was not possible to accurately converge results at higher

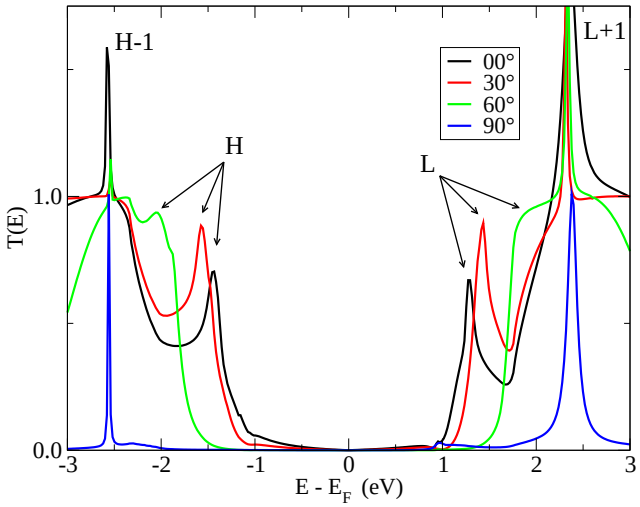

Figure 5.13: Transmission function at zero bias for the 4L 3-aGNR junction, under rigid torsion of the central phenyl ring. The curves shown here refer to rotations by $0°, 30°, 60°$, and $90°$. The main resonances are highlighted and the labels correspond to the 3-aGNR molecular states shown in Fig. 5.14.

voltages. However, we can explore the behavior of the currentvoltage characteristics with the non-self-consistent calculation and estimate the values of the current at higher voltages. The current sharply increases when the two main peaks enter the bias window, and for a bias of 3.0 V we estimate a current of 3.3 μ. Our calculated values of the current are consistent with recent measurements performed in graphene molecular junctions [76].

Torsion of the central phenyl ring

When considering junctions made of 3-aGNR, the system is actually a chain of phenyl rings. In this case, it has been shown that the stable configuration consists of neighboring rings lying on different planes [86, 87]. We can thus take into account one more degree of freedom, that is the relative torsion angle between the phenyl rings of the linkers. We show the effect of the ring rotation by taking the 4L 3-aGNR as test system. According to our calculations, the most stable configuration corresponds to a rotation of $\simeq 45°$ [88]. In fact, the central ring tends to rotate with respect to its planar configuration due to steric repulsion between its hydrogen atoms and those of the neighboring rings. By looking at the transmission function in Fig. 5.13 we note a general trend. As the ring rotates from $0°$ to $90°$, the peak H (HOMO) shifts towards lower energies, while the peak L (LUMO) shifts towards higher energies. As a result, the energy gap of the system increases. In fact, the wavefunctions related to these peaks (see Fig. 5.14) are extended along all the molecular backbone and they feel a distortion as the central ring is rotated, thus their energies are expected to change. Both HOMO and LUMO are even with respect to the mirror plane that bisects the 3-aGNR molecule. As a

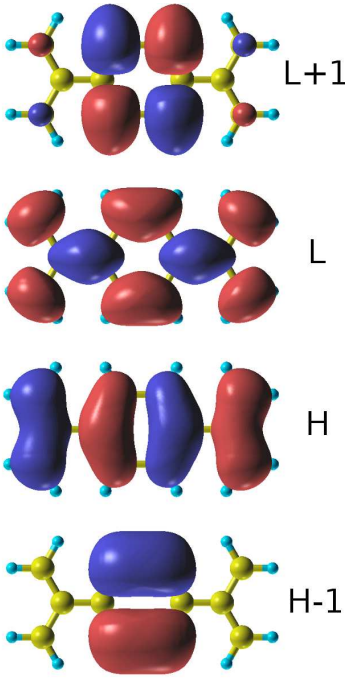

Figure 5.14: Isosurface plots of the selected molecular orbitals of the isolated 3-aGNR linker: HOMO (H), HOMO-1 (H-1), LUMO (L) and LUMO+1 (L+1).

consequence of this symmetry, when the rotation is by 90° these two peaks disappear: the linear combinations of the p_z orbitals of the central carbon atoms are orthogonal to those of the remaining carbon atoms, resulting in the closure of the corresponding conduction channels. The situation is different for the HOMO-1 and LUMO$+1$, whose wavefunctions are mainly localized on the central phenyl ring. In fact, they are at the same energy position regardless of the torsion angle. These considerations may be extended to the case of longer aGNR.

Passivation of the graphene edges

Concerning the passivation of the graphene edges, all the results presented so far refer to what we can call "standard saturation". That is, each edge carbon atom is passivated by a single hydrogen (panel *d* in Fig. 5.15). In a real system, subject to different hydrogen partial pressures, one may guess that the edge saturation may change [85]. In order to validate our results, we show the effect of four different edge passivations on the transmission function. The first case we consider is the formation of pentagon-heptagon reconstruction of the graphene edges, where no H atoms are present on the edge (panel *a*). Then, we considered the case in which each carbon edge atom is passivated by two hydrogens (panel *c*). One may also guess a more complicated connection between the aGNR and the leads, and we modeled it as shown in the inset of panel *b*. Figure 5.15 also shows the transmission function for these four cases. Our results are very robust with respect to these changes of the geometry and

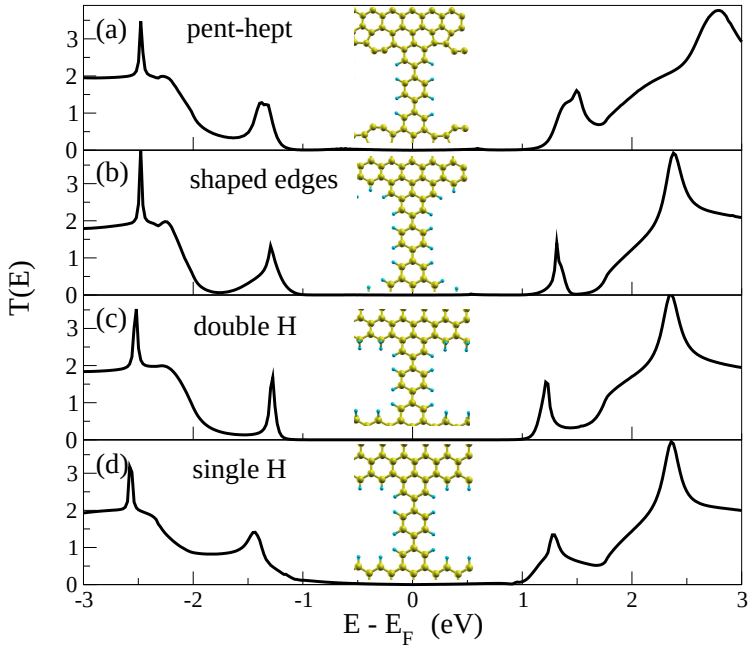

Figure 5.15: Zero bias transmission function of 4L 3-aGNR junctions with four different passivations of the graphene edges. The inset show the linking geometries.

passivation of the graphene lead edges, as we see only minor differences among these cases, mainly a sharpening of the peaks derived from the HOMO and LUMO resonances. This is evident in particular for the double H and shaped edges, in which the orbitals of the aGNR are less hybridized with the leads. The reason is that in both cases less charge is present on the graphene layer edge.

5.3 Graphene-diarylethene junctions

5.3.1 Diarylethene

Before showing the detailed results of this study, it is necessary to briefly introduce photochromism and what diarylethene molecules are. Photochromism is defined as the reversible change of color upon photoirradiation which is typical of certain molecules in gas, liquid or solid phase. Diarylethenes is a novel class of photochromic molecules which have been proved to be photochemically reversible and thermally irreversible [89, 90]. Most of diarylenthene derivatives exhibit light induced switching both in solution and as single crystals [89, 91, 92] by changing reversibly in aromaticity during the closed-open (open-closed) configuration transition, determined by visible and ultraviolet light, respectively [93]. In the upper panel of Fig. 5.16 the chemical structure of the diarylenthene molecule is shown. In the left-side open-ring isomer two thiophene rings present an open bond. On the other hand, in the right-side closed-ring isomer π-electrons are delocalized throughout the molecule and the HOMO$-$LUMO gap becomes small. More precisely, the photocyclization process (i.e. the process of transition from open to closed isomer) causes a transition from a cross-conjugated system to a fully conjugated one. In addition to the change in the electronic structure, a photocyclization induces a geometrical structural change. In the lower panel of Fig. 5.16 we show the relaxed molecule geometries that we calculated with DFT. While in the open isomer the two thiophene rings lie in two planes forming a dihedral angle of 40°, in the closed isomer it reduces to 5°. We also notice a 2% shrinking of the molecule length upon photocyclization. The electronic ground states of the two isomers are separated by a large potential barrier which prevents the cyclization at standard temperature conditions. It has been shown that the cyclization proceeds via excitation of an electron to one or more excited states, where the energy barriers become considerably lower. For a more detailed discussion of the photochromic reactions see Ref. [89]. In the same reference, it has been shown that diarylethene molecules fulfill some key requirements for photo-switching devices application:

- Thermal stability of both isomers
- Fatigue resistent properties
- High sensitivity
- Rapid response
- Reactivity in solid state.

These properties have motivated the investigation on diarylethene junctions with metal and semiconducting electrodes as we will discuss in the next Section.

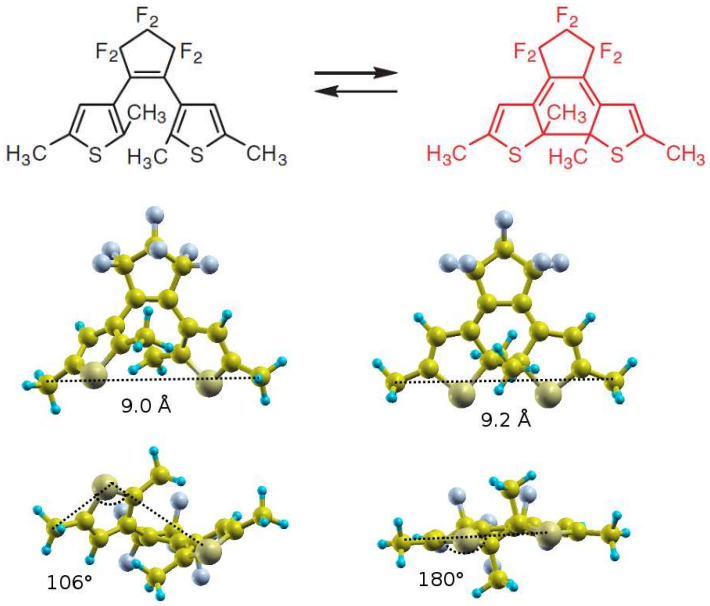

Figure 5.16: Open- and close-ring isomers of 1,2-bis(2,5-dimethyl-3-theinyl)perfluorocyclopentene: chemical structures (upper panel) and top-side view of the geometry relaxed with DFT (lower panel).

5.3.2 Experiments and motivation

The exciting properties of diarylenthenes raised much interest and stimulated research on diarylethene derivatives as suitable photochromic molecular switches [94, 95]. Investigations of diarylenthene junctions with gold electrodes showed that conductivity increases by two orders of magnitude in the closed isomer compared to that of the open one [96]. Nonetheless several diarylethene derivatives on gold leads only display photochromic switching from the closed to the open state after irradiation with visible light but not the reverse process by UV [97, 98] owing to the fast quenching of the photo-excited hole of the HOMO state of the open isomer into gold [99]. By connecting the metal anchoring sulfur atom by a phenyl group spacer reversible light-induced switching resulted both on Au(111) [100] and gold nanoparticles [101]. Photochromic diarylethene derivatives are also investigated on single walled carbon nanotube (SWCNT) as perspective single molecule devices with a more accurately defined contacts to the electrodes [102]. For such system it was found that switching from insulating to conducting, i.e. from open to closed molecular configuration occurs, but not the reverse, unlike in the case of Au [103]. The timely character of this topic is confirmed by the wealth of theoretical studies on the conductance of photochromic switches both with gold [90, 99, 104, 105, 106, 107, 108] and SWCNT electrodes [109].
In this Section, we investigate the conductance of a diaylethene switch sandwiched between two semiinfinite graphene electrodes [110]. As explained in Sect. 5.1, the two-dimensional

(2D) form of carbon has just revealed several intriguing fundamental properties and huge potential in nanoelectronics. In particular, high chemical stability, low resistivity and mechanical strength suggest graphene, a more cost-effective material than carbon nanotubes, as an alternative component for electrodes in electronic devices [111]. Furthermore in graphene electrons can travel ballistically up to a μm [112], and electron-phonon scattering intensity is very weak [113]. This implies a carrier mobility larger than that of the inorganic semiconductor with the largest mobility, i.e. InSb, and that of carbon nanotubes. If defects and impurities are eliminated, such mobility is about $2{\cdot}10^5$ cm^2/Vs [112], but in practice graphene sheets have irregular shapes and contain impurities and defects. To overcome this difficulty we point out a promising bottom up experimental technique capable to synthetize graphene starting from small corenene blocks and to build well defined molecule electrode contacts [114]. Transparent, conductive, and ultrathin graphene films, have been demonstrated to be alternative metal-oxide electrodes for solid-state dye-sensitized solar cells [115].

5.3.3 Model and Methods

We studied the open and closed structures of two different diarylethene molecules, shown in Fig. 5.17. The central dithienylethene part is the same for each molecule, and it is attached to the electrodes through $-$R$-$ with R=CH_2 (we call this A1) and R=CO$-$NH (referred to as A2). We also considered longer isomers, with two phenyl linkers connected in the same fashion, namely B1 and B2. We started with optimized structures of the molecules with the two R groups connected to H atoms. Then the two H atoms were removed and the molecules were embedded between two graphene sheets. The graphene electrodes were taken to have zig-zag edges with the valencies of the edge C atoms satisfied by H atoms. This structure was chosen because C atoms at zig-zag terminations display stronger affinity towards radicals, and hence form stronger bonds with H atoms. Graphene with zig-zag edges displays an edge state near the Fermi level [116].

First, we optimized the energy of the system by varying the electrode-electrode distance. We remark that in the optimized geometry, the plane of the molecule is approximately perpendicular to the plane of the two graphene sheets. This minimizes the coupling of π states of the molecule with those of graphene, which can be advantageous in certain cases. In fact, it would be interesting to tune the orientation of the molecular plane with respect to that of graphene, by linking the molecule to more than one carbon of the graphene. In this way, one could adjust the hybridization of the molecular levels by changing the relative orientation of the molecule with respect to the graphene plane. The system may thus be thought of comprising of three separate parts: the left and right semi-infinite graphene leads, and an extended-molecule region. For each electrode, six layers of carbon atoms are included in the extended molecule region in order to screen the perturbation from the central region. With this, the final geometry with the contacts is relaxed again. The graphene electrodes are constructed so that the periodic replicas of the contact region are separated by four unit cells (i.e. 7.436 Å), and the interaction among them is negligible. Our electronic

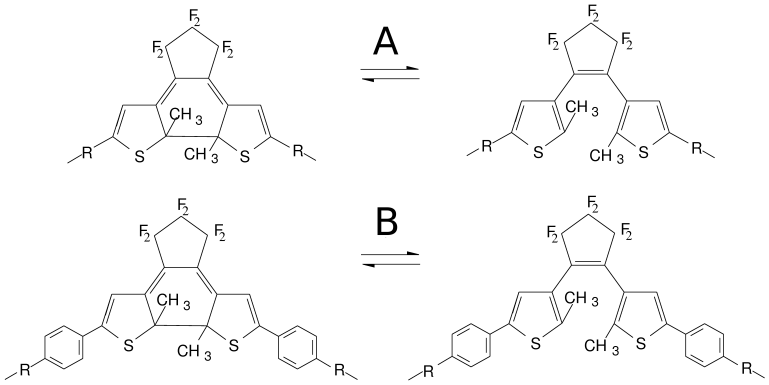

Figure 5.17: Structures of the closed and open forms of the two diarylethene derivatives studied in this work. Here, R is the functional group that links the molecule to graphene, which is $-CH_2-$ in the first case (A1 and B1) and $-CO-NH-$ (amide linking) in the second case (A2 and B2).

structure calculations are carried out using the DFT self-consistent pseudopotential method implemented in SIESTA package [117]. The exchange-correlation effect and electron-ion interaction is described by the Perdew-Burke-Ernzerhof generalized gradient approximation and the norm-conserving pseudopotential in the fully nonlocal form, respectively. A double-ζ plus polarization basis set is used to describe the localized atomic orbitals and an energy cutoff for real space mesh size is set to be 200 Ry. The ionic positions of carbon atoms are the ideal positions of a previously relaxed graphene sheet, while the hydrogen positions are relaxed for each junction. We performed all relaxations with a force tolerance of 0.04 eV/Å. For the self-consistent calculations, 12 K-points are used in the transversal direction (that of the electrode's edge), while for the calculations of the transmission function 60 K-points are taken into account. The vacuum portions between two neighboring layers are set to be 15 Å. The electronic and transport properties are similar for the four molecules shown in Fig. 5.17 and we choose to first discuss those of B1 in depth.

5.3.4 Results

In the upper panels of Fig. 5.18 we present the total DOS (solid line) of the extended system and the projected density of states (PDOS) (shaded area) onto the molecular region, as function of the electron energy, the left and the right one for the closed and open isomer, respectively. The transmission function dependence on the injected electron energy is shown in logarithmic scale in the lower panels of Fig. 5.18. The total DOS is reminescent of that of the electrodes, since near E_F it displays a linear dispersion following that of an ideal, infinite graphene sheet. Of course, very close to E_F the dispersion is not perfectly linear due to the vacuum region between two graphene sheets. Furthemore we remark the presence of two low peaks very near E_F, one slightly above and the other just below it. They are states mainly localized at the molecule-electrode interface whose origin stems from the zig-zag termination

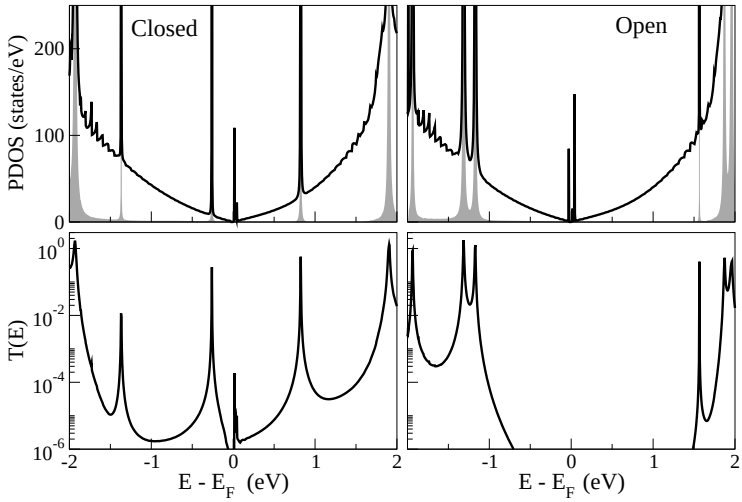

Figure 5.18: PDOS and transmission function for the closed (left) and open (right) isomers of B1 diarylethene. Upper panel: DOS (line) and PDOS (shaded area) on the molecular region. Lower panels: zero-bias transmission functions.

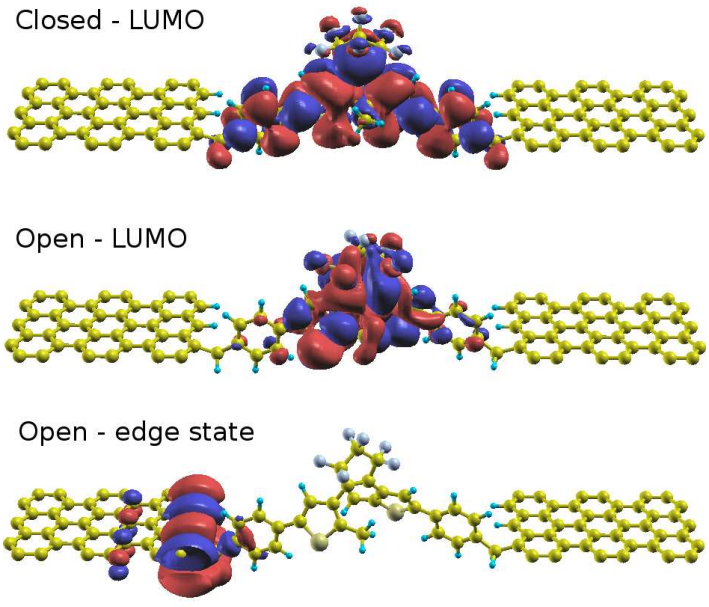

Figure 5.19: Real part of some representative wavefunctions of the junction with molecule B1: the LUMO of the closed isomer (upper panel), the LUMO of the open isomer (middle panel), and one edge state for the open isomer (lower panel).

edge states of the two graphene sheets interacting with the orbitals of the molecule in the coupled system. We point out that, as a consequence of the perturbation due to the junction, such states lie within the continuum graphene spectrum and they become resonant conducting states.Apart from the edge states, all peaks in the PDOS refer to molecular orbitals broadened by the interaction with the electrodes and a corresponding feature at the same energy appears in the transmission function. We concentrate on the two main peaks of conductance for each isomer that appear on the left and on the right side of E_{F}. They are due to the hybridization of the HOMO and LUMO states of the molecule with the graphene substrate. For the closed isomer such states are closer to E_{F}, and their intensity is lower, if compared with that of other molecular states, since the DOS of the underlying graphene sheets tends to zero as the energy approaches E_{F}. However, considering small enough energy deviations from E_{F}, the transmission function is always larger for the closed isomers than for the open ones. The lower conductance of the open isomers is due to their distorted geometry: the breaking of the central C−C bond due to the closed-open transition affects the π-conjugation of the structure reducing it [118]. Hence, the electrons are less delocalized along the molecular backbone reducing transmission. In Fig. 5.19 we display the real part of the wavefunction for three representative states of the system, namely the LUMO of the closed isomer, the LUMO of the open isomer, and one edge state of the open molecule. We observe that the former LUMO is more widely spread than the latter one, reflecting its more extended π conjugation. The plotted edge state shows a rapid decay inside the molecular region. The other edge state just mirrors it on the opposite side of the junction. The transmission functions for the A1, A2, B1, B2 diarylethene derivatives are compared in the upper panels of Fig. 5.20. We remark that the intensity of T(E) in correspondence of the molecular resonances should approach unity; here, for computational time saving reasons, we decided to use an energy sampling lower than the optimal. The HOMO-LUMO gap of B molecules is lower with respect to the shorter A molecules, because the extension of the π electronic system is larger. If we compare the transmission functions of the diarylethene with different connecting groups (A1 vs. A2 and B1 vs. B2), we notice that the presence of the amide end-groups produces a slight shift of the peaks toward higher energies. This effect is due to the creation of different dipole moments at the interface, since the amide group is more electronegative than the methyl group. The determines a better alignment of the HOMO of the closed isomer with the Fermi level and, once a voltage is applied, we expect qualitatively a larger current in this case. Apart from this shift, the structure of the transmission function is not appreciably affected by the change of connecting groups.

Effect of applied bias

We now discuss the changes in the conductance for molecule B1 when the system is driven out of equilibrium by the application of a bias V. In Fig. 5.21 the transmission functions are reported for the closed (left panel) and open isomer (right panel) by increasing the voltage from the bottom pictures. For the closed molecule a bias of 1 V allows one to include the

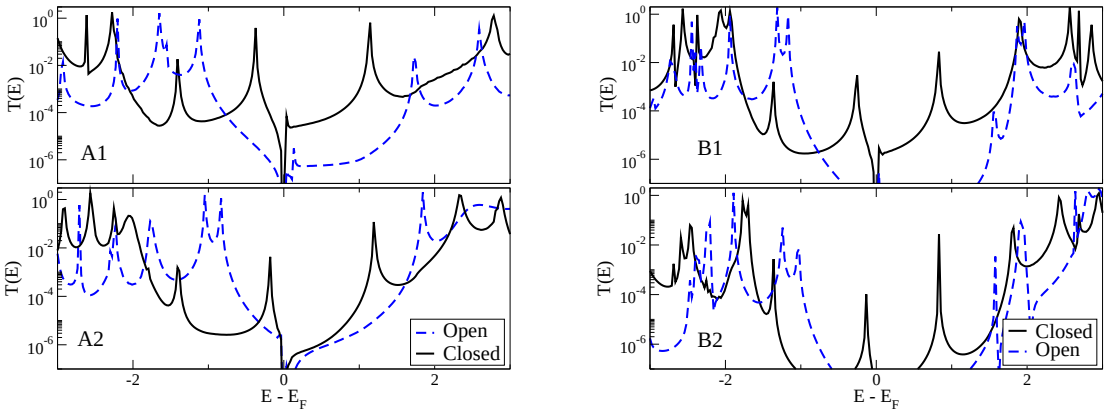

Figure 5.20: Transmission function of the closed (solid) and open (dotted) isomers of the A1,A2 (upper panel) and B1,B2 (lower panel) diarylethene derivatives.

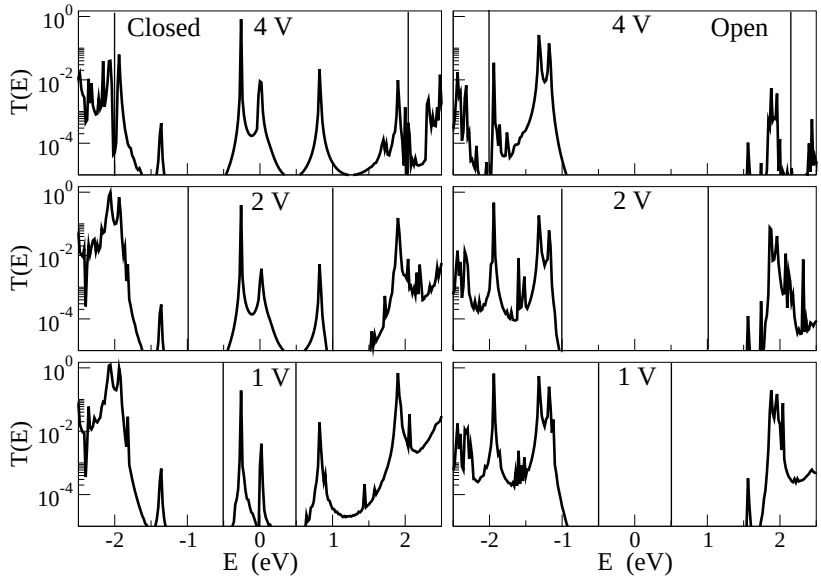

Figure 5.21: Transmission function of the closed (left) and open (right) isomers of the B1 diarylethene derivative at different applied biases (from bottom to top: 1V, 2V, 4V). The bias window is delimited by two vertical lines.

contribution of the HOMO in the admissible energy window (vertical lines), while a bias of 2 V is needed to contain the LUMO. We also observe two features from the edge resonances near E_F. In fact, as a finite bias is applied, edge states play a role, though small, in the transmission curve. A non negligible conductance asks for a bias $V = 4$ V for the open isomer. In both cases the HOMO-LUMO energy difference is unaffected by the applied voltage.

In conclusion, diarylethene based molecules can be switched between the two states by photochemical means. When used as a bridge between two Au electrodes, the switching occurs, usually in one direction only, due to quenching by the electrodes. For CNT electrodes too, the switching from open to closed isomers occurs through light, but the reverse does not [103]. We suggest the use of graphene as the electrode as (i) it has a lower density of states near the Fermi level in comparison with Au leading to lesser probability for quenching and (ii) the orientation of the molecule with respect to the graphene sheet can be changed chemically, tuning the interaction between the two components. In the polymeric state, the change from closed state to the open state can be induced not only by light, but also by electron/hole injection obtained by the application of a potential difference [90]. Consequently one may anticipate that in the case of diarylethene molecules connected to graphene, the switching from open to closed may be induced by light and the reverse by the application of a large potential difference. Looking at the positions of the LUMO/HOMO orbitals energies in the transmission curves given in Fig. 5.21, it seems possible to populate/depopulate them to a sizeable extent by the application of about 2 and 4 volts for the closed and open configurations, respectively. Thus one has the possibility of inducing switching in both directions, by the application of such a potential difference for a short period of time, and hence light may be avoided altogether.

Graphene versus CNT and Au contacts

A common problem of experimental realizations of diarylethene nanojunctions is that they usually show only one-way switching. In fact, in several experiments with gold electrodes the diarylethene derivatives switch from closed to open with visible light but not from open to closed with UV [97, 101]. This has been explained as a consequence of the quenching of the excited state of the open isomer by resonance energy transfer to the gold nanoparticles, which prevents the ring closure process. Theoretical studies suggest that the HOMO of the open isomer would be largely coupled with the $3d$ DOS of Au, resulting in a short lifetime of the HOMO which would prevent its depopulation by photoexcitation [99, 119]. With CNT electrodes, the situation is the opposite. Only the open-to-close reactions are allowed, but not the inverse [103]. From theoretical investigations, a possible reason is that the photoexcited electron has a high probability to transferring into the CNT leads before nuclear relaxation can occur [120]. In fact, the estimated lifetime of HOMO resonances for both isomers ranges from 230 to 360 fs, while the LUMO ones from 7 to 30 fs. These lifetimes should be compared to the characteristic switching times after photon absorption of diarylethene molecules, which

have been reported to range from sub-200 fs [121] to 900 fs [122]. Therefore, the lifetimes of HOMO are shorter than the times required for the isomerization process, which is in turn prevented. The molecule remains oxidized in the HOMO state for a time equal to its lifetime, after which an electron from the leads is injected restoring the molecular charge [120].

We present here preliminary results of the lifetimes τ of the main HOMO and LUMO resonances for B1 and B2 molecules with graphene leads as reported in Tab. 5.1. The lifetimes are estimated by extracting the full width half maximum (FWHM) of the molecular resonances in the PDOS calculated via the Green's function of the infinite system. The procedure will be explained in more detail in Chap. 7. The lifetimes are calculated from the GS orbitals, which for these system are a fair approximation of the photoexcited ones [120]. We

Table 5.1: Calculated resonance lifetimes for the open and closed isomers of B1 and B2.

	–CH_2– (B1)		–CO–NH– (B2)	
τ(fs)	HOMO	LUMO	HOMO	LUMO
Open	98	714	350	3138
Closed	387	134	631	8936

can notice that our calculated values are much larger than those in the case of CNT leads. This may be understood in terms of the DOS of graphene, which is very small near the Fermi level. As a consequence, the molecules hybridize poorly with the substrate, which may imply that the resonance widths are very small (in all the cases we considered lower than 20 meV). The resulting lifetimes appear therefore significantly larger than the characteristic switching times of diarylethene. Hence, our calculations suggest that by using graphene electrodes the probability of finding the photoexcited electron/hole on the molecule during the direct and inverse cyclization reactions is high. Therefore, double-way switching may be favored by using graphene electrodes. Finally, we notice that the lifetimes of the B2 isomer are larger than those of the B1. In fact, the amine bonds reduce the conjugation of the graphene-diarylenthene system, acting as resistive spacers between the molecule and the electrodes. In this case one expect a reduction of the molecule/leads hybridization.

5.4 Closing remarks

Very simple prototypes of carbon-based molecular junctions have been investigated in order to characterize their transport properties. In the first part of this chapter, aGNR have been considered as linkers between two semiinfinite graphene electrodes. These systems present a typical metal-semiconductor-metal behavior due to the electronic gap of the ribbons which depends on the their width. The electronic properties of the isolated subsystems, i.e. graphene electrodes and the nanoribbon, together with their interaction in contact regions determine the transport properties of the junction. The coupling between the subsystems is very efficient and the contacts do not create any appreciable barrier to transport due to

the same chemical species constituting the subsystems. Hence the transport properties are mainly determined by the shape (width and length) of the finite ribbon included in between the graphene leads. In spite of the simple model considered, the reported results on the electronic transport provide some parameters to control and engineer future carbon-based electronic devices. In the second part, we have calculated the conductance of diarylethene-based molecular junctions with graphene leads. Our calculations show that at zero bias the peaks in conductance of the diarylethene moiety attached to two graphene electrodes reflect not only the molecule electronic states broadened into resonances by the coupling to the leads, but also the features of graphene edge states. Near the Fermi energy (E_{F}) the conductance of the closed isomer is much lower in the energy interval between the HOMO and the LUMO resonances of the molecule, following the linear dependence of the electrode density of states (DOS) proportional to $|E - E_{\mathrm{F}}|$. In the same range the conductance of the open isomer is about zero. If we apply a finite bias we observe that conductance is allowed within different energy windows for the open and closed isomers. Finally, we have discussed the advantage of using graphene electrodes with respect to other materials, namely a reduced quenching of the photoexcited state compared to gold electrodes.

Chapter 6

Transport on a 3D system

6.1 Introduction

In this chapter we investigate the conductance properties of pyrazine single molecular junctions (SMJ) with platinum electrodes. This system has been found to display features which are critical to obtain reliable molecular switches. In fact, experiments suggest that it is a highly conductive system and it shows bi-stable states. We will refer to a recent experimental study carried on by M. Kiguchi and coworkers [123], who have performed MCBJ experiments on such devices.

Molecule-based electronics have attracted wide attention due to their potential application for ultra small electronic devices. Utilization of bi-stable states in SMJs as memory, switch, and other components, is a key issue in the realization of molecular electronics. Recently, several single molecular switches showing bi-stable states have been reported using photochromic molecules, 1,6-hexanedithiol, 4,4-bipyridine, and other molecules, thanks to the recent development of experimental techniques (e.g. STM break junction, MCBJ) [124, 107, 125]. Especially, single bipyridine molecule switches has been intensely studied, because Au-N or Au-NH2 bonds provide fixed conductance values [107, 126, 127, 128, 129] which are critically important to obtain reliable single molecular switches.

However, investigation on single molecular switch is still open to further research. First, the conductance value of the on-state of single molecule switches is often too low (below 0.01 G_0) [125, 107]. This can be a problem for the application of SMJ to realistic devices. Second, all the evidence for switching behavior has been indirect because the experiments are "blind": the geometrical configuration of the device at the atomic scale is not known. In view of this uncertainties, theoretical *ab initio* calculations can offer good insight into the driving effects in molecular devices, giving light to the mechanism of the transition between bi-stable states.

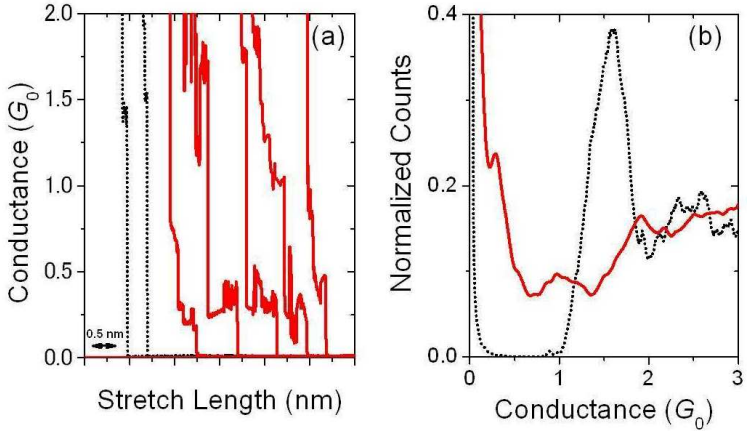

Figure 6.1: (a) Conductance traces, (b) conductance histograms of the Pt contacts before (black curve) and after (red curve) the introduction of pyrazine. The bias voltage is set to 300 mV. The conductance histogram is constructed from 1000 conductance traces of breaking metal contacts. The intensity of the conductance histograms is normalized with the number of the conductance traces.

6.2 Experiments: Pt/pyrazine junction

In order to improve the conductance of the single molecule junction (SMJ), one needs to focus on the metal-molecule contact. In a conventional SMJ, the molecules are attached to the metal electrodes via anchoring groups (e. g. thiol, amine) [130, 131, 132, 133, 134, 135, 136]. Although a stable SMJ can be prepared in this way, the anchoring group acts as a resistive spacer, leading to a lower conductivity. Recently, the direct binding of the π conjugated molecule to the metal electrode has been found to improve the conductance of SMJ [137, 138]. The efficient overlap between π orbitals of the molecule and the metal states leads to higher conductivity. In fact, the π orbitals, including p orbital of nitrogen, can directly bind to the metal electrodes. The introduction of nitrogen atoms in the molecule back-bone of pyrazine could also fix the binding site with the metal electrodes, and σ bonds are formed between lone pair of nitrogen atom and the metal, which in principle could lead to a decrease in the variability of the conductance values owing to multiple stable configurations [132].
The choice of metal electrodes can also be critical to the performance of the junction. In a simple tunneling model, the conductance of SMJ depends on the LDOS of the contact metal atoms at the Fermi level [5]. In contrast with Au, which is the most commonly adopted metal, Pt yields a narrow $5d$ band located at E_{F} and a higher LDOS. In addition, molecular orbitals can effectively hybridize with d orbitals of Pt. Thus, a higher conductivity is expected by using Pt as metal electrodes. Actually, the increase in conductance of SMJ has been reported for various molecules including benzene, H_2 and benzenedithiol [136, 137, 139, 140, 141].

Fig. 6.1-(a) displays typical conductance traces as a function of the stretch length. Before the introduction of pyrazine, the conductance decreases in a stepwise fashion, showing the

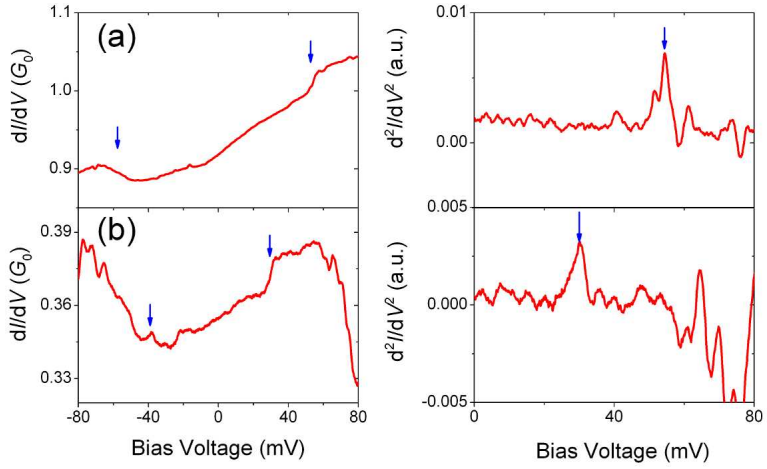

Figure 6.2: Differential conductance spectra and its derivative of single pyrazine molecule junction taken at (a) high and (b) low conductance regime.

last plateaus around 1.5 G_0. The corresponding conductance histograms Fig. 6.1-(b) show a peak around 1.5 G_0, which corresponds to clean Pt atomic contacts [5]. After introducing the pyrazine molecule, the peak at the position characteristic for Pt atomic contacts is suppressed, and a large weight is added in the entire range below that value. On top of this background, distinct features are found around 1.0 G_0 and 0.3 G_0. Their appearance indicates the existence of two distinct states, namely a low conductance state (LC), and a high conductance one (HC). It is noteworthy that the 0.3 G_0 plateau appears after the 1 G_0 plateau as shown in the last two traces in Fig. 6.1-(a), which implies the distance between metal electrodes to be larger for the low conductance state. In order to characterize the atomic configuration of the SMJ, inelastic tunneling electron spectroscopy [142, 143, 144, 145, 146] (IETS) has been worked out at both HC and LC regimes. In brief, in IETS measurements the electrodes are kept at a fixed distance, while the voltage is increased. Above a certain voltage bias, the incoming electrons have sufficient energy to excite a vibration mode of the SMJ. Fig. 6.2 displays differential conductance and its derivative at HC (a) and LC (b) regimes. Symmetric upward kinks were observed in differential conductance around 30 meV for the LC state and 60 meV for the HC one (Fig. 6.2-(a)). Accordingly, clear symmetric peaks appear in the derivatives in Fig. 6.2-(b). The conductance enhancement is explained by the opening of an additional tunneling channel for electrons that lost energy to a vibration mode [140, 141, 142, 143, 144, 145, 146, 3]. The temperature dependence of the $\frac{d^2I}{dV^2}$ curves confirms that the peaks originated from the excitation of vibration mode. Since the phonon mode of Pt is below 20 meV (T mode: 6, 10 meV, L mode: 20 meV) [147], the observed modes correspond to vibrations of the Pt-molecule bond or internal molecular vibrations, confirming the formation on the pyrazine bridge. The different vibrational energy of HC and LC states clearly suggest that the two distinct states display two different atomic configurations.

6.3 Methods

We have carried out first-principles calculations for several model structures in order to shed light on the experimental observations of bi-stable states in Pt/pyrazine junctions. The electronic structure calculations are carried out using the SIESTA package [29, 30]. The exchange-correlation energy and electron-ion interaction are described by the Perdew-Burke-Ernzerhof (PBE) generalized gradient approximation [52] and norm-conserving pseudopotentials in the fully nonlocal form, respectively. A single-ζ polarized basis set of numerical atomic orbitals is used, and the energy cutoff for real-space mesh is set to 200 Ry. We tested this basis for Pt bulk. The calculated band structure and DOS are presented in Fig. 6.3. They are in good agreement with those in Ref. [148]. The total DOS in the region shown is almost entirely due to d states, except for the s contribution at the bottom of the d band, which indicates the hybridization of the nearby empty s band with the valence d band. We verified that using a double-ζ polarized basis set does not modify our results. With these parameters we calculated an optimal lattice parameter for bulk Pt equal to 4.0 Å. For the other species (i.e. N,C,H) we used a double-ζ polarized basis set.

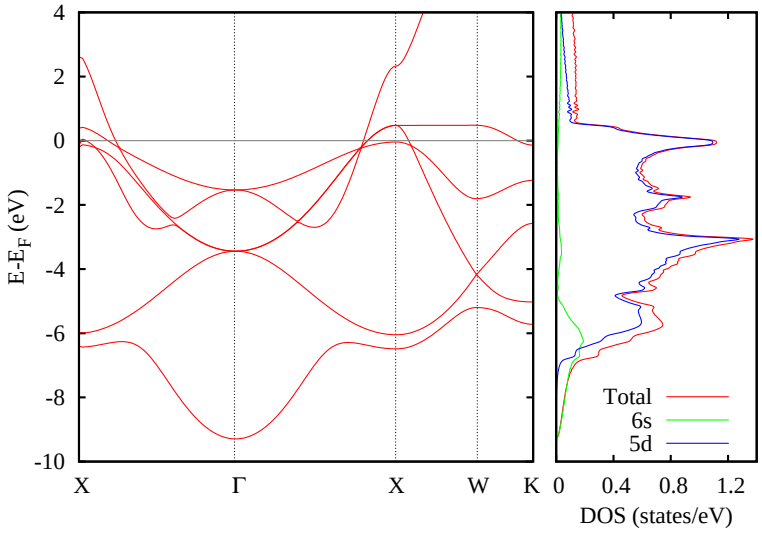

Figure 6.3: Band structure, DOS and projected DOS on ($5d$, $6s$) orbitals of bulk Pt.

In order to describe the molecular junction we consider a periodic supercell, where the junction is oriented along the z axis, as represented in Fig. 6.4. In most cases, the contact is modeled by considering a pyramidal Pt_4 tip placed at the top of a Pt(111) 3×3 surface unit cell. The slab contains 10 atomic layers. We define the length D as the distance between the outermost Pt layers, as shown in Fig. 6.4. For the electronic structure calculations we used a 3×3 **k**-mesh in the x, y plane; the transmission functions are instead calculated by using a 5×5 **k**-mesh. We first relaxed the single electrode (5 Pt layers) containing the Pt_4 tip and then used the obtained geometry to build the junction configuration. All the subsequent relaxations are performed by keeping all the atomic positions of the electrodes fixed and

allowing for relaxing the 8 Pt cluster atoms as well as the pyrazine ones until residual forces are smaller than 0.04eV/Å.

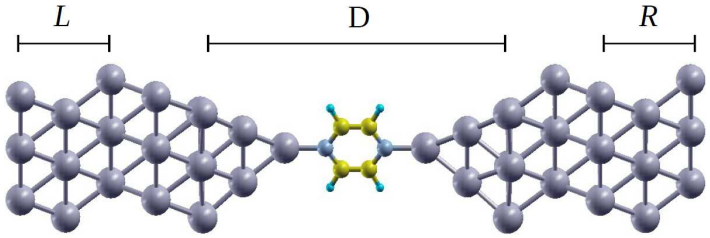

Figure 6.4: Molecular junction setup. The left and right electrodes portions and the electrode distance D are pointed out by segments L, R, and D, respectively.

6.4 Results

In order to determine the most suitable contact configuration to adopt, we calculated the adsorption energies for different structures. We considered the adsorption on top of a pyramidal Pt_4 cluster, on the hollow and bridge sites of a Pt_3 cluster, and on the hollow and top sites of the clean Pt(111) surface. In Fig. 6.5 the relaxed structure as well as the adsorption energies for all five configurations are reported. The most stable contact configuration is the pyramidal Pt_4 electrode, placed on top of Pt(111). The surface top adsorption is unfavored with respect to the Pt_4 top one due to the steric repulsion between the molecule and the surface Pt atoms. Our calculations also suggest that pyrazine adsorbed on a hollow site is unstable, and that N selectively forms a bond on the top of a Pt atom. According to

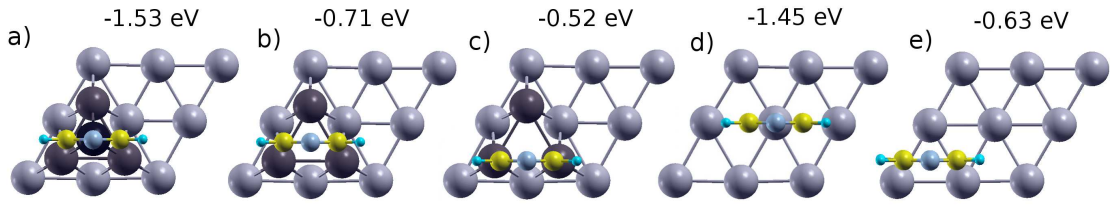

Figure 6.5: Adsorption energies of pyrazine on different electrode geometries: a) on top of Pt_4 cluster, on b) hollow site and c) bridge site of a Pt_3 cluster, on the d) top site and e) hollow site of the clean Pt(111) surface.

these results we modeled the tips as composed by two Pt_4 pyramids placed on top of a 3×3 Pt(111) surface (as described in the previous Section), which seems to be compatible with the experimental setup.

Fig. 6.6 displays how the structural and transport properties of the junction change with the stretching. We measure such properties as a function of D, the distance between the Pt surfaces. Here, d_{Tips} is the distance between the apical Pt atoms, $\alpha_{1,2}$ are defined as the angles between the straight line of the N-N molecular backbone and that defined by the N-Pt bonds (as shown in the inset), E_{form} is the junction formation energy calculated as $\mathrm{E}_{form} = \mathrm{E}_{Pt-molecule-Pt} - 2\mathrm{E}_{Pt} - \mathrm{E}_{molecule}$, and $T(E_F)$ is the transmission function at the Fermi level. By looking at Fig. 6.6-(a) two regimes can be distinguished. A high conductance regime is observed for distances D lower than 14.5 Å, where the conductance is comprised in a range between 1.3 G_0 and 1.5 G_0. In this regime the tilt angles $\alpha_{1,2}$ are lower than 120°, meaning that the molecule sits in a tilted configuration with respect to the junction axis. The electronic coupling between the molecule π orbitals and the d orbitals of the Pt tip is favored due to the orientation of the molecule, and correspondingly the transmission function increases inversely by increasing $\alpha_{1,2}$. The transmission does not change in a range between D=13.0 Å and 14.5 Å, and shows a HC plateau. In the range between 14.3 Å and 14.7 Å, we assist to a rapid rotation of the molecule, which overcomes an energy barrier (Fig. 6.6-(b))

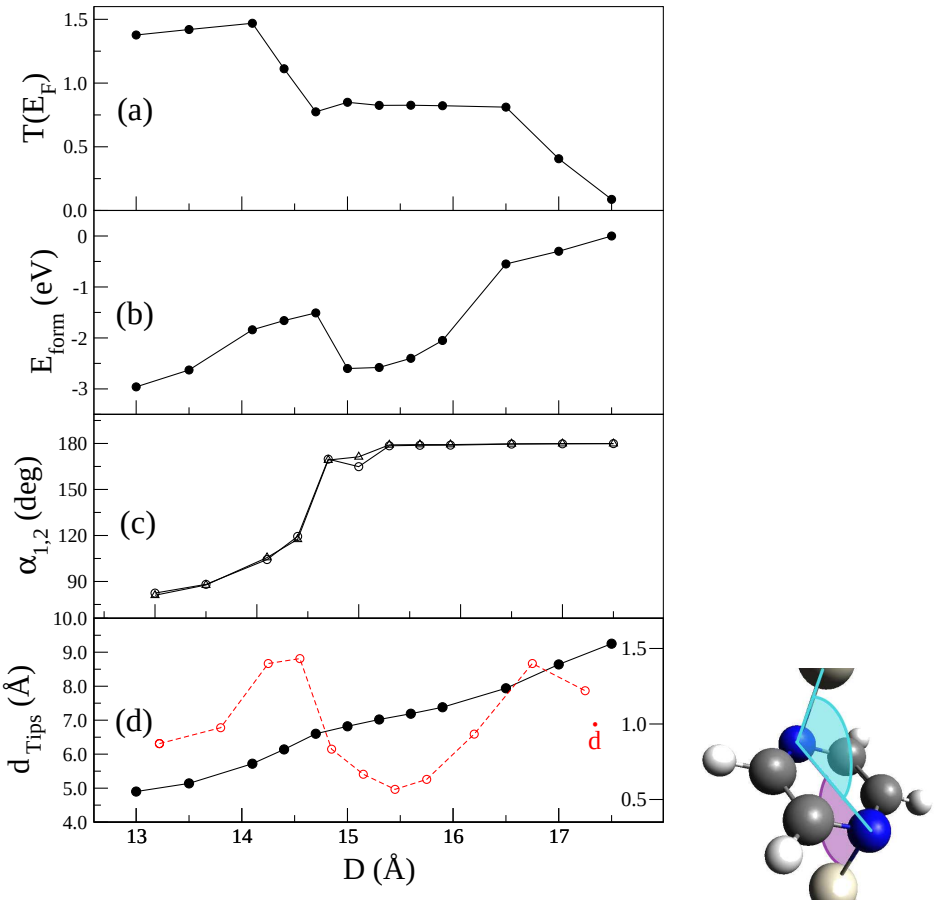

Figure 6.6: Pyrazine/Pt junction properties plotted against the surface distance D: zero-bias transmission function $T(E_F)$ (a), junction formation energy E_{form} (b), bending angles $\alpha_{1,2}$ (c), distance d_{Tips} between the outermost Pt atoms (d) and its derivative d' (red dashed). The inset illustrates the bending angles $\alpha_{1,2}$.

to reach a local energy minimum corresponding to a LC state. In this regime the pyrazine is aligned with the junction axis, i.e. $\alpha_{1,2}$ are equal to 180°; this reflects in a lower coupling between the molecule orbitals and those of the Pt. As a consequence, we notice that the transmission $T(E_F)$ assumes fractional values and its intensity is fairly constant and equal to 0.7 G_0 for a range of about 2 Å. This is in agreement with the appearance of a low conductance feature in the conductance histogram (Fig. 6.1-(b)). When D is larger than 16.5 Å the Pt-N bond is broken causing an abrupt decay of $T(E_F)$ to zero, while also the formation energy tends to zero. During the junction elongation d_{Tips} increases almost linearly (Fig. 6.6-(d)), while the peaks in its derivative give signal of transition between different regimes.
We assign the experimental high and low conductance states to the two regimes highlighted by first-principles calculations. In agreement with the conductance traces, the low conductance plateau appears after the high conductance one and extends for a longer range. The differences between theory and experiments regarding the conductance intensities are due to the intrinsic limitations of ground-state DFT applied to electronic transport, as the underestimation of the HOMO-LUMO gap and the self-interaction error [149]. In fact, even in the prototypical case of benzenedithiol/Au junction, the DFT-NEGF approach overestimates any experimental conductance by at least 1 order of magnitude [150]. In our case we don't find such a dramatic discrepacy, since the system shows a strong metal-molecule coupling. We also point out that in our approach we have followed the molecule stretching along the minimum energy path obtaining a bi-stable junction where conductance results are in fairly good agreement with the experimental ones. For this reason we did not work out an average over several molecular configurations.
In order to obtain a more comprehensive view of the electronic properties, in Fig. 6.7 we show the projected density of states (PDOS) onto the basis orbitals associated with the N,C species and the 5*d* orbitals of Pt for a representative state in each conductance regime (D=13.5 Å solid line and D=15.3 Å dashed line). Calculations reveal that in both cases the pyrazine HOMO orbital is highly hybridized with the Pt states and it is the main contribution for the conductance at E_{F}. At the same time, the D=15.3 Å junction shows more pronounced peaks, which signals a lower hybridization of the molecular orbitals with respect to the D=13.5 Å case. As mentioned, this is due to the different bending angles formed by the pyrazine with the junction. Accordingly, in the upper panel, we see that the overall conductance for D=13.5 Å is larger not only near E_{F}, but also in a broader energy range. In fact, the transmission coefficient depends on the metal-molecule coupling. For the bent structure, the coupling is larger due to a higher hybridization of the pyrazine π orbitals, polarized orthoghonally to the molecular plane, and the metal *d* orbitals which stem from the undercoordination of the surface Pt atoms. The result of the bending is a higher overlap between the respective wavefunctions, which leads to larger hybridization and conductance.
To obtain information about the individual channels contribution to the conduction, we have calculated the eigenchannels [151] for these two reference configurations. The outcome is that in the high conductance regime two channels are open and equally contribute to the charge

transport, while only one is present in the low conductance regime. In Fig. 6.8 such transport channels are depicted to provide an intuitive picture of transport. For D=15.3 Å the symmetry and the spatial distribution of the channel has the same character of the π-type HOMO of pyrazine, while for D=13.5 Å the two channels display a stronger interaction between the states of Pt atoms and those of the molecule.

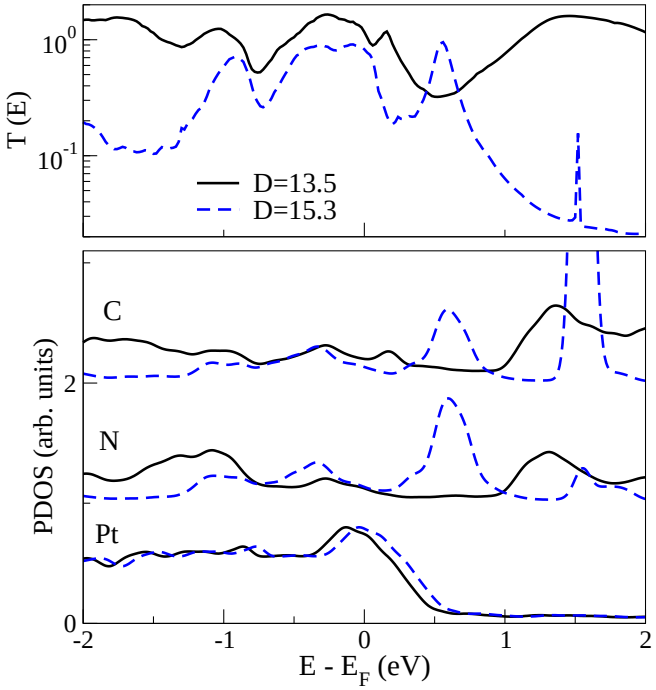

Figure 6.7: Upper panel: transmission function T(E) of Pt/pyrazine junctions for HC and LC structures calculated for two representative distances D, namely 13.5 Å (black solid line) and 15.3 Å (blue dashed line). Lower panel: PDOS of the same structures on the C and N orbitals and on the Pt 5*d* orbital.

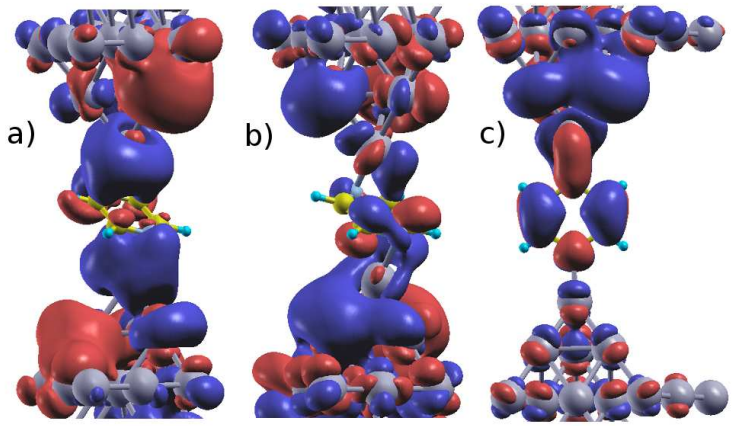

Figure 6.8: Isosurface plots of the most transmitting eigenchannels of the high and low conductance structures at two representative distances D. a-b) first and second eigenchannel for D=13.5 Å. c) single eigenchannel for D=15.3 Å. The real part of the scattering state is shown.

Anchoring geometry

So far, we have considered that pyrazine is attached to the leads by its N atoms. This is the most intuitive configuration, due to the natural directionality of the molecule. We also explored the possibility of a different anchoring, namely by its two C atoms: in Fig 6.9 the two anchoring configurations are sketched. In Tab. 6.1 we report the energy differences of the relaxed C- and N- anchored molecular junctions at different electrode distances D. We verified that the N- anchoring is always energetically favored. However, at low D the bending of the molecule allows also for the C- anchoring, with an energy cost of less than 0.1 eV. On the other hand, at larger electrodes separations (D>14.5 Å) the molecule sits coaxially with the junction and the C- linking is unfavorable, as the steric repulsion between H and Pt costs more than 1 eV. We calculated the transmission function for the C- anchoring in the case of D=13.2 Å, and we found that $T(E_F)$ is approximately 1.5 G_0, that is even higher than in the N- anchoring case. This further confirms that the HC regime can be attributed to a bent contact configuration of the pyrazine.

Table 6.1: Energy differences between C- and N- anchoring at different surface distances

D(Å)	ΔE (eV)
13.20	0.07
13.50	0.05
14.10	0.20
15.3	1.19

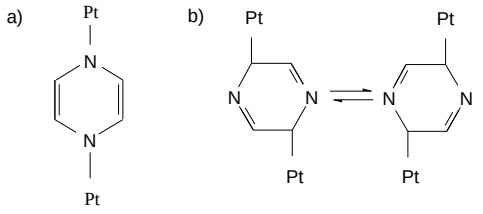

Figure 6.9: Chemical sketch of C- and N- anchoring.

Vibrational properties

The experimental measurements provided an estimate of the energy of the IETS-active vibration modes of the SMJ, that is 60 meV and 30 meV for HC and LC configurations, respectively. Theoretical calculations can help identifying which modes are activated in experiments. We performed DFT calculations in order to calculate the vibrational modes of pyrazine/Pt junctions for the geometries obtained at different D. We used finite Pt clusters to represent the electrodes and we kept all the Pt atom fixed, which is justified by the large difference between the mass of Pt and that of the other species involved. In Fig. 6.10 we show the stretching dependence of the relevant vibration modes. The lowest three modes envolve rigid vibrations of the entire molecule with respect to the Pt junction. As a consequence, their energy is strongly affected by the stretching (D). At distances D$>$ 15 Å, there are two possible candidates for the LC mode observed with IETS. Namely, these modes consist in a shuffling of the molecule in the z direction and in a frustrated rotation of the molecule with respect to the axis of its plane. Unlike the third rigid mode shown, their energy dependence on D is the same. Their vibrational energy increases while the molecule is progressively rotated and slowly decreases once it is coaxial with the junction. On the other side, the possible candidates for the HC mode are internal vibrations of the pyrazine. We display the configuration of the two most likely ones in Fig. 6.11.

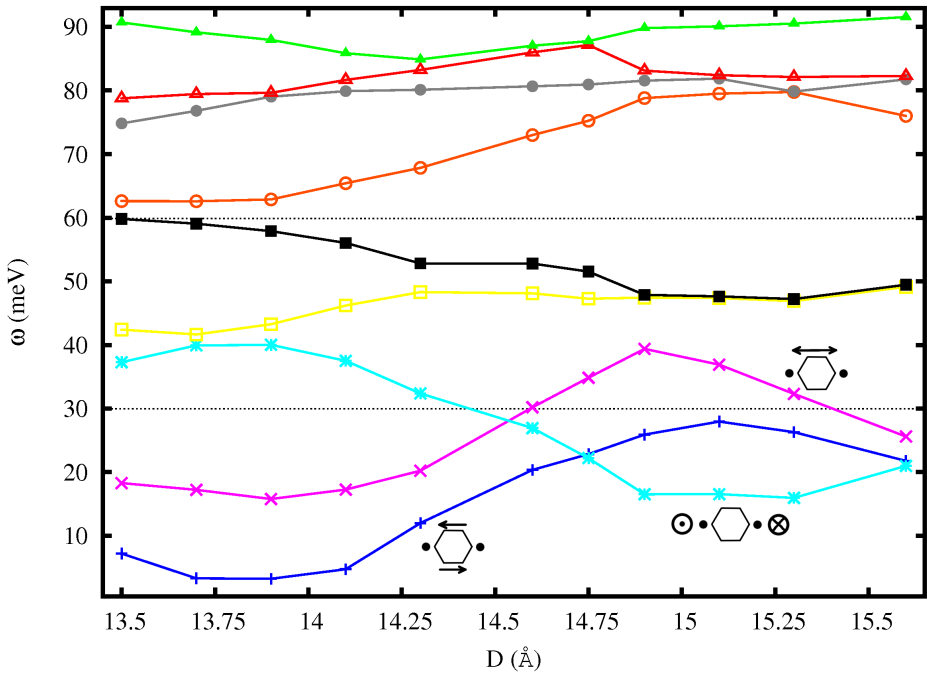

Figure 6.10: Stretching dependence of the relevant vibration modes of pyrazine/Pt involved in the experiments. The insets represent the character of the lowest 3 modes, which involve a collective vibration of the molecule with respect to the Pt junction. The two dotted lines correspond to the experimental vibrational energies for small and large stretching distances.

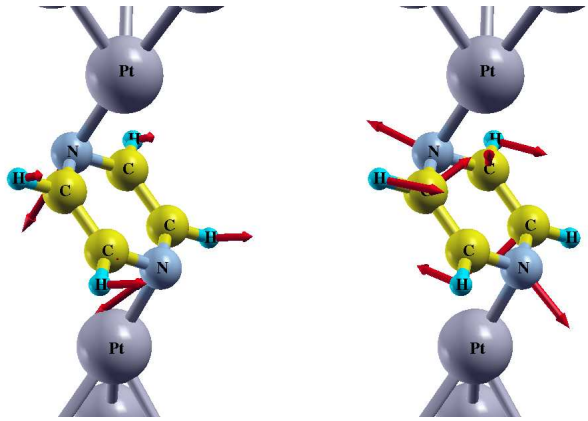

Figure 6.11: Internal vibrations with energy around 60 meV for the tilt molecule configuration.

Bi-stable switching

After revealing the existence of bi-stable structures, and charactering their atomic configurations, experiments demonstrated mechanically controlled conductance switching in single pyrazine molecular junction. By imposing a repeated mechanical elongation/compression by applying an AC voltage (triangle wave) to a piezo element. The resulting displacement

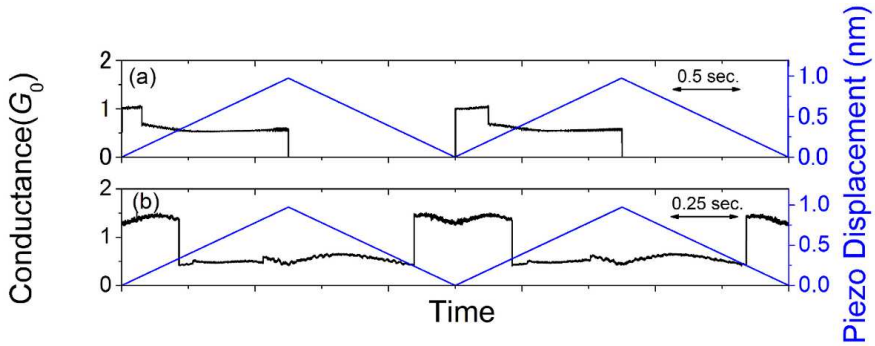

Figure 6.12: Sample pyridine switching conductance traces. These trace were collected while applying the linear ramps (dashed black line) shown measured at a 100 mV applied bias. The displacement was 1.0 nm, and the modulation frequency was (a) 0.8 Hz and (b) 0.4 Hz. Curve (a) shows the transition among high and low conductance states and breaking the junction, while curve (b) shows the transition between high and low conductance states.

amounted to 1.0 nm at a modulation frequency of 0.4∼0.8 Hz. Fig. 6.12 shows some examples of conductance switching of single pyrazine molecule junction. Curve (a) shows the transition among high and low conductance states and breaking the junction, while curve (b) shows the transition between high and low conductance states. Although the conductance gradually changed in the high or low conductance, a discrete change was observed between high and low conductance states. Such a discrete change in response to the smooth triangle-wave perturbations confirms that the conductance switching indeed occurs via transitions between two particular metal-molecule contact configurations. Finally, the conductance traces in Fig. 6.12 clearly show that the junction is controllably modulated between the high and low conductance state by mechanical modulation.

6.5 Closing remarks

We investigated the bi-stable conductance of highly conductive single-molecule pyrazine/Pt junctions. Break-junction measurements show two distinct conductance states of 1.0 G_0 and 0.3 G_0. As a support to experiments, first-principles calculations reveal that the two stable states can be ascribed to different geometrical configurations in which the pyrazine axis is bent and coaxial with the junction, to which correspond high and low couplings of the molecular orbitals with the electrodes, respectively. IETS measurements and theoretical calculation of the vibrations further characterized the configuration-specific conductance of such junctions. These findings allow us to prove the reversibility of the process, which has ultimately been achieved by only mechanical manipulation of the junction.

Chapter 7

Resonant charge transfer

7.1 Introduction

In this chapter, the Non Equilibrium Green's function formalism described in Chap. 3 is applied to study resonant charge transfer. In principle, this is a problem different from charge transport, but which has a strong connection with it. Our interest is to study electronic charge transfer in systems composed of a molecule/atom (or an overlayer of them) adsorbed on a surface of a given substrate, which may be either metallic or insulating. This problem is relevant in surface chemistry, catalysis and organic photovoltaics because the charge transfer determines the time of localization of an electronic excitation and thus the reactivity of an adsorbate. For instance, the dye-sensitized solar cell (DSSC) [152] harvest light energy by utilizing a transition metal complex or an organic dye adsorbed on a substrate, which in most cases is TiO_2 or ZnO. Light irradiation excites an electron from an occupied state (usually the HOMO) to an excited resonance of the dye, and it is then transferred to the continuum of states of the substrate. The oxidized dye is restored to its reduced form by a redox pair in solution, and a photocurrent can be generated in the circuit. Thus, one of the key ingredients to improve the efficiency of DSSCs is to maximize the electron injection rate. A theoretical method to predict the relative rates of charge transfer can be beneficial to determine which molecule and which configurations are the more efficient ones.

Unless they lie within a projected band gap of the substrate the states of an adsorbed molecule become resonances of the semiinfinite substrate/molecule system, i.e., they are no more eigenstates of the system. Molecular resonances do not have well defined energies any longer, rather they are broadened and display a finite width. The latter quantity can be related to the time required for an electron to delocalize into the substrate, that is the time needed to depopulate the molecular excited state. We refer to this width as the "elastic linewidth" and to its inverse as the "elastic lifetime" [153]. These quantities are difficult to calculate with DFT by a slab model. This model consists in representing the substrate with a slab whose periodic replica along the direction normal to the surface are separated by a vacuum region. Usually a slab model involves subbands whose energy difference is larger

than the typical linewidths. Therefore, a model which takes into account the true infinite substrate is necessary to resolve such quantities.

Our method relies on the Green's function of the semiinfinite system, which can be obtained in conjunction with DFT as explained in Chap. 3. From this quantity, one can then extract the correct elastic width. In Sect. 7.2, we describe this method in detail. Then, Sect. 7.3 is devoted to an application of the method to a test system, namely Cs-p(2x2)-Cu(111). Finally, in Sect. 7.4, we discuss preliminar studies of charge transfer of organic dyes on TiO_2 surfaces.

7.2 Methods

We outline the details of our method. As shown in Sect. 2.3, a localized basis set is adopted to describe the system Hamiltonian. We perform DFT calculations to obtain the electronic structure of a symmetric slab in which an adsorbate is present on both surfaces. Then, the ground-state Hamiltonian is used to compute the Green's function G (see Eq. 3.36) of the infinite system comprising the two surfaces separated by a vacuum region which prevents their direct interaction, following the same scheme described in Sect. 3.4. In other words, the scattering region is formed here by two decorated surfaces without direct interaction and separated by a large vacuum gap. The effect of the two semiinfinite substrates is described by the corresponding self-energies introduced in Sect. 3.4.1. Thus, the current flowing through the system is negligible. One technical point which is worth commenting refers to the aling-ment of the electronic structure of the periodic electrode calculation and that of the scattering region. In the case of metal electrodes, they are aligned by taking the Fermi level as a common reference. Of course, this is not possible in the case of non-metallic electrodes, since the Fermi level is no more a well defined quantity. An alternative way is thus to calculate the planar average potential (PAV) along the direction normal to the surface, and to align the PAVs of the different (electrode and scattering region) calculations. The latter procedure has been used here for the TiO_2 substrate calculations.

The matrix elements of the Green's function are defined so that

$$G(\mathbf{r},\mathbf{r}';E,\mathbf{k}_\parallel) = \sum_{ij} G^{ij}(E,\mathbf{k}_\parallel)\phi_i(\mathbf{k}_\parallel,\mathbf{r})\phi_j^*(\mathbf{k}_\parallel,\mathbf{r}') \quad , \tag{7.1}$$

where $\mathbf{k}_\parallel$ is the crystalline momentum parallel to the surface plane, $\phi_i(\mathbf{k}_\parallel,\mathbf{r})$ are the basis functions defined as Bloch combinations of the atomic orbitals $\varphi_i(\mathbf{r})$ at the atomic positions $\mathbf{R}_\alpha$:

$$\phi_i(\mathbf{k}_\parallel,\mathbf{r}) = \sum_\alpha e^{-i\mathbf{k}_\parallel\cdot\mathbf{R}_\alpha}\varphi_i(\mathbf{r}-\mathbf{R}_\alpha) \quad . \tag{7.2}$$

The Green's function allows us to calculate the DOS and the PDOS onto selected orbitals. If $S_{ij}(\mathbf{k}_\parallel)$ is the overlap matrix between the Bloch combinations of the localized basis orbitals

$\{\phi_i(\mathbf{k}_\parallel)\}$ and $G_{ij} = \langle\phi_i|G|\phi_j\rangle$, the PDOS over a set of orbitals Ω [a] can be calculated as:

$$\rho(E,\mathbf{k}_\parallel) = -\frac{1}{\pi}\mathrm{Im}\sum_{i\in\Omega}\sum_{j} S_{ij}(\mathbf{k}_\parallel)G_{ij}(E,\mathbf{k}_\parallel) \quad . \tag{7.3}$$

The DOS can be also projected onto a given initial wavepacket. In fact, in the case of an adsorbed molecule, the most intuitive picture is that the electron initially lies in a state corresponding to a molecular eigenstate. By a preliminar calculation of the isolated molecule/overlayer, we can extract the coefficients $\{c_i(\mathbf{k}_\parallel)\}_{i\in N}$ corresponding to the expansion of a given molecular orbital onto the basis, N being the dimension of the basis. Then, the DOS can be projected onto this precise molecular orbital (MO):

$$\rho(E,\mathbf{k}_\parallel) = -\frac{1}{\pi}\mathrm{Im}\sum_{i,j\in\mathrm{MO}}\sum_{k,l} c_i(\mathbf{k}_\parallel)^* c_j(\mathbf{k}_\parallel)S^*_{ik}G_{kl}(E,\mathbf{k}_\parallel)S_{lj} \quad . \tag{7.4}$$

In order to calculate the widths W of the surface resonances, we fit the projected density of states at different $\mathbf{k}$-points with a Lorentzian,

$$\rho(E,\mathbf{k}_\parallel) \simeq \frac{A(\mathbf{k}_\parallel)}{(E-\epsilon)^2 + (W_{fit}(\mathbf{k}_\parallel)/2)^2} \quad . \tag{7.5}$$

From this fit, we obtain the elastic width $W_{\mathrm{fit}}(\mathbf{k}_\parallel)$ as a function of $\mathbf{k}_\parallel$. To obtain the physical width, we need to subtract the small imaginary part η added to the energy in the calculation of the Green's function (see Eq. 3.36): $W(\mathbf{k}_\parallel) = W_{\mathrm{fit}}(\mathbf{k}_\parallel) - \eta$. In our case, η is always quite small, of the order of 1.0 meV. Given the uncertainty relation $\Delta E\Delta\tau \sim \hbar$, the inverse of W gives the time constant for the decay of the resonance population due to elastic processes, i.e. the resonant elastic lifetime: $\tau_{\mathbf{k}_\parallel} = \hbar W^{-1}_{\mathbf{k}_\parallel}$. The $\mathbf{k}_\parallel$-dependence of the width (and the lifetime) has been explicitly written, as the width can change due to the dispersion of the resonance or to the coupling of the resonance with states of the substrate with different character/symmetry at different $\mathbf{k}_\parallel$ points (particularly when small cells along the lateral directions are used in the calculations). In the present calculations, however, we will concentrate in the elastic width calculated at the supercell Γ point. For our calculation of molecular dyes on TiO_2, where relatively large supercells are used, we consider that this can be taken as a reasonable approximation to the total elastic width of the molecular resonances, i.e, $W \simeq W_\Gamma$.

Being DFT a ground state theory, the energy of the electron excited states as deduced from the Kohn-Sham spectra does not necessarily have a good correspondance with the experimental values. Therefore the molecular resonances may not lie in their real positions. Fortunately some errors, like underestimating both the energy gap of the substrate and that of the adsorbate, tend to calcel out. However, in certain cases we are interested in calculating the elastic lifetime as we shift the molecular electronic states with respect to the substrate bands (see Fig. 7.1) by means of a scissor-like operator. To do this, we add a small energy shift $\Delta\varepsilon$ to the terms of the Hamiltonian matrix H_{ij} belonging to the adsorbate:

$$H_{ij} = \begin{cases} H_{ij} & i,j \notin \text{adsorbate} \\ H_{ij} + S_{ij}\Delta\varepsilon & i,j \in \text{adsorbate} \end{cases} \tag{7.6}$$

[a] Typically we take those of the adsorbed molecule.

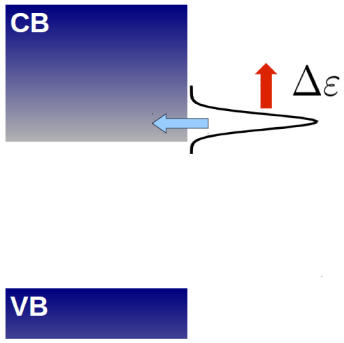

Figure 7.1: Diagram of the adsorbate resonances and substrate bands. The red arrow symbolizes the energy shift of the resonances.

Accordingly, all the adsorbate resonances are shifted by the same energy amount $\Delta\varepsilon$ and their position relative to the substrate states can be tuned.

7.3 Cs-p(2x2)-Cu(111)

We apply the method described in previous Section to evaluate the electronic properties and electron dynamics of Cs-p(2x2)-Cu(111). This system has been already discussed in the literature, and both the electronic structure and the electron dynamics have been explored by means of the embedding theory[154] and recursive methods to obtain the surface Green's function [153, 155]. From experiments and theory it is well known that the (111) surfaces of noble metals exhibit a projected band gap around $\bar{\Gamma}$. As a consequence, the (111) surfaces of Au, Ag and Cu exhibit a well-defined partially occupied surface state. This state has a free-electron-like dispersion with its minimum at $\bar{\Gamma}$. As we move to lower binding energies we can also find the image state series in these surfaces. Electrons occupying surface states close to the Fermi level (E_F) extend far toward vacuum and, therefore, play an important role in the adsorption of weakly physisorbed species. Adsorption of alkali overlayers introduces a significant change in the electronic structure of the surface. Charge transfer from the alkali layer to the metal reduces appreciably the work function and new states appear at the interface, such as quantum well states (QWS). QWS are quasi two-dimensional states confined between the substrate and the vacuum barrier. The adsorption of alkali atoms in p(2x2) superstructures causes the folding of the projected bulk bands: as a consequence, the gap near E_F of Cu(111) is closed. In the case of Cs-p(2x2)-Cu(111), the presence of the overlayer allows the QWS to couple with the substrate bands: the effective hybridization results in a finite lifetime of the state. In the following, we will discuss the band structure of the system and the elastic lifetime of the QWS.

7.3.1 Model

The electronic structure calculations are carried out using the first-principles self-consistent method implemented in SIESTA package [29, 30]. The exchange-correlation energy and electron−ion interaction are described by the Perdew-Burke-Ernzerhof (PBE)[52] generalized gradient approximation (GGA) and norm-conserving pseudopotentials [32] in the fully nonlocal form, respectively. The dynamic properties are calculated with the TranSIESTA code [38], which combines the NEGF technique with density functional theory.

Our unit cell consists in a slab of 13 Cu layers, and a Cs adatom on both the upper and lower surfaces. The vacuum space between the periodic replicas of the slab is set to 17 Å: this guarantees that the overlaps of the basis functions of the atoms forming different surfaces are zero, and therefore the periodic replicas are decoupled. We use a 2x2 surface unit cell, thus the supercell is formed by 52 Cu atoms plus 2 Cs atoms. A double-ζ polarized (DZP) basis set of numerical atomic orbitals is used and the energy cutoff for real-space mesh is set to 300 Ry. [29] For Cu our DZP basis set includes $4s$, $4p$ and $3d$ orbitals, while for Cs $6s$ and $6p$ orbitals are considered. We fix the radii of the orbitals by imposing an energy shift of 0.02 Ry. The resulting cutoff radii of the different species are then $r_{3d} = 3.6$, $r_{4s,4p} = 6.4$ Bohr for Cu and $r_{6s,6p} = 9.9$ Bohr for Cs. The cell has been fully relaxed with a force tolerance of 0.04 eV/Å and by using a 10x10 **k**-mesh. We verified a 10x10 **k**-mesh is enough to obtain a converged band structure. We also tested the convergence of the bands with respect to the energy cutoff and found no noticeable differences from 150 Ry to 400 Ry. We opted for a value of 300 Ry and used it for all the subsequent calculations.

7.3.2 Results

In the following, we will analyze the electronic properties of the structures obtained from SIESTA calculations. In Fig. 7.2 we illustrate the band structure of Cs-p(2x2)-Cu(111) along the Γ-M direction and the PDOS on the Cs orbitals at Γ. Also, the band structure of the clean Cu(111) and of the Cs isolated layer are reported for a direct comparison. Below ~ -1.4 eV the band structure is characterized by a dense contribution of the $3d$ bands. Unlike the case of the clean Cu(111), no energy gap is found around E_F at Γ due to the p-(2x2) superstructure. The gap only opens above $\sim$ 1.5 eV, in good agreement with previous results [155]. By comparing the band structure of the surfaces with and without the Cs overlayers, we were able to identify two main QWSs, which are marked by solid black symbols. The QWS1 is located at $\Gamma \sim -0.3$ eV below the Fermi level, and it can interact with the bands of the substrate. On the contrary, the QWS2 lies in the energy gap, at $\sim$ 3 eV above the Fermi level, in agreement with [154]. If we compare the band structure of Cs-p(2x2)-Cu(111) with that of the free-standing Cs layer, we notice the large shift of the QWS2. This upward shift can be interpreted as a result of the confinement of this state with large p_z character, associated with the presence of the Cu surface. On the left side of Fig. 7.2, the PDOS over the Cs orbitals calculated at the Γ point is shown. Two well defined peaks are found in correspondence to

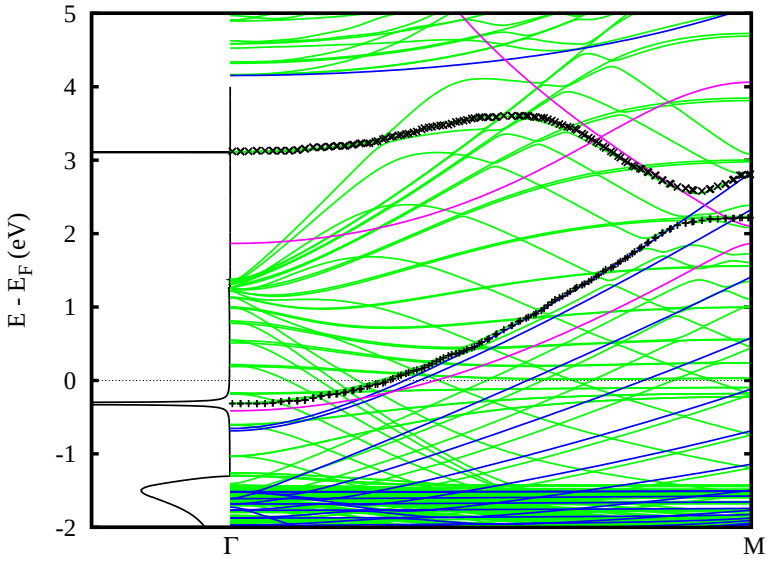

Figure 7.2: Band structure of Cs-p(2x2)-Cu(111) (green), and PDOS on the Cs orbitals at Γ (black). Band structure of the clean Cu(111)-(1x1) (blue) and of the Cs unsupported layer (pink). The QWS are highlighted by black symbols.

the QWSs. While the QWS1 has a finite width, QWS2 has a discrete character as it lies within a gap. Below 1.4 eV we notice that there is also a (very small) contribution due to the mixing of the Cs states with the 3d states of the substrate. After fitting of the QWS1 PDOS with a Lorentzian curve as in Eq. 7.5, we found an elastic linewidth $W \simeq$7.0 meV. This is in good agreement with previous results: Chis et. al. found a value of 2.4 meV [154], while Sánchez-Portal et. al. found a value of 9.4 meV [155].

Our results show a discrepancy with respect to the previous ones: in our case the QWS1 lies slightly below E_F, while it has been previously found about 0.1 eV above E_F. This can be attributed to a different basis set effect and a slightly different relaxed geometry. Anyway, we are interested in understanding what would be the change of W if the QWS1 were localized at higher energies, and therefore we apply an energy shift $\Delta\varepsilon$ to the Cs states. In Tab.7.1 we show the changes in W as $\Delta\varepsilon$ increases. We notice that W decreases as the QWS1 is shifted at higher energies. This is probably related to the progressive change of the character of the bands in the Cu substrate in that energy range, that include for 4p character as we move to higher energies. The Cs QWS1 has a strong s character at Γ. When we shift the QWS at a value close to the one found in previous results, we obtain $W \simeq$5.10 meV, which is in closer agreement with the results in Ref. [154].

E-E_F (eV)	W (meV)
-0.31	7.00
0.02	5.56
0.10	5.10
0.19	4.65
0.27	4.16

Table 7.1: Resonances width W versus the quantum well state energy position (determined by applying an energy shift $\Delta\varepsilon$) for Cs-p(2x2)-Cu(111).

7.4 Organic dyes on TiO_2

The scope of this Section is to show preliminary results obtained for the study of charge transfer of physical systems relevant for organic photovaltaics. As mentioned in the introduction to this chapter, the lifetimes of resonant excited states of organic dyes on TiO_2 surfaces are basic quantities to control the efficiency of DSSCs. In this study, we consider organic chromophores bound to the (110) surface of rutile TiO_2.

In DSSCs, the mesoporous oxide layer is actually composed of TiO_2 nanoparticles of $10 - 30$ nm size [152]. Several crystal forms of TiO_2 occur naturally: rutile, anatase, and brookite. The study presented here is performed exclusively on the (110) surface of rutile since (i) the rutile is the thermodinamically more stable form, (ii) the rutile (110) surface is the most stable crystal face and (iii) the crystal structure of rutile reduces the complexity of the supercell used in our approach. Two classes of dyes are used for DSSCs applications: organometallic complexes and organic chromophores. The latter ones exhibit many advantages: easy design of diverse molecular structure forms, low cost, higher molar extinction coefficients and efficiences with respect to metallic complexes. Generally, organic dyes display a donor–π-spacer–acceptor (D-π-A) structure. The HOMO wavefunction is usually localized on the donor end side. On the contrary, the LUMO is more localized on the acceptor part, the same one to which usually the molecule is anchored to the TiO_2 surface. A good localization of the LUMO near the surface improves the charge transfer to the substrate. The π-spacer is a conjugated bridge usually composed of a sequence of C=C bonds, or thiophene rings or a mixture of them. Its length and composition can be controlled experimentally, influencing the efficiency of the device. In our study, we will consider triarylamine (TAA) dyes. This class of organic sensitizers has been investigated widely due to the prominent electrondonating ability and hole-transport properties of the triarylamine unit[152, 156]. To date, a very large number of dyes with triarylamine as electron donor have been developed and most of them have shown good power conversion efficiencies in DSCs. In fact, TAA derivatives display efficiencies which range from 3.3% to 9.8% [152].

After calculating the electronic properties of the molecules in gas phase, we calculate the ground-state of the dye-oxide interface by optimizing the adsorption structure. Then, we compute the linewidth of the relevant molecular resonances. This can be in principle

calculated as a function of different factors like the dye conjugation length, the adsorption geometry, the functionalization, the defects in the surface, the effect of the electrolyte solution, and eventually also the dye's vibrations (by introducing a dynamics of the system). In the present work, we will only focus on the first aspect, namely the influence of the spacer. Other aspects, like those mentioned above, will be studied with the methodology presented as a future development of the work described here.

7.4.1 Rutile TiO_2

The unit cell of rutile TiO_2 is tetragonal with two titanium and four oxygen atoms (Fig. 7.3). We calculated the bulk structure of rutile by using a 15×15×25 **k**-grid, a mesh cutoff of

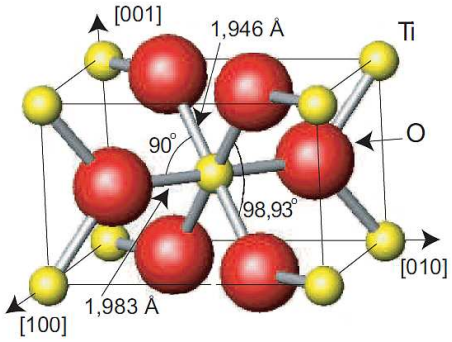

Figure 7.3: The unit cell of rutile TiO_2.

400 Ry, and the PBE exchange-correlation functional. Rutile TiO_2 is a wide band gap semiconductor with a band gap of ~ 3.02 eV. By inspecting the decomposed density of states in Fig. 7.4, calculated with a DZP basis, we can see that the valence band is composed of O $2p$ states, while the conduction band consists mainly of contributions from Ti $3d$ orbitals. As expected, the band gap is underestimated by DFT, with a value of 1.5 eV. In order to balance the computational effort with the precision of the results, we tested our results with respect to three different basis sets, namely double-ζ polarized (DZP), double-ζ (DZ) and single-ζ (SZ). Minimal single-ζ are the more inexpensive with only 6 and 4 orbitals, respectively for Ti and O. In the other extreme, DZP basis contain 15 orbitals for Ti and 13 for O. After relaxing the structure, the two inequivalent lattice parameters along the [100] and [010] directions assume the value of a=4.526 Å b=2.904 Å for SZ, a=4.588 Å b=2.958 Å for DZ, a=4.627 Å b=2.990 Å for DZP, in good agreement with the experimental results of a=4.594 Å b=2.959 Å (deviations are 1.66%, 0.08% and 0.88% respectively) [157]. In Fig. 7.5 the band structure of bulk rutile is calculated with those three different basis sets. Our results are in fair agreement with previous ones [157]. We notice that the DZ basis set provides results that are very close to those obtained with DZP. Also, the SZ bands are in good agreement with the DZP ones in the energy region relevant to our purpose, that is in a range of ~ 2 eV below the valence band (VB) maximum and above the conduction band (CB) minimum. Out of that region, discrepancy increases even if the results are quite reasonable even for the SZ basis.

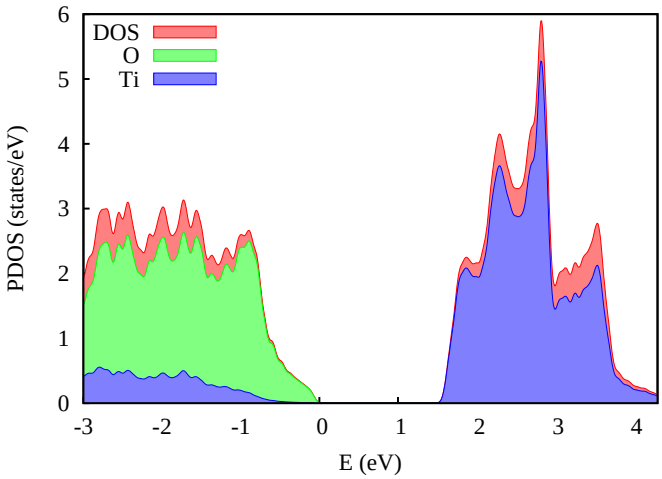

Figure 7.4: Total DOS (red), PDOS on O (green) and on Ti (blue) of rutile TiO_2.

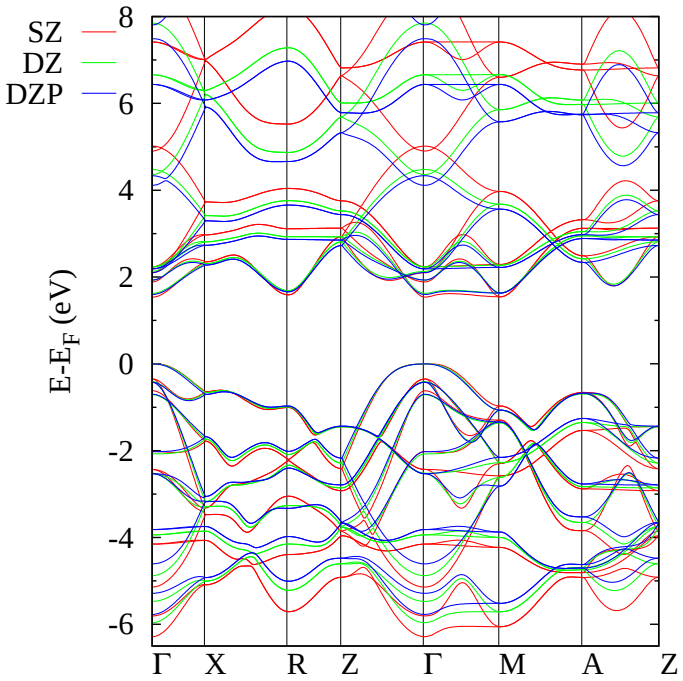

Figure 7.5: Band structure of rutile TiO_2 along high-simmetry directions of the first Brillouin zone. The valence band maximum is taken as the energy zero.

The (110) surface of rutile TiO_2 is shown in Fig. 7.6 The surface consists of rows of bridging oxygen atoms (O_b) that lie above the in-plane surface, which are 2-fold coordinated, whereas the in-plane O atoms on the surface are 3-fold coordinated (O_{3f}). The O_b atoms are located directly on top of 6-fold coordinated Ti (Ti_{6f}) rows, and Ti atoms not bound to O_b atoms are 5-fold coordinated (Ti_{5f}). Complexively, the structure is composed by trilayers disposed along the [110] direction with different stacking. We calculated the properties of

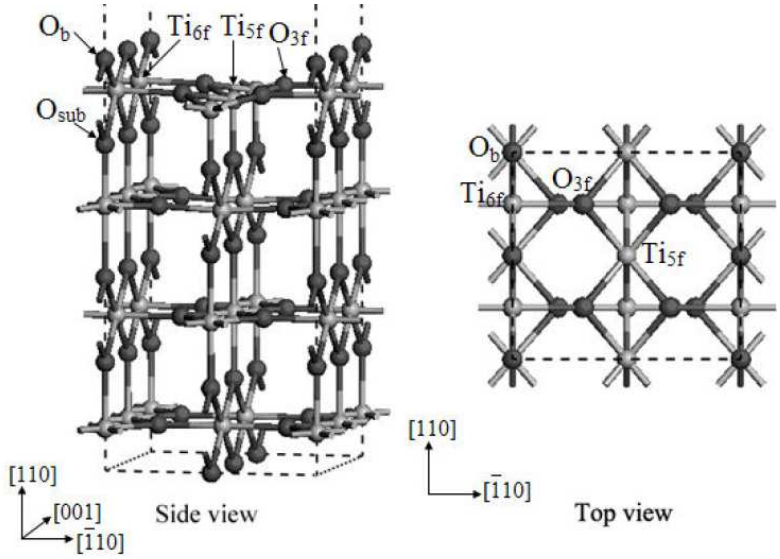

Figure 7.6: Side and top view of the rutile TiO_2 (110) slab showing the 2×1 surface unit cell.

rutile TiO_2 (110) considering a slab with 7 trilayers showing the 1×1 surface unit cell, with a total of 42 atoms. We set a $8{\times}16{\times}1$ **k**-grid and a mesh cutoff of 350 Ry, we used both DZP and SZ basis sets and let relaxing all the atoms in the supercell. The structural parameters are in agreement with experiments [158] for both basis sets, since we correctly predict positive upward shifts for Ti_{6f}, O_b, O_{sub} and a negative one for Ti_{5f}. The band structure along with the DOS are shown in Fig. 7.7. The DZP bands exhibit good agreement with previous calculations [159]. The SZ basis set also provides a good estimate, even if the gap at Γ is 0.1 eV lower than with DZP.

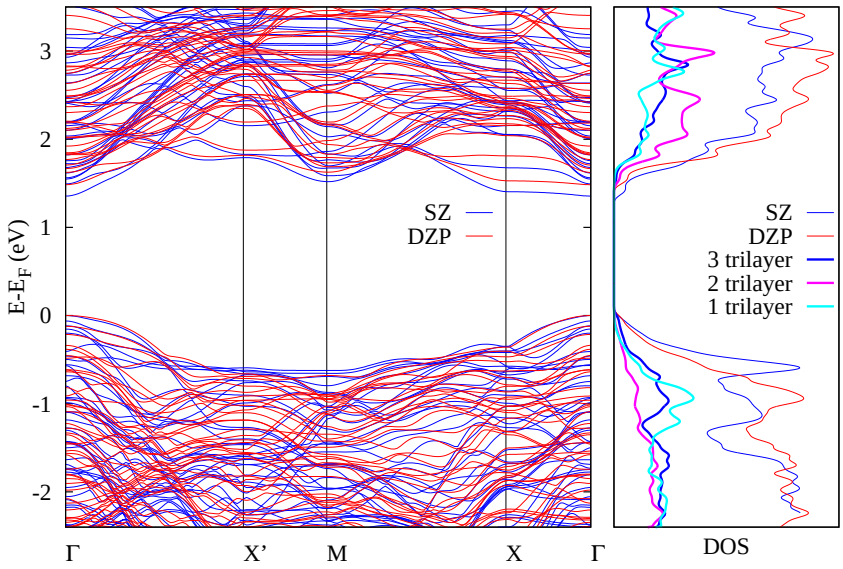

Figure 7.7: Left panel: band structure of rutile TiO_2 (110)-1x1 for DZP and SZ basis sets. Right panel; DOS calculated with DZP and SZ, and projection of the outermost 3 trilayers (the latter are shown only in the case of DZP). The valence band maxima are taken as the energy zero.

7.4.2 Dyes on TiO2

Model

The supercell used to calculate the resonant lifetimes of dyes on rutile TiO_2 is shown in Fig. 7.8: it consists of 9 rutile trilayers with a 1x3 surface periodicity plus two symmetric dyes, with a total number of 218 atoms. The left and right "electrode" regions are indicated: periodic calculations of those structures provide the left and right self-energies used to build the Green's function of the infinite system. Test calculations have shown that using symmetric slab with molecules attached to both the surfaces is necessary. In fact, using an asymmetric slab with only a single molecule induces a spurious electric field across the slab, which introduces problems regarding (i) the alignment of the molecular levels with the substrate bands and (ii) the alignment of the electronic levels of the slab calculation with the one of the electrodes. The molecules considered are TAA derivatives, which will be discussed in more detail in the following.

In this work we choose to consider chromophores anchored to the TiO_2 surface with a carboxylic acid group bound to a pair of undercoordinated Ti atoms on the exposed surface, as many chromophores reported are attached to the TiO_2 surface in this way. The bidentate bridging dissociative conformation, where the carboxylic acid binds to two Ti atoms and the hydrogen is dissociated, is known to be the energetically most stable for rutile (110) [160, 161, 162, 163]. We considered the dissociate H to be adsorbed on the bridging O which is

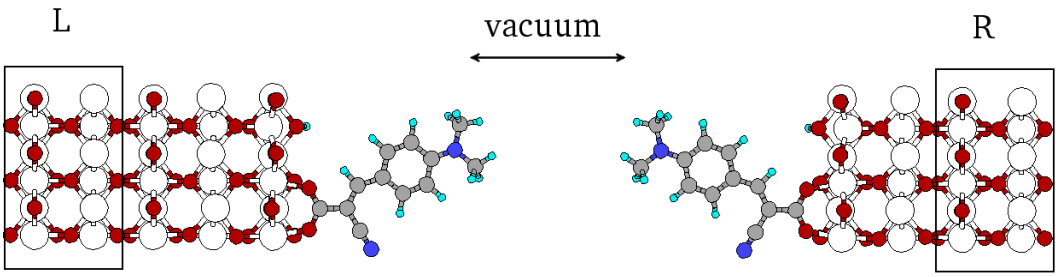

Figure 7.8: Scheme of the supercell. The TiO_2 slab thickness is 9 rutile trilayers and we have considered a 1×3 surface periodicity. The left (L) and right (R) portions considered as electrodes are indicated. Two TAA derivatives are anchored to the surfaces via the bidentate dissociative conformation. The two molecules are separated by a vacuum region.

furthest from the molecule. However, preliminar tests show that a different choice for the H adsorption site has no influence on the electronic properties.

A major difficulty in the calculations is given by the complexity the system. While accurate calculations are needed to reliably describe the structural and electronic configuration, the large dimensions of the systems to be studied substantially limit the viable level of accuracy. Thus, we adopt the following procedure. The first stage is the search for the most stable configuration. To this end, we relax the structure with high accuracy. In order to obtain reliable structures, we use a DZP basis. We consider a symmetric slab with 5 trilayers and relax the atoms of the molecules as well as those of the outermost two trilayers until residual forces are below 0.04 eV/Å . After this procedure, we build the large supercell of Fig. 7.8 by using the relaxed atomic coordinates. In order to combine accuracy and efficiency, the calculations of the larger supercell are performed by considering a DZ basis for the TiO_2 orbitals and a DZP basis for the molecule ones. In fact, we have shown in the previous Section that the electronic properties of the TiO_2 are well described by a DZ basis. After calculating the system Green's function, we follow the procedure described in Sect. 7.2 to calculate the elastic linewidth and lifetime.

Molecules

We considered the TAA structure as the representative starting point for designing the dyes in our work. A simple configuration of such molecules is the dye **d1** of Fig. 7.9: the triarylamine unit is well known for its ease in oxidation of the nitrogen center and acts as donor which is connected via a conjugated spacer to the carboxylic endgroup. For reasons of computational efficiency, we consider slight modifications of this molecule, namely the configuration **d2** of Fig. 7.9. In the latter, the two terminal phenyl rings are substitued by two methyl groups. By doing so, a smaller TiO_2 surface supercell can be employed (see Fig. 7.8) thus decreasing significantly the computational effort. This substitution does not alterate significantly the

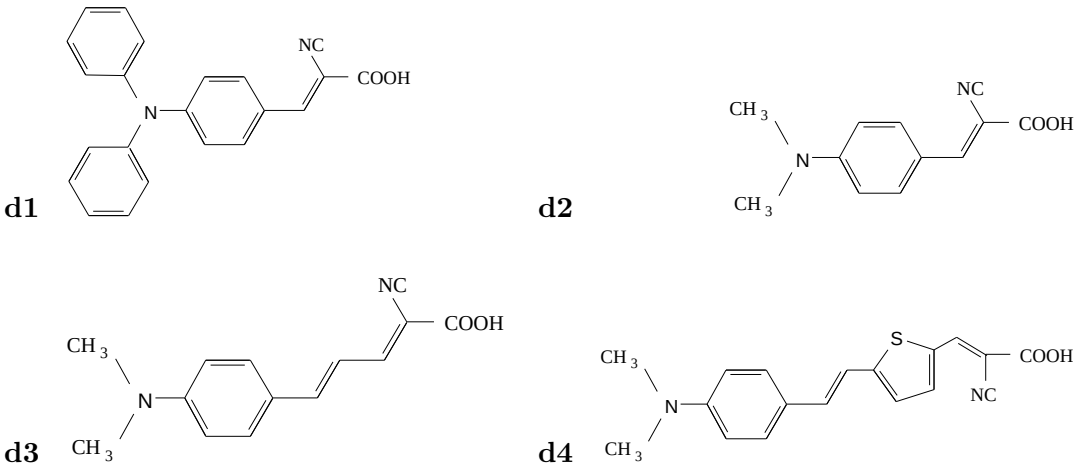

Figure 7.9: Molecular structures of sensitizers **d1**–**d4** with D-π-A configuration.

electronic structure of the dye. In fact, the energy gap varies from 2.2 eV to 1.9 eV, and the spatial localization of the molecular orbitals relevant to our purpose is the same. In particular, in Fig. 7.10 we can compare the HOMO and LUMO wavefunctions of **d1** and **d2** in gas phase. In both cases, we notice that the HOMO is delocalized along the whole molecule with predominant weight on the donor part, while on the contrary the LUMO is localized on the acceptor part, which facilitates the injection of photoelectrons into the substrate. The configurations **d3** and **d4** differ from **d2** by the length of the π-spacer: in the configuration **d3** the donor and acceptor parts are separated by a polyenic chain which is longer with respect to **d1**, while in the configuration **d4** a thiophene is inserted in the π-spacer. In Fig. 7.10 the HOMO and LUMO wavefunctions of all the molecules considered in this work are illustrated. Far all four dyes **d1**–**4**, the HOMO is quite delocalized over the whole molecule with a larger weight on the donor part, while the LUMO is mainly centered on the acceptor unit. The lowest energy adsorption corresponds to the $\pi - \pi^*$ intramolecular transition [164].

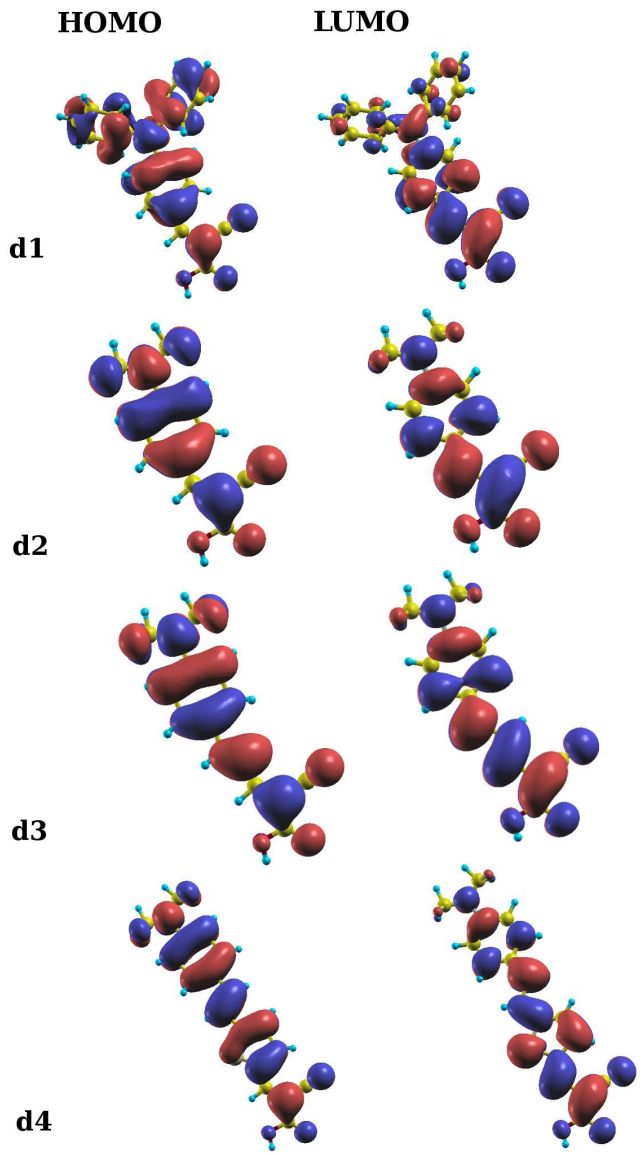

Figure 7.10: HOMO and LUMO wavefunction of the **d1**, **d2**, **d4** and **d4** dyes calculated with DFT for the molecules in gas phase.

Electronic properties of dye-TiO_2 systems

In this Section we show the results of our calculations. In Fig. 7.11 we report the total DOS, the PDOS onto the atomic species of the molecules, and the PDOS on the first TiO_2 trilayer of the slab for the three molecular configurations we studied. The energy axis is rescaled with respect to the valence band maximum (VBM). In each case, the HOMO resonance lies within the TiO_2 bandgap, near the edge of the valence band, and it is completely filled [b]. The HOMO has a large weight on the N of the triarylamine unit, as expected for this class of organic dyes. On the other hand, the LUMO resonance lies inside the TiO_2 conduction band, and it is completely hybridized with the electronic states of the substrate. The main features to be considered are the decreasing of its linewidth by increasing the π-spacer length, and its corresponding shift towards the conduction band minimum (CBM). This can be explained considering the increasing spacial extension (and the π system delocalization) of the molecules from **d2** to **d4**. This is also consistent with the increase of molecular resonances in the selected energy region. The position of the LUMO resonance critically affects the electron injection rate if the resonance lies near the CBM. Also, if the LUMO lies at the very edge of the conduction band, the injection mechanism can change to a direct excitation of an electron from the dye HOMO to the TiO_2 states [164]. The exact position of the LUMO level is less crucial if it is fairly above the CBM.

We calculated the elastic linewidths of these structures. The values of the LUMO resonant linewidths W and resonant lifetimes τ are illustrated in Tab. 7.2. The resonant lifetime of **d4** is in excellent agreement with the value reported in Ref. [165], which has been calculated with a different method. Our results indicate that the resonant lifetime increases from 3.3 fs to 18.8 fs by increasing the π-spacer length. As a consequence, the electron injection in the substrate occurs more slowly for systems with a large π-spacer. This is due to the increase of the delocalization of the molecular states in the longer molecule, as well as to the smaller density of states of the substrate approaching the CBM, which slows the electron transfer. Eventually, longer spacer may shift the LUMO resonance inside the TiO_2 bandgap, forcing the injection mechanism to change. However, it is well known that once electrons are injected into the substrate, they relax toward the bottom of the conduction band. In a DSSC system, this effect reduces the open-circuit voltage. Therefore, the exact position of the LUMO level might not influence the device performance unless the injection rate is largey affected by this position. This will be studied in more detail in the following.

Theoretical studies based on DFT-PBE calculations can only provide qualitative predictions of the position of the molecular levels with respect to the substrate ones. For this reason, we are interested in evaluating the resonant linewidth as the LUMO assumes different energy positions inside the conduction band. To this end, we focus on the molecule **d4**, whose LUMO

[b] In other words, the Fermi level lies somewhere within the energy gap and above the HOMO resonance.

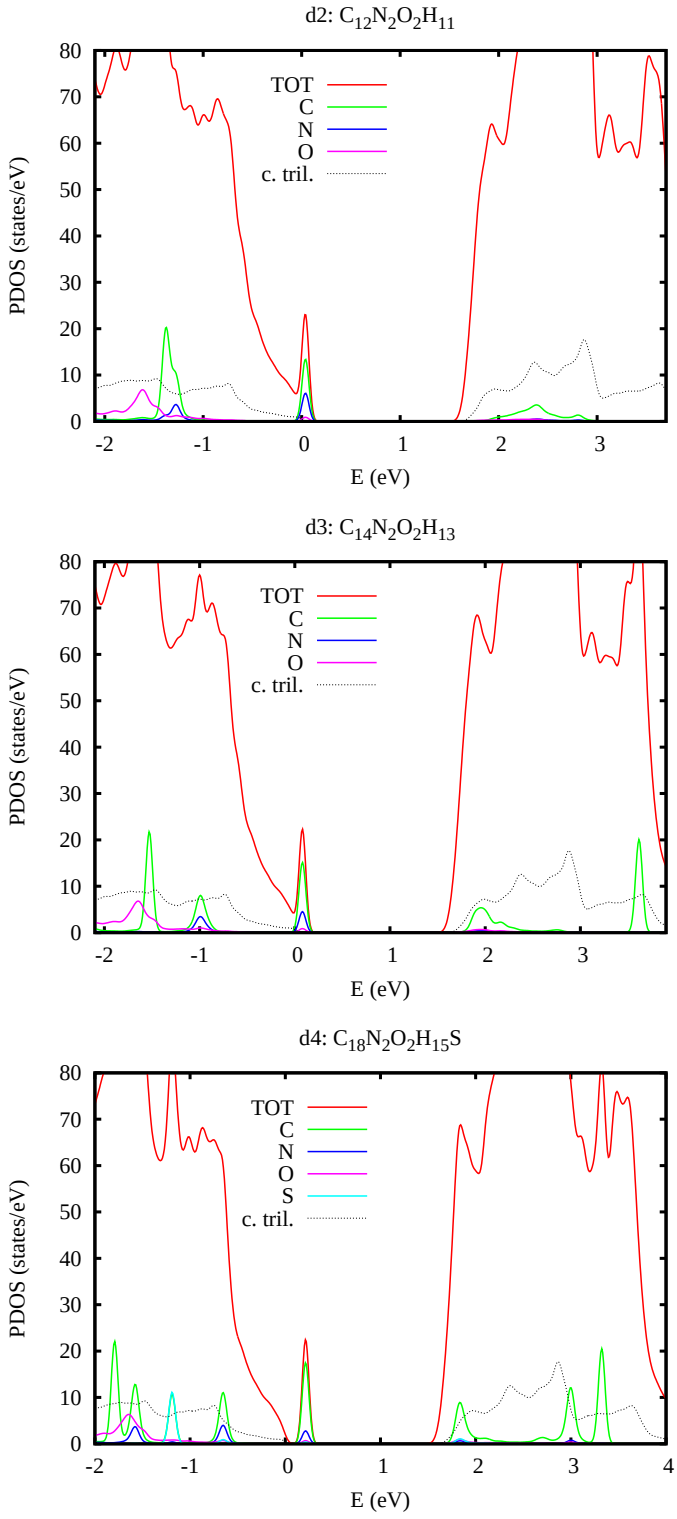

Figure 7.11: From top to bottom: DOS, PDOS on the different species belonging to the dye and PDOS on the central trilayer of the slab of the dyes **d2**, **d3** and **d4**. The energy axis has been rescaled by taking the VBM as zero.

molecule	W (meV)	τ (fs)
d2	200.3	3.3
d3	41.7	15.8
d4	35.8	18.4

Table 7.2: LUMO resonant linewidth W and resonant lifetime τ for the molecules considered in this work.

is the closest to the CBM, and shift its positions by different values $\Delta\varepsilon$. In Fig. 7.12 the PDOS on the LUMO is shown for different energy shifts. While for $\Delta\varepsilon = 0$ the PDOS displays a well defined peak, as $\Delta\varepsilon$ increases the LUMO interacts with the electronic states of the TiO_2 substrate, giving rise to a split structure composed of two components that complicate the analysis. We fitted these two (left/right) components with two different Lorentzian functions as in Eq. 7.5 extracting two values of W (namely, left and right components). In Fig. 7.13 (a) the variation of W for the left/right Lorentzian components are illustrated as a function of $\Delta\varepsilon$. In Fig. 7.13 (b) one can find the center of the two Lorentzians as a function of $\Delta\varepsilon$, together with the relative weight of the two components. At zero and large values of $\Delta\varepsilon$ the spectra consist mostly of a single peak (that clearly shifts with $\Delta\varepsilon$), and the position and width of the molecular resonance can be easily estimated. Comparing the results of the width for zero and the largest shift we can see that there is only a very moderate increase of the width with a shift of almost 1 eV. The region of intermediate shifts becomes more complicated and points to the existence of a surface resonance in TiO_2 in this energy range that can couple to the LUMO resonance. As expected, the TiO_2 resonance presents a larger width than the LUMO level and does not significantly disperse with the applied shift (which is restricted to orbitals residing in the molecular dye).

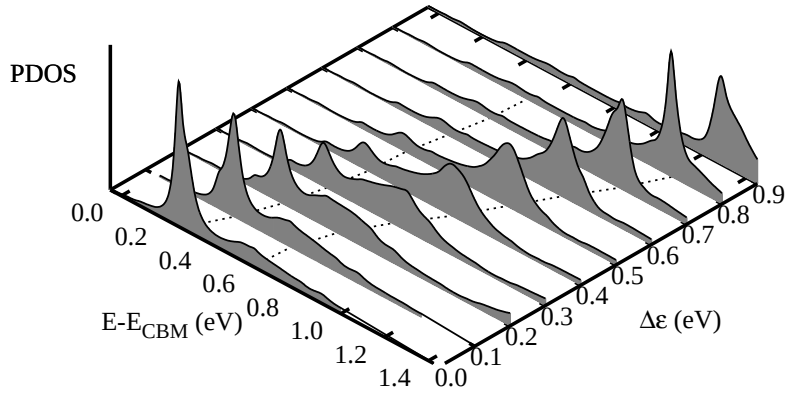

Figure 7.12: PDOS on the LUMO for the dye **d4** calculated by applying various energy shifts $\Delta\varepsilon$. The profile of the PDOS can approximately fitted by a sum of two Lorentzian functions whose centers are indicated by the dotted lines. The energy axis has been rescaled with by the CBM energy as zero.

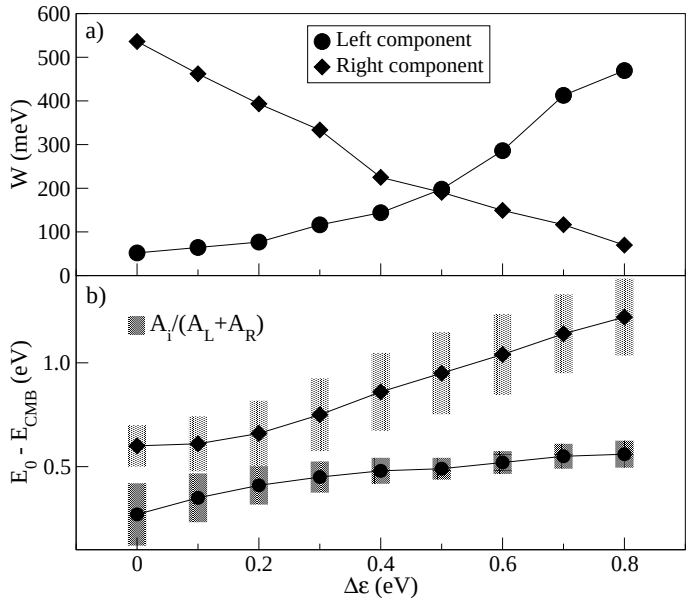

Figure 7.13: Panel a) Resonant linewidth of left and right components the LUMO versus $\Delta\varepsilon$ for the dye **d4**. Panel b) Centers E_0 of the two Lorentzians as a function of $\Delta\varepsilon$, together with the relative weight (vertical bars) of the two components $A_i/(A_L + A_R)$, i=L, R (A is the Lorentzian area).

7.5 Closing remarks

In this chapter we presented a scheme for the *ab initio* calculation of the resonant transfer of excited electrons from adsorbed molecules on a semiinfinite substrate. We applied it to triarylamine molecules on the (110) surface of rutile TiO_2, a system which is relevant for dye sensitized solar cells. Our results show how the LUMO resonant lifetime modifies with respect to the π-spacer length between the electron-donor and electron-acceptor ends of the dyes. A detailed analysis of the LUMO linewidth as a function of the resonance position inside the TiO_2 conduction band reveals the interaction with a surface feature that splits it into two components. Progress in this work will involve the characterization of the charge transfer with respect to other effects not included in this work, such as the molecular vibrations, defects in the substrate, different dye's functionalizations, and the presence of the electrolyte solution.

Conclusions

In recent years there has been a huge increase in the research on the electronic transport of organic molecular junctions. A wealth of techniques has been developed to contact single molecules to metallic electrodes and to measure the electronic and transport properties of such systems. The existence of new complex phenomena motivated the need for a theoretical description and interpretation. For these reasons this thesis focuses on the theoretical investigation of electronic transport in organic molecular junctions.

As a first step towards a full understanding of these phenomena, we applied the Landauer theory of coherent electronic transport to a simplified model. We considered a one dimensional potential of any shape inside a well defined scattering region. Inside that region, we initially took into account single barrier as well as double barrier potentials where the interaction with the continuum of free particle states yields electronic resonances. To compute transport with semi-infinite leads we made use of the embedding Green's function formalism. Though such a model is oversimplified, it still allowed us to capture the main features of resonant electronic transport, considering both jellium and metallic electrodes.

We then focused on the realistic description of molecular junctions, by means of *ab initio* calculations. Our approach relies on the combination of density functional theory and of the non-equilibrium Green's function technique. At the present, this is one of the most powerful theoretical methods to calculate the conductive properties of nanojunctions. In this work, this method has been applied to a number of different systems, which we categorize as two- and three-dimensional ones.

Transport in two-dimensional systems has been investigated considering molecular junctions with graphene electrodes. We first studied graphene junctions with armchair graphene nanoribbon linkers. These systems present a metal-semiconductor-metal behavior due to the electronic gap of the ribbons which depends on the their width. The electronic properties of the isolated subsystems, i.e. the graphene electrodes and the nanoribbon, together with their interaction in the contact regions, determine the transport properties of the junction. The coupling between the various subsystems is very efficient and the contacts do not create any appreciable barrier to transport mainly because the same chemical species constitute the full junction. Hence the transport properties are mainly determined by the shape (width and length) of the finite ribbon included between the graphene leads. The calculated results of the electronic transport provide some relevant parameters to control and engineer future

carbon-based electronic devices.

We also calculated the conductance of diarylethene-based molecular junctions sandwiched between graphene leads with zigzag edges. Our calculations show that at zero bias the peaks in the conductance show not only the molecule electronic states broadened into resonances by the coupling to the leads, but also the features of graphene edge states. Near the Fermi energy (E_{F}) the conductance of the closed isomer drastically lowers in the energy interval between the HOMO and the LUMO resonances of the molecule, following the linear dependence of the electrode density of states (DOS) proportional to $|E-E_{\mathrm{F}}|$. In the same range the conductance of the open isomer is about zero. If we apply a finite bias we observe that conductance is allowed within different energy windows for the open and closed isomers. We have also discussed the advantage of using graphene electrodes with respect to other materials, namely a reduced quenching of the photoexcited state compared to gold electrodes.

Moving to transport in three-dimensional systems, we present a comprehensive study of the conductance of a bi-stable pyrazine molecular junctions with Pt leads. We have calculated both the structural and transport properties as a function of the junction elongation, by following the minimum energy path. Our calculations reveal that the high- and low-conductance states found experimentally can be ascribed to different geometrical configurations in which the pyrazine axis is bent and coaxial with the junction. In these situations higher and lower couplings of the molecular orbitals with the electrodes occur, respectively. By a vibrational analysis of the junction, performed as a function of molecule's stretching, we were also able to identify the active vibrations found in experiments.

The model used in this thesis describes ballistic transport; the effect of the electron-phonon interaction is neglected and future development may concern such implementation. Still when experiments are available for comparison as for the pyrazine Pt junction, our results qualitatively describe the experimental conductance measurements.

Since the applied model well describes the electronic resonances of the junction coupled to semiinfinite electrodes these findings motivated the development of a scheme for the study of the resonant transfer of excited electrons from adsorbed molecules on metal or insulating substrates. To this end, we decided to combine the density functional calculation of a slab geometry with that of the bulk substrate, in order to obtain the Hamiltonian of the semi-infinite system which an electron is injected into. To test the method, we have studied the quantum-well state of Cs-p(2x2)-Cu(111). Our calculated elastic linewidth is fairly comparable with previous theoretical values. In the final part of our thesis work we preliminarly studied triarylamine molecules on TiO_2 rutile (110), a system which is relevant for dye sensitized solar cells. We were able to compute the elastic linewidths and lifetimes as a function of the length of the π-spacer between the electron-donor and electron-acceptor ends of the dyes. Further studies in this direction will help clarifying how charge transfer is affected by molecular vibrations, defects in the substrate, different dye's functionalizations, and the presence of the electrolyte solution.

Acknowledgments

The research work presented in this thesis has been done during my Ph.D. studies at the University of Milano-Bicocca, under the supervision of Prof. Gian Paolo Brivio. I wish to thank him for having suggested this very interesting topic and for his supervision and support to my Ph.D. project all the way through these years. A fundamental contribution to my work has been given by Drs. Mario Italo Trioni and Guido Fratesi, who spent hours of fruitful discussions with me. I am grateful to them for their helpful assistance during these years and for sharing their knowledge with support and patience. Part of my research has been carried on at the Donostia International Physics Center in Donostia-San Sebastián, under the supervision of Dr. Daniel Sánchez-Portal. It was a honor to work with him, whom I wish to thank for his extreme kindness and for his contribution to my project with his brilliant mind. I am also grateful to Dr. Simona Achilli, who has been a precious support more than once. I acknowledge Vincenzo Boffa of Pirelli for his help, and Prof. Francesco Mauri for accepting to referee this thesis work. I thank the CARIPLO foundation for its support within the PCAM European Doctoral Program and Pirelli for funding my scolarship.

I express my profound gratitude to my family for their constant support, understanding and continuous encouragement. Without it none of this would have been possible. Finally, but not least, all my love goes to Miriam, whose unconditional and faithful love has supported me through these years.

Carlo Motta, Milan, December 2012

Appendix A

Embedding formula in matrix form

We want to expand the embedding equation for the Green's function:

$$-\frac{1}{2}\frac{\partial^2 G}{\partial z^2} + (V-E)\,G(z,z';E) + \delta(z-z_R)\left[\frac{1}{2}\frac{\partial G}{\partial z} + \Sigma_R(E)G(z_R,z';E)\right] + \delta(z-z_L)\left[-\frac{1}{2}\frac{\partial G}{\partial z} + \Sigma_L(E)G(z_L,z';E)\right] = \delta(z-z') \tag{A.1}$$

in matrix form. This will be done by expanding the Green's function on a real-space basis:

$$G(z,z';E) = \sum_{i,j} G_{ij}(E)\chi_i(z)\chi_j(z') \tag{A.2}$$

where $G_{ij}(E)$ is an energy-dependent matrix, while $\{\chi_i(z)\}$ a suitable basis. By substitution we obtain

$$\sum_{ij} G_{ij}\Big\{-\frac{1}{2}\chi_i(z)'' + (V-E)\,\chi_i(z) + \delta(z-z_R)\left[\frac{1}{2}\chi_i'(z) + \Sigma_R\chi_i(z_R)\right] + \delta(z-z_L)\left[-\frac{1}{2}\chi_i'(z) + \Sigma_L\chi_i(z_L)\right]\Big\}\chi_j(z') = \delta(z-z')$$

If we multiply both the sides to a quantity $\chi_k(z)$, we obtain:

$$\sum_{ij} G_{ij}\Big\{-\frac{1}{2}\chi_i(z)''\chi_k(z) + (V-E)\,\chi_i(z)\chi_k(z) + \delta(z-z_R)\left[\frac{1}{2}\chi_i'(z)\chi_k(z) + \Sigma_R\chi_i(z_R)\chi_k(z)\right] + \delta(z-z_L)\left[-\frac{1}{2}\chi_i'(z)\chi_k(z) + \Sigma_L\chi_i(z_L)\chi_k(z)\right]\Big\}\chi_j(z') = \delta(z-z')\chi_k(z)$$

We now integrate between z_L and z_R, by exploiting the relation

$$\chi_i''\chi_k = -\chi_i'\chi_k' + \frac{d}{dz}\left[\chi_i'\chi_k\right]$$

which can be obtained by the z-derivative of $\chi_i'\chi_k$. The terms $\chi_i'(z_{L/R})\chi_k(z_{L/R})$ erase and we obtain

$$\sum_{ij} G_{ij}\left[H_{ij} - E\,S_{ij} + \Sigma_{ij}\right]\chi_j(z') = \chi_k(z') \quad , \tag{A.3}$$

where the Hamiltonian is given by

$$H_{ij} = \int_{z_L}^{z_R} \frac{1}{2}\chi_i'(z)\chi_k'(z)dz + \int_{z_L}^{z_R} V(z)\chi_i(z)\chi_k(z)dz$$

. The overlap matrix is

$$S_{ik} = \int_{z_L}^{z_R} \chi_i(z)\chi_k(z)dz$$

and the embedding matrix is

$$\Sigma_{ik}(E) = \Sigma_L(E)\chi_i(z_L)\chi_k(z_L) + \Sigma_R(E)\chi_i(z_R)\chi_k(z_R)$$

Since the functions χ form a basis, they are linearly independent. Therefore, in Eq. (A.3) the coefficients of the j sum on the left will be zero, except if $j = k$. Thus,

$$\sum_{i} G_{ij}\left[H_{ij} - E\,S_{ij} + \Sigma_{ij}\right] = \delta_{jk} \tag{A.4}$$

The latter can be re-written in compact form:

$$G = \left[H - ES + \Sigma\right]^{-1} \tag{A.5}$$

Appendix B

Extension from to 3D of a 1D dependent potential

In presence of 1D potentials $V(\mathrm{r}) = V(z)$, one can solve the Schröedinger in 1D and extend the solution to 3D.
The Green's equation reads:

$$\left(-\frac{\nabla^2_{\mathbf{r}}}{2} + V(z) - E\right) G(\mathbf{r}, \mathbf{r}'; E) = \delta(\mathbf{r} - \mathbf{r}') \quad .$$

If we separate the variables into R and z, where $R = (x, y)$, we obtain:

$$\left(-\frac{1}{2}\frac{\partial^2}{\partial z^2} - \frac{\nabla^2_R}{2} + V(z) - E\right) G(R, z, R', z'; E) = \delta(R - R')\delta(z - z' quad.)$$

We can now apply the Fourier transform for R and R', that is:

$$\mathcal{F}[f(\mathbf{rx})] = \int e^{-i\mathbf{kx}} f(\mathbf{x}) d\mathbf{x}$$

$$\mathcal{F}^{-1}[f(\mathbf{k})] = \frac{1}{(2\pi)^n} \int e^{i\mathbf{kx}} f(\mathbf{k}) d\mathbf{k} \quad ,$$

where n equals to 2 in our case. We thus obtain:

$$\left(-\frac{1}{2}\frac{\partial^2}{\partial z^2} + \frac{k^2_\parallel}{2} + V(z) - E\right) G(k_\parallel, z, k'_\parallel, z'; E) = \delta(z - z') \quad .$$

By applying a coordinates change $E_\perp = E - \frac{k^2_\parallel}{2}$ we obtain

$$\left(-\frac{1}{2}\frac{\partial^2}{\partial z^2} + V(z) - E_\perp\right) G(k_\parallel, z, k'_\parallel, z'; E_\perp + \frac{k^2_\parallel}{2}) = \delta(z - z') \tag{B.1}$$

By comparing the latter equation with the monodimensional one

$$\left(-\frac{1}{2}\frac{\partial^2}{\partial z^2} + V(z) - E\right) G^{1D}(z, z'; E) = \delta(z - z')$$

we notice that $G_{\mathbf{k}_\parallel}(z,z';E) = G^{1D}(z,z';E-\frac{k_\parallel^2}{2})$. Thus, the Green's function $G(\mathbf{r},\mathbf{r}';E)$ must be invariant upon translations in the (x,y) plane. For this reason, $k_\parallel = k'_\parallel$ in Eq. (B.1). We can now write the Green's function in 3D by the inverse Fourier transform:

$$\begin{aligned} G(\mathbf{r},\mathbf{r}';E) &= \frac{1}{(2\pi)^2}\int d\mathbf{k}_\parallel e^{-i\mathbf{k}_\parallel(R-R')}G_{\mathbf{k}_\parallel}(z,z';E) = \\ &= \frac{1}{(2\pi)^2}\int d\mathbf{k}_\parallel e^{-i\mathbf{k}_\parallel(R-R')}G^{1D}(z,z';E-\frac{k^2}{2}) \end{aligned} \tag{B.2}$$

The 1D result is useful if we want to compute non-exthensive quantities (like the conductance) in the direction normal to the surface (i.e. at the Γ point). For exthensive quantities (like the charge) we need the 3D result. Eq. (B.2) can be used to compute the density of states as well as the charge density in 3D. In therms of the Green's function, the local density of states is $\sigma(\mathbf{r},E) = \frac{1}{\pi}\mathrm{Im}G(\mathbf{r},\mathbf{r},E+i\delta)$. We can apply this formula and obtain:

$$\begin{aligned} \sigma(\mathbf{r},E) = \frac{1}{\pi}\mathrm{Im}G^{3D}(\mathbf{r},\mathbf{r};E) &= \frac{1}{\pi}\mathrm{Im}\frac{1}{(2\pi)^2}\int d^2\mathbf{k}e^{-i\mathbf{k}(R-R)}G^{1D}(z,z;E-\frac{k^2}{2}) = \\ &= -\frac{1}{\pi}\frac{2\pi}{(2\pi)^2}\mathrm{Im}\int_0^{+\infty} kdkG^{1D}(z,z;E-\frac{k^2}{2}) \end{aligned} ,$$

and by doing the substitution $E_\perp = E - \frac{k^2}{2} \Rightarrow dE_\perp = -kdk$, it follows:

$$\begin{aligned} \sigma(\mathbf{r},E) = -\frac{1}{2\pi^2}\mathrm{Im}\int_E^{-\infty} dE_\perp G^{1D}(z,z;E_\perp) &= \frac{1}{2\pi^2}\mathrm{Im}\int_{-\infty}^{E} dE_\perp G^{1D}(z,z;E_\perp) = \\ &= \frac{1}{2\pi}\int_{-\infty}^{E} dE_\perp \sigma(z,E_\perp) \end{aligned} \tag{B.3}$$

Bibliography

[1] J. Gimzewski and R. Möller. Transition from the tunneling regime to point contact studied using scanning tunneling microscopy. *Phys. Rev. B*, 36(2):1284–1287, 1987.

[2] C. J. Muller, J. M. Van Ruitenbeek, and L. J. De Jongh. Experimental observation of the transition from weak link to tunnel junction. *Physica C Superconductivity*, 191(3-4):485–504, 1992.

[3] N. Agraït, A. L. Yeyati, and J. M. Van Ruitenbeek. Quantum properties of atomic-sized conductors. *Phys. Rep.*, 377(2-3):120, 2002.

[4] M. Tsutsui and M. Taniguchi. Single molecule electronics and devices. *Sensors*, 12(6):7259–7298, 2012.

[5] J.C. Cuevas and E. Scheer. *Molecular Electronics: An Introduction to Theory and Experiment*. World Scientific Publishers, 2010.

[6] G. Rubio, N. Agraït, and S. Vieira. Atomic-sized metallic contacts: Mechanical properties and electronic transport. *Phys. Rev. Lett.*, 76:2302–2305, 1996.

[7] C. Joachim, G. K. Gimzewsky, and A. Aviram. Electronics using hybrid-molecular and mono-molecular devices. *Nature*, 408(6812):541–548, 2000.

[8] A. Nitzan and M. A. Ratner. Electron transport in molecular wire junctions. *Science*, 300(5624):1384–1389, 2003.

[9] A. Nitzan and M. A. Ratner. Electron transport in molecular junctions. *Nat. Nano*, 1(3):173–181, 2006.

[10] K. Moth-Poulsen and T. Bjornholm. Molecular electronics with single molecules in solid-state devices. *Nat. Nano*, 4(9):1748–3387, 2009.

[11] N. A. Zimbovskaya and M. R. Pederson. Electron transport through molecular junctions. *Phys. Rep.*, 509(1):1–87, 2011.

[12] H. Song, M. A. Reed, and T. Lee. Single molecule electronic devices. *Adv. Mater.*, 23(14):1583–1608, 2011.

[13] J. B. Neaton, M. S. Hybertsen, and S. G. Louie. Renormalization of molecular electronic levels at metal-molecule interfaces. *Phys. Rev. Lett.*, 97(21):4, 2006.

[14] M. A. Reed. Conductance of a molecular junction. *Science*, 278(5336):252–254, 1997.

[15] S. Datta. *Electronic transport mesoscopic systems*. Cambridge University Press, 1995.

[16] N. D. Lang. Resistance of atomic wires. *Phys. Rev. B*, 52:5335–5342, 1995.

[17] M. Di Ventra. *Electrical transport in nanoscale systems*. Cambridge University Press, 2008.

[18] M. Koentopp, C. Chang, K. Burke, and R. Car. Density functional calculations of nanoscale conductance. *J. Phys.: Condens. Matter*, 20(8):28, 2007.

[19] N.W. Ashcroft and N.D. Mermin. *Solid state physics*. Brooks Cole, 1976.

[20] B.H. Bransden and C.J. Joachain. *Physics of Atoms and Molecules*. Prentice Hall, 2nd edition.

[21] P. Hohenberg and W. Kohn. Inhomogenous electron gas. *Phys. Rev.* , 136 B:864, 1964.

[22] P. Giannozzi. Density functional theory for electronic structure calculations. *Lecture Notes*.

[23] H. Ehrenreich and M. H. Cohen. Self-consistent field approach to the many electron problem. *Phys. Rev.*, 115:786–790, 1959.

[24] R. Martin. *Electronic Structure: Basic Theory and Practical Methods*. Cambridge University Press, 2004.

[25] J. P. Perdew. Density-functional approximation for the correlation energy of the inhomogeneous electron gas. *Phys. Rev. B*, 33:8822–8824, 1986.

[26] J. P. Perdew, K. Burke, and M. Ernzerhof. Generalized gradient approximation made simple. *Phys. Rev. Lett.*, 77:3865–3868, 1996.

[27] G. P. Brivio and M. I. Trioni. The adiabatic molecule-metal surface interaction: Theoretical approaches. *Rev. Mod. Phys.*, 71:231–265, 1999.

[28] P. Ordejón, E. Artacho, and J. M. Soler. Self-consistent order-n density-functional calculations for very large systems. *Phys. Rev. B*, 53:R10441–R10444, 1996.

[29] J. M. Soler, E. Artacho, J. D. Gale, A. García, J. Junquera, P. Ordejón, and D. Sánchez-Portal. The SIESTA method for ab initio order-N materials simulation. *J. Phys.: Condens. Matter*, 14:2745–2779, 2002.

[30] E. Artacho, E. Anglada, O. Diéguez, J. D. Gale, A. García, J. Junquera, R. M. Martin, P. Ordejón, J. M. Pruneda, D. Sánchez-Portal, and J. M. Soler. The SIESTA method: Developments and applicability. *J. Phys.: Condens. Matter*, 20:064208, 2008.

[31] H. J. Monkhorst and J. D. Pack. Special points for Brillouin-zone integrations. *Phys. Rev. B*, 13:5188–5192, 1976.

[32] N. Troullier and J. L. Martins. Efficient pseudopotentials for plane-wave calculations. *Phys. Rev. B*, 43:1993–2006, 1991.

[33] M. Paulsson. Non equilibrium green's functions for dummies: Introduction to the one particle NEGF equations. arXiv:cond-mat/0210519, 2006.

[34] K. S. Thygesen and Jacobsen K. W. Molecular transport calculations with wannier functions. *J. Chem. Phys.*, 319:111–125, 2005.

[35] A. Messiah. *Quantum Mechanics*. North-Holland Publishing Company, 1961.

[36] M. P. L. Sancho, J. M. L. Sancho, J. M. L. Sancho, and J. Rubio. Highly convergent schemes for the calculation of bulk and surface green functions. *J. Phys. F: Met. Phys.*, 15(4):851–858, 1985.

[37] A. R. Rocha and S. Sanvito. Asymmetric I-V characteristics and magnetoresistance in magnetic point contacts. *Phys. Rev. B*, 70:094406, 2004.

[38] M. Brandbyge, J.-L. Mozos, P. Ordejón, J. Taylor, and K. Stokbro. Density-functional method for nonequilibrium electron transport. *Phys. Rev. B*, 65:165401, 2002.

[39] J. E. Inglesfield. A method of embedding. *J. Phys. C*, 14:3795, 1981.

[40] M. I. Trioni, G. P. Brivio, S. Crampin, and J. E. Inglesfield. Embedding approach to the isolated adsorbate. *Phys. Rev. B*, 53:8052–8064, 1996.

[41] H. Ishida, D. Wortmann, and T. Ohwaki. First-principles calculations of tunneling conductance. *Phys. Rev. B*, 70(8):085409, Aug 2004.

[42] D. Wortmann, H. Ishida, and S. Blügel. Embedded Green-function approach to the ballistic electron transport through an interface. *Phys. Rev. B*, 66(7):075113, 2002.

[43] L. Chang, L. Esaki, and R. Tsu. Resonant tunneling in semiconductor double barriers. *Appl. Phys. Lett.*, 24(12):593, 1974.

[44] E. Chulkov. Image potential states on metal surfaces: binding energies and wave functions.

[45] K. S. Novoselov, A. K. Geim, S. V. Morozov, D. Jiang, Y. Zhang, S. V. Dubonos, I. V. Grigorieva, and A. A. Firsov. Electric field effect in atomically thin carbon films. *Science*, 306(5696):1–12, 2004.

[46] A. K. Geim and K. S. Novoselov. The rise of graphene. *Nat. Phys.*, 6:183–191, 2007.

[47] A. H. Castro-Neto, F. Guinea, N. M. R. Peres, K. S. Novoselov, and A. K. Geim. The electronic properties of graphene. *Rev. Mod. Phys.*, 81:109–162, 2009.

[48] S. M. M. Dubois, Z. Zanolli, X. Declerck, and J.-C. Charlier. Electronic properties and quantum transport in graphene-based nanostructures. *Eur. Phys. J. B*, 72:1–24, 2009.

[49] J. C. Charlier, J. P. Michenaud, X. Gonze, and J. P. Vigneron. Tight-binding model for the electronic properties of simple hexagonal graphite. *Phys. Rev. B*, 44:13237–13249, 1991.

[50] P. R. Wallace. The band theory of graphite. *Phys. Rev.*, 71:622–634, 1947.

[51] G. Jo, M. Choe, S. Lee, W. Park, Y. H. Kahng, and T. Lee. The application of graphene as electrodes in electrical and optical devices. *Nanotechnol.*, 23:112001, 2012.

[52] J. P. Perdew, K. Burke, and M. Ernzerhof. Generalized gradient approximation made simple. *Phys. Rev. Lett.*, 77:3865–3868, 1996.

[53] M. Fujita, K. Wakabayashi, K. Nakada, and K. Kusakabe. Peculiar localized state at zigzag graphite edge. *J. Phys. Soc. Jpn.*, 65:1920–1923, 1996.

[54] K. Nakada, M. Fujita, G. Dresselhaus, and M. S. Dresselhaus. Edge state in graphene ribbons: Nanometer size effect and edge shape dependence. *Phys. Rev. B*, 54:17954–17961, 1996.

[55] K. Wakabayashi, M. Fujita, H. Ajiki, and M. Sigrist. Electronic and magnetic properties of nanographite ribbons. *Phys. Rev. B*, 59:8271–8282, 1999.

[56] Y. Son, M. L. Cohen, and S. G. Louie. Energy gaps in graphene nanoribbons. *Phys. Rev. Lett.*, 97:216803, 2006.

[57] P. Avouris, Z. Chen, and V. Perebeinos. Carbon-based electronics. *Nat. Nanotechnol.*, 2:605–615, 2007.

[58] S. Wang, P. K. Ang, Z. Wang, A. Ling L. Tang, J. T. L. Thong, and K. P. Loh. Energy gaps in graphene nanoribbons. *Nano Lett.*, 10:92–98, 2010.

[59] K. Wakabayashi, M. Fujita, H. Ajiki, and M. Sigrist. Electronic and magnetic properties of nanographite ribbons. *Phys. Rev. B*, 59:8271–8282, 1998.

[60] C. Berger, Z. Song, X. Li, X. Wu, N. Brown, C. Naud, D. Mayou, T. Li, J. Hass, A. N. Marchenkov, E. H. Conrad, P. N. First, and W. A. de Heeret. Electronic confinement and coherence in patterned epitaxial graphene. *Science*, 312:1191–1196, 2006.

[61] J. Cai, P. Ruffieux, R. Jaafar, M. Bieri, T. Braun, S. Blankenburg, M. Muoth, A. P. Seitsonen, M. Saleh, X. Feng, K. Müllen, and R. Fasel. Atomically precise bottom-up fabrication of graphene nanoribbons. *Nature*, 466:470–473, 2010.

[62] L. Jiao, X. Wang, G. Diankov, H. Wang, and H. Dai. Facile synthesis of high-quality graphene nanoribbons. *Nat. Nanotechnol.*, 5:321–325, 2010.

[63] N. M. R. Peres, A. H. Castro Neto, and F. Guinea. Conductance quantization in mesoscopic graphene. *Phys. Rev. B*, 73:195411, 2006.

[64] J. Tworzydło, B. Trauzettel, M. Titov, A. Rycerz, and C. W. J. Beenakker. Sub-poissonian shot noise in graphene. *Phys. Rev. Lett.*, 96:246802, 2006.

[65] L. Brey and H. A. Fertig. Electronic states of graphene nanoribbons studied with the dirac equation. *Phys. Rev. B*, 73:235411, 2006.

[66] Y. Hancock, A. Uppstu, K. Saloriutta, A. Harju, and M. J. Puska. Generalized tight-binding transport model for graphene nanoribbon-based systems. *Phys. Rev. B*, 81:245402, 2010.

[67] X. Chen, K. Song, B. Zhou, H. Wang, and G. Zhou. Dependence of transport on adatom location for armchair-edge graphene nanoribbons. *Appl. Phys. Lett.*, 98:093111, 2011.

[68] L. Rosales, P. Orellana, Z. Barticevic, and M. Pacheco. Transport properties of graphene nanoribbon heterostructures. *Microelectron. J.*, 39:537–540, 2008.

[69] K. Wakabayashi. Electronic transport properties of nanographite ribbon junctions. *Phys. Rev. B*, 64:125428, 2001.

[70] K. Wakabayashi and M. Sigrist. Zero-conductance resonances due to flux states in nanographite ribbon junctions. *Phys. Rev. Lett.*, 84:3390–3393, 2000.

[71] F. Muñoz Rojas, D. Jacob, J. Fernández-Rossier, and J. J. Palacios. Coherent transport in graphene nanoconstrictions. *Phys. Rev. B*, 74:195417, 2006.

[72] M. Yamamoto and K. Wakabayashi. Control of electric current by graphene edge structure engineering. *Appl. Phys. Lett.*, 95:082109, 2009.

[73] P. Darancet, V. Olevano, and D. Mayou. Coherent electronic transport through graphene constrictions: Subwavelength regime and optical analogy. *Phys. Rev. Lett.*, 102:136803, 2009.

[74] A. Rycerz, J. Tworzydlo, and C. W. J. Beenakker. Valley filter and valley valve in graphene. *Nat. Phys.*, 3:172–175, 2007.

[75] N. Tombros, A. Veligura, J. Junesch, M. H. D. Guimaraes, I. J. V. Marun, H. T. Jonkman, and B. J. Van Wees. Quantized conductance of a suspended graphene nanoconstriction. *Nat. Phys.*, 7:1–4, 2011.

[76] F. Prins, A. Barreiro, J. W. Ruitenberg, J. S. Seldenthuis, N. Aliaga-Alcalde, L. M. K. Vandersypen, and H. S. J. Van Der Zant. Room-temperature gating of molecular junctions using few-layer graphene nanogap electrodes. *Nano Lett.*, 11(11):4607–11, 2011.

[77] M. Begliarbekov, K. I. Sasaki, O. Sul, E. Yang, and S. Strauf. Optical control of edge chirality in graphene. *Nano Lett.*, 11(11):4874–8, 2011.

[78] Jing Shan Qi, Jian Yu Huang, Ji Feng, Da Ning Shi, and Ju Li. The possibility of chemically inert, graphene-based all-carbon electronic devices with 0.8 eV gap. *ACS Nano*, 5:3475–3482, 2011.

[79] S. M. M. Dubois, A. Lopez-Bezanilla, A. Cresti, F. Triozon, B. Biel, J. Charlier, and S. Roche. Quantum transport in graphene nanoribbons: Effects of edge reconstruction and chemical reactivity. *ACS Nano*, 4:1971–1976, 2010.

[80] S. V. Morozov, K. S. Novoselov, M. I. Katsnelson, F. Schedin, D. C. Elias, J. A. Jaszczak, and A. K. Geim. Giant intrinsic carrier mobilities in graphene and its bilayer. *Phys. Rev. Lett.*, 100:016602, 2008.

[81] K. I. Bolotin, K. J. Sikes, Z. Jiang, M. Klima, G. Fudenberg, J. Hone, P. Kim, and H. L. Stormer. Ultrahigh electron mobility in suspended graphene. *Solid State Comm.*, 146:351–355, 2008.

[82] M. I. Katsnelson, K. S. Novoselov, and A. K. Geim. Chiral tunnelling and the klein paradox in graphene. *Nat. Phys.*, 2:620–625, 2006.

[83] N. Troullier and J. L. Martins. Efficient pseudopotentials for plane-wave calculations. *Phys. Rev. B*, 43:1993–2006, 1991.

[84] C. Motta, D. Sánchez-Portal, and M. I. Trioni. Transport properties of armchair graphene nanoribbon junctions between graphene electrodes. *Phys. Chem. Chem. Phys.*, 14:10683–10689, 2012.

[85] T. Wassmann, A. P. Seitsonen, A. M. Saitta, M. Lazzeri, and F. Mauri. Structure, stability, edge states, and aromaticity of graphene ribbons. *Phys. Rev. Lett.*, 101:096402, 2008.

[86] E. Lortscher, M. Elbing, M. Tschudy, C. Von Hanisch, H. B. Weber, M. Mayor, and H. Riel. Charge transport through molecular rods with reduced π-conjugation. *Chem. Phys. Chem.*, 9:2252–2258, 2008.

[87] L. Venkataraman, J. E. Klare, C. Nuckolls, M. S. Hybertsen, and M. L. Steigerwald. Dependence of single-molecule junction conductance on molecular conformation. *Nature*, 442(7105):904–907, 2006.

[88] M. G. Vergniory, J. M. Granadino-Roldan, A. Garcia-Lekue, and Lin-Wang Wang. Molecular conductivity switching of two benzene rings under electric field. *Appl. Phys. Lett.*, 97:262114, 2010.

[89] M. Irie. Photochromism of diarylethene molecules and crystals. *Proc. Jpn. Acad. Ser. B-Phys. Biol. Sci.*, 86:472, 2010.

[90] S. Nakamura, S. Yokojima, K. Uchida, T. Tsujioka, A. Goldberg, A. Murakami, K. Shinoda, M. Mikami, T. Kobayashi, and S. Kobatake. Theoretical investigation on photochromic diarylethene: A short review. *J. Photochem. Photobiol. A-Chem.*, 200:10, 2008.

[91] M. Irie, S. Kobatake, and H. Horichi. Reversible surface morphology changes of a photochromic diarylethene single crystal by photoirradiation. *Science*, 291:1769, 2001.

[92] S. Kobatake, S. Takami, H. Muto, T. Ishikawa, and M. Irie. Rapid and reversible shape changes of molecular crystals on photoirradiation. *Nature*, 446:778, 2007.

[93] J. Huang, Q. Li, H. Su, and J. Yang. Transport properties through diarylethene derivatives between carbon nanotube electrodes: a theoretical study. *Chem. Phys. Lett.*, 479:120, 2009.

[94] N. Katsonis, M. Lubomska, M. M. Pollard, B. L. Feringa, and P. Rudolf. Synthetic light-activated molecular switches and motors on surfaces. *Prog. Surf. Sci.*, 82:407, 2007.

[95] S. J. van der Molen and P. Liljeroth. Charge transport through molecular switches. *J. Phys.: Condens. Matter*, 22:133001, 2010.

[96] J. He, F. Chen, P. A. Liddell, J. Andréasson, S. D. Straight, D. Gust, T. A. Moore, A. L. Moore, J. Li, O. F. Sankey, and S. M. Lindsay. Switching of a photochromic molecule on gold electrodes: single-molecule measurements. *Nanotechnol.*, 16:695, 2005.

[97] D. Dulic, S. J. van der Molen, T. Kudernac, H. T. Jonkman, J. J. D. de Jong, T. N. Bowden, J. van Esch, B. L. Feringa, and B. J. van Wees. One-way optoelectronic switching of photochromic molecules on gold. *Phys. Rev. Lett.*, 91:207402, 2003.

[98] S. J. van der Molen, H. van der Vegte, T. Kudernac, I. Amin, B. L. Feringa, and B. J. Van Wees. Stochastic and photochromic switching of diarylethenes studied by scanning tunnelling microscopy. *Nanotechnol.*, 17:310–314, 2006.

[99] J. Li, G. Speyer, and O. F. Sankey. Conduction switching of photochromic molecules. *Phys. Rev. Lett.*, 93:248302, 2004.

[100] N. Katsonis, T. Kudernac, M. Walko, S. J. van der Molen, B. J. Van Wees, and B. L. Feringa. Reversible conductance switching of single diarylethenes on a gold surface. *Adv. Mater.*, 18:1397, 2006.

[101] T. Kudernac, S. J. van der Molen, B. J. Van Wees, and B. L. Feringa. Uni- and bi-directional light-induced switching of diarylethenes on gold nanoparticles. *Chem. Commun.*, page 3597, 2006.

[102] X. Guo, J. P. Small, J. E. Klare, Y. Wang, M. S. Purewal, I. W. Tam, B. H. Hong, R. Caldwell, L. Huang, S. O'Brien, J. Yan, R. Breslow, S.J. Wind, J. Hone, P. Kim, and C. Nuckolls. Covalently bridging gaps in single-walled carbon nanotubes with conducting molecules. *Science*, 311:356, 2006.

[103] A. C. Whalley, M. L. Steigerwald, X. Guo, and C. Nuckolls. Reversible switching in molecular electronic devices. *J. Am. Chem. Soc.*, 129:12590, 2007.

[104] M. Kondo, T. Tada, and K. Yoshizawa. A theoretical measurement of the quantum transport through an optical molecular switch. *Chem. Phys. Lett.*, 412:55, 2005.

[105] J. Huang, Q. Li, H. Ren, H. Su, Q. W. Shi, and J. Yang. Switching mechanism of photochromic diarylethene derivatives molecular junctions. *J. Chem. Phys.*, 127:094705, 2007.

[106] A. Staykov, D. Nozaki, and K. Yoshizawa. Photoswitching of conductivity through a diarylperfluorocyclopentene nanowire. *J. Phys. Chem. C*, 111:3517, 2007.

[107] S. Y. Quek, M. Kamenetska, M. L. Steigerwald, H. J. Choi, S. G. Louie, M. S. Hybertsen, J. B. Neaton, and L. Venkataraman. Mechanically controlled binary conductance switching of a single-molecule junction. *Nat. Nanotechnol.*, 4(4):230–234, 2009.

[108] A. Odell, A. Delin, B. Johansson, I. Rungger, and S. Sanvito. Investigation of the conducting properties of a photoswitching dithienylethene molecule. *ACS Nano*, 4:2635, 2010.

[109] P. Zhao, P.i Wang, Z. Zhang, C. Fang, Y. Wang, Y. Zhai, and D. Liu. Electronic transport properties of a diarylethene-based molecular switch with single-walled carbon nanotube electrodes: The effect of chirality. *Solid State Commun.*, 149:928, 2009.

[110] C. Motta, M. I. Trioni, G. P. Brivio, and K. L. Sebastian. Conductance of a photochromic molecular switch with graphene leads. *Phys. Rev. B*, 84:113408, 2011.

[111] S. Pang, H. N. Tsao, L.I. Feng, and K. Muellen. Patterned graphene electrodes from solution-processed graphite oxide films for organic field-effect transistors. *Adv. Mater.*, 21:3488, 2009.

[112] J. H. Chen, C. Jang, S. Xiao, M. Ishigami, and M. S. Fuhrer. Intrinsic and extrinsic performance limits of graphene devices on SiO2. *Nat. Nanotech.*, 3:206, 2008.

[113] S. V. Morozov, K. S. Novoselov, M. I. Katsnelson, F. Schedin, D. C. Elias, J. A. Jaszczak, and A. K. Geim. Giant intrinsic carrier mobilities in graphene and its bilayer. *Phys. Rev. Lett.*, 100:016602, 2008.

[114] I. Diez-Perez, Z. Li, J. Hihath, J. Li, C. Zhang, X. Yang, L. Zang, Y. Dai, X. Feng, K. Muellen, and N. Tao. Gate-controlled electron transport in coronenes as a bottom-up approach towards graphene transistors. *Nat. Commun.*, 1:31, 2010.

[115] X. Wang, L. Zhi, and K. Mullen. Transparent, conductive graphene electrodes for dye-sensitized solar cells. *Nano Lett.*, 8:323, 2008.

[116] D. J. Jiang, B. G. Sumpter, and S. Dai. Unique chemical reactivity of a graphene nanoribbon's zigzag edge. *J. Chem. Phys.*, 126:134701, 2007.

[117] J. M. Soler, E. Artacho, J. D. Gale, A. Garcia, J. Junquera, P. Ordejón, and D. Sanchez-Portal. *J. Phys.: Condens. Matter*, 14:22, 2001.

[118] M. J. Marsella, Z. Wang, and R. H. Mitchell. Linked photoswitches where both photochromes open and close. *Org. Lett.*, 2:2979, 2000.

[119] M. Zhuang and M. Ernzerhof. Reversibility and transport properties of dithienylethene photoswitches. *J. Chem. Phys.*, 130(11):114704, 2009.

[120] M. K. Ashraf, N. A. Bruque, J. L. Tan, G. J. O. Beran, and R. K. Lake. Conductance switching in diarylethenes bridging carbon nanotubes. *J. Chem. Phys.*, 134(2):024524, 2011.

[121] C. Bertarelli, M. C. Gallazzi, F. Stellacci, G. Zerbi, S. Stagira, M. Nisoli, and S. De Silvestri. Ultrafast photoinduced ring-closure dynamics of a diarylethene polymer. *Chem. Phys. Lett.*, 359(3-4):278–282, 2002.

[122] P. R. Hania, A. Pugzlys, L. N. Lucas, J. J. D. De Jong, B. L. Feringa, J. H. Van Esch, H. T. Jonkman, and K. Duppen. Ring closure dynamics of BTE-based photochromic switches: perfluoro- versus perhydrocyclopentene derivatives. *J. Phys. Chem. A*, 109(42):9437–9442, 2005.

[123] S. Kaneko, C. Motta, G. P. Brivio, and M. Kiguchi. Mechanically controllable bi-stable states in highly conductive single pyrazine molecular junction. *J. Am. Chem. Soc.*, 2013. Submitted.

[124] D. Dulić, S. J. van der Molen, T. Kudernac, H. T. Jonkman, J. J. D. de Jong, T. N. Bowden, J. van Esch, B. L. Feringa, and B. J. van Wees. One-way optoelectronic switching of photochromic molecules on gold. *Phys. Rev. Lett.*, 91, 2003.

[125] M. Taniguchi, M. Tsutsui, K. Yokota, and T. Kawai. Mechanically-controllable single molecule switch based on configuration specific electrical conductivity of metal-molecule-metal junctions. *Chem. Sci.*, 1:247–253, 2010.

[126] B. Xu and N. J. Tao. Measurement of single-molecule resistance by repeated formation of molecular junctions. *Science*, 301:1221–1223, 2003.

[127] N. D. Lang and P. Avouris. Electrical conductance of individual molecules. *Phys. Rev. B*, 64:125323, 2001.

[128] M. Kamenetska, S. Y. Quek, A. C. Whalley, M. L. Steigerwald, H. J. Choi, S. G Louie, C. Nuckolls, M. S. Hybertsen, J. B. Neaton, and L. Venkataraman. Conductance and geometry of pyridine-linked single-molecule junctions. *J. Am. Chem. Soc.*, 132(19):6817–6821, 2010.

[129] K. Horiguchi and A. Kurokawa, S.and Sakai. High-bias breakdown of Au/1, 4-benzenedithiol/Au junctions. *J. Chem. Phys. B*, 131:104703/1–104703/5, 2009.

[130] F. Chen, X. Li, J. Hihath, Z. Huang, and N. Tao. Effect of anchoring groups on single-molecule conductance: comparative study of thiol-, amine-, and carboxylic-acid-terminated molecules. *J. Am. Chem. Soc.*, 128(49):15874–15881, 2006.

[131] A. Mishchenko, L. A. Zotti, D. Vonlanthen, M. Bürkle, F. Pauly, J. C. Cuevas, M. Mayor, and T. Wandlowski. Single-molecule junctions based on nitrile-terminated biphenyls: A promising new anchoring group. *J. Am. Chem. Soc.*, 133(2):184–187, 2010.

[132] L. Venkataraman, J. E. Klare, I. W. Tam, C. Nuckolls, M. S. Hybertsen, and M. L. Steigerwald. Single-molecule circuits with well-defined molecular conductance. *Nano Lett.*, 6(3):458–462, 2006.

[133] L. Venkataraman, Y. S. Park, A. C. Whalley, C. Nuckolls, M. S. Hybertsen, and M. L. Steigerwald. Electronics and chemistry: Varying single molecule junction conductance using chemical substituents. *Nano Lett.*, 7(2):502–506, 2007.

[134] R. Parameswaran, J. R. Widawsky, H. Vázquez, Y. S. Park, B. M. Boardman, C. Nuckolls, M. L. Steigerwald, M. S. Hybertsen, and L. Venkataraman. Reliable formation of single molecule junctions with air-stable diphenylphosphine linkers. *J. Phys. Chem. Lett.*, 1(14):2114–2119, 2010.

[135] Y. S. Park, A. C. Whalley, M. Kamenetska, M. L. Steigerwald, M. S. Hybertsen, C. Nuckolls, and L. Venkataraman. Contact chemistry and single-molecule conductance: a comparison of phosphines, methyl sulfides, and amines. *J. Am. Chem. Soc.*, 129(51):15768–15769, 2007.

[136] M. Kiguchi, S. Miura, K. Hara, M. Sawamura, and K. Murakoshi. Conductance of a single molecule anchored by an isocyanide substituent to gold electrodes. *Appl. Phys. Lett.*, 89(21):213104, 2006.

[137] M. Kiguchi, O. Tal, S. Wohlthat, F. Pauly, M. Krieger, D. Djukic, J. C. Cuevas, and J. M. van Ruitenbeek. Highly conductive molecular junctions based on direct binding of benzene to platinum electrodes. *Phys. Rev. Lett.*, 101:046801, 2008.

[138] Z. L. Cheng, R. Skouta, H. Vazquez, J. R. Widawsky, S. Schneebeli, W. Chen, M. S. Hybertsen, R. Breslow, and L. Venkataraman. In situ formation of highly conducting covalent Au-C contacts for single-molecule junctions. *Nat. Nanotechnol.*, 6(6):353–357, 2011.

[139] S. Kaneko, T. Nakazumi, and M. Kiguchi. Fabrication of a well-defined single benzene molecule junction using Ag electrodes. *J. Phys. Chem. Lett.*, 1(24):3520–3523, 2010.

[140] F. If. Measurement of the conductance of a hydrogen molecule. *Nature*, 419:906–909, 2002.

[141] M. Kiguchi, T. Nakazumi, K. Hashimoto, and K. Murakoshi. Atomic motion in single H2 and D2 molecule junction induced by phonon excitation. *Phys. Rev. B*, 81(4):5, 2009.

[142] B. C. Stipe, M. A. Rezaei, and W. Ho. Single-molecule vibrational spectroscopy and microscopy. *Science*, 280(5370):1732–1735, 1998.

[143] N. Okabayashi, M. Paulsson, H. Ueba, Y. Konda, and T. Komeda. Site selective inelastic electron tunneling spectroscopy probed by isotope labeling. *Nano Lett.*, 10(8):2950–2955, 2010.

[144] D. P. Long, J. L. Lazorcik, B. A. Mantooth, M. H. Moore, M. A. Ratner, A. Troisi, Y. Yao, J. W. Ciszek, J. M. Tour, and R. Shashidhar. Effects of hydration on molecular junction transport. *Nature Materials*, 5(11):901–908, 2006.

[145] J. Hihath, C. R. Arroyo, G. Rubio-Bollinger, N. Tao, and N. Agraït. Study of electron-phonon interactions in a single molecule covalently connected to two electrodes. *Nano Lett.*, 8(6):1673–1678, 2008.

[146] J. M. Beebe, H. J. Moore, T. R. Lee, and J. G. Kushmerick. Vibronic coupling in semi-fluorinated alkanethiol junctions: implications for selection rules in inelastic electron tunneling spectroscopy. *Nano Lett.*, 7(5):1364–1368, 2007.

[147] A. V. Khotkevich. Modern state of point contact spectroscopy of electron-phonon interaction in transition metals. *Physica B*, 218:31–34, 1996.

[148] A. Kokalj and M. Causà. Periodic density functional theory study of Pt(111): surface features of slabs of different thickness. *J. Phys.: Condens. Matter*, 11:7463, 1999.

[149] C. Toher, A. Filippetti, S. Sanvito, and Kieron Burke. Self-interaction errors in density-functional calculations of electronic transport. *Phys. Rev. Lett.*, 95:146402, 2005.

[150] C. Toher and S. Sanvito. Effects of self-interaction corrections on the transport properties of phenyl-based molecular junctions. *Phys. Rev. B*, 77:155402, 2008.

[151] M. Paulsson and M. Brandbyge. Transmission eigenchannels from nonequilibrium green's functions. *Phys. Rev. B*, 76:115117, 2007.

[152] A. Hagfeldt, G. Boschloo, L. Sun, L. Kloo, and H. Pettersson. Dye-sensitized solar cells. *Chem. Rev.*, 110(11):6595–6663, 2010.

[153] D. Sánchez-Portal. Slab calculations and Green's function recursive methods combined to study the electronic structure of surfaces: application to Cu(111)–(4x4)–Na. *Prog. Surf. Sci.*, 82(46):313–335, 2007.

[154] V. Chis, S. Caravati, G. Butti, M. I. Trioni, P. Cabrera-Sanfelix, A. Arnau, and B. Hellsing. Two-dimensional localization of fast electrons in $p(2 \times 2)$-CsCu(111). *Phys. Rev. B*, 76:153404, 2007.

[155] C. Corriol, V. M. Silkin, D. Sánchez-Portal, A. Arnau, E. V. Chulkov, P. M. Echenique, T. von Hofe, J. Kliewer, J. Kröger, and R. Berndt. Role of elastic scattering in electron dynamics at ordered alkali overlayers on Cu(111). *Phys. Rev. Lett.*, 95:176802, 2005.

[156] Z. Ning and H. Tian. Triarylamine: a promising core unit for efficient photovoltaic materials. *Chem. Commun.*, pages 5483–5495, 2009.

[157] K. M. Glassford and J. R. Chelikowsky. Structural and electronic properties of titanium dioxide. *Phys. Rev. B*, 46(3):1284–1298, 1992.

[158] U. Diebold. The surface science of titanium dioxide. *Surf. Sci. Rep.*, 48(5-8):53–229, 2003.

[159] A. Beltrán, J. Andrés, J. R. Sambrano, and E. Longo. Density functional theory study on the structural and electronic properties of low index rutile surfaces for TiO2/SnO2/TiO2 and SnO2/TiO2/SnO2 composite systems. *J. Phys. Chem. A*, 112(38):8943–8952, 2008.

[160] S.P. Bates, G. Kresse, and M. J. Gillan. The adsorption and dissociation of ROH molecules on TiO2(110). *Surf. Sci.*, 409(2):336–349, 1998.

[161] W. R. Duncan and O. V. Prezhdo. Theoretical studies of photoinduced electron transfer in dye-sensitized TiO2. *Annu. Rev. Phys. Chem.*, 58:143–184, 2007.

[162] S.A. Chambers, S. Thevuthasan, Y.J. Kim, G.S. Herman, Z. Wang, E. Tober, Ynzunza, J. Morais, C. H. F. Peden, K. Ferris, and C.S. Fadley. Chemisorption geometry of formate on Ti2(110) by photoelectron diffraction. *Chem. Phys. Lett.*, 267(12):51 – 57, 1997.

[163] K. Fukui, H. Onishi, and Y. Iwasawa. Imaging of individual formate ions adsorbed on TiO2(110) surface by non-contact atomic force microscopy. *Chem. Phys. Lett.*, 280(34):296 – 301, 1997.

[164] N. Martsinovich and A. Troisi. Theoretical studies of dye-sensitised solar cells: from electronic structure to elementary processes. *Energy Environ. Sci.*, 4(11):4473, 2011.

[165] N. Martsinovich and A. Troisi. High-throughput computational screening of chromophores for dye-sensitized solar cells. *System*, 115(23):11781–11792, 2011.